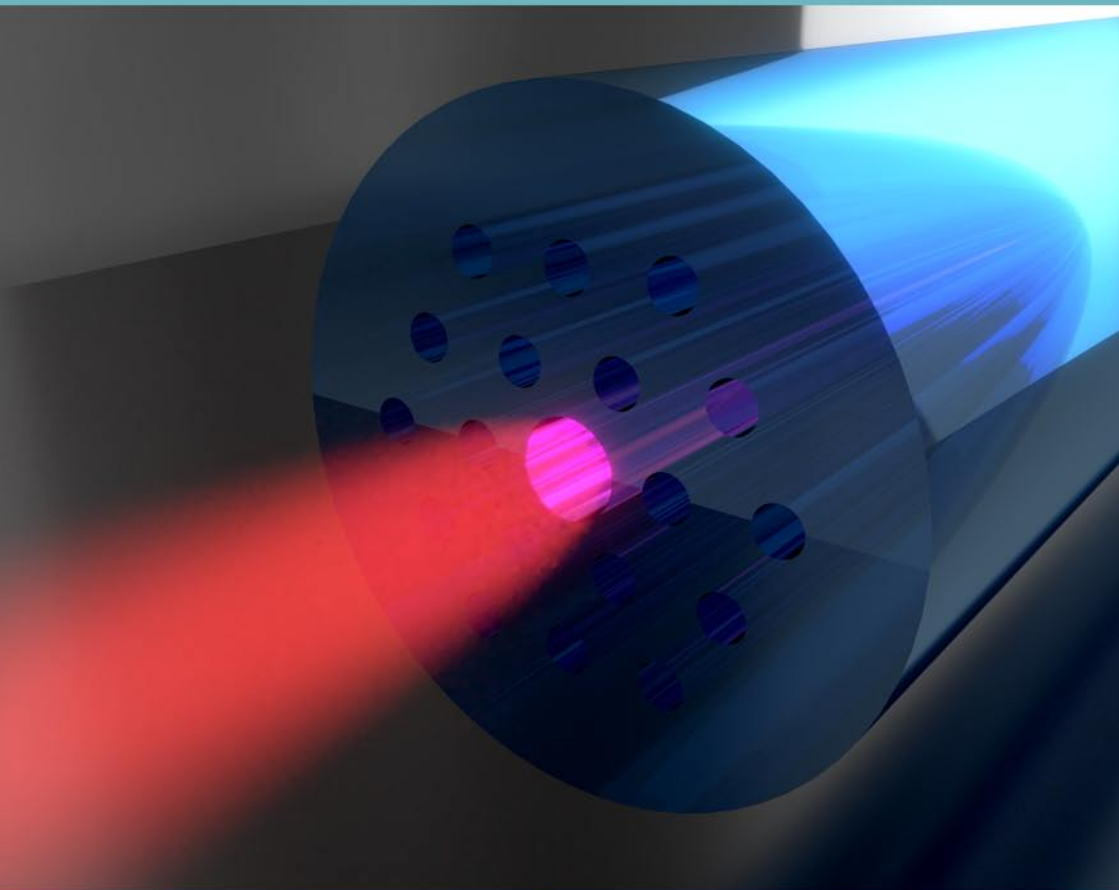# Perturbation and manipulation of leaky modes in photonic crystal fibers

Swaathi Upendar

University of Stuttgart
2020

Perturbation and manipulation of leaky modes in photonic crystal fibers

Von der Fakultät Mathematik und Physik der Universität Stuttgart
zur Erlangung der Würde eines Doktors der
Naturwissenschaften (Dr. rer. nat.) genehmigte Abhandlung

Vorgelegt von

Swaathi Upendar

Hauptberichter:	Apl. Prof. Dr. Thomas Weiss
Mitberichter:	Prof. Dr. Eric Lutz
Vorsitzender:	Prof. Dr. Sebastian Loth

Tag der mündlichen Prüfung: 30.09.2020

4. Physikalisches Institut der Universität Stuttgart

2020

Contents

Abbreviations

Technical abbreviations:

RSE	Resonant state expansion
FT	Fourier transform
PBG	Photonic bandgap
PCF	Photonic crystal fiber
DOS	Density of states
ARROW	Anti resonant reflecting optical waveguides
FMM	Fourier modal method
PML	Perfectly matched layers
a.u.	Arbitrary units
NLSE	Nonlinear Schrodinger equation
GVD	Group velocity dispersion

Physical quantities:

c	Speed of light in vacuum
ε, μ	Permittivity and permeability
ω	Angular frequency
k_0	Vacuum wave number $k_0 = \frac{\omega}{c}$
β	Propagation constant in the direction of invariance
χ	Radial propagation constant
$\mathbb{E}$	Electric field
$\mathbb{H}$	Magnetic field
$\mathbb{D}$	Electric displacement
$\mathbb{B}$	Magnetic induction
$\mathbb{J}$	Current vector
$\mathbb{S}$	Poynting vector

Abstract

Optical fibers guide light in a central core surrounded by a cladding. The most common fibers are step-index fibers, which guide light using total internal reflection in the fiber core. Recently, a new class of fibers, with a microstructured cladding, which also include photonic crystal fibers have been developed. The photonic crystal fibers have a periodic refractive index profile in the cladding and guide light using a bandgap effect or modified total internal reflection. Photonic crystal fibers promise to surpass the guiding properties of the traditional step-index fiber and are being studied extensively. However, these new fibers support leaky modes in contrast to the perfectly guided or bound modes of the conventional step-index fiber. Leaky modes are solutions to Maxwell's equations that radiate energy in the transverse direction of the fiber. This energy leakage leads to growing fields in the homogeneous exterior. Due to these growing fields in the exterior, the normalization of leaky modes has been a long standing challenge.

The normalization for bound modes, which have exponentially decaying fields as we move away from the fiber core, is achieved using an integral of the time-averaged Poynting vector over the xy plane. However, this expression diverges for the case of leaky modes. In this thesis, we derive a general analytical normalization for leaky and bound modes in fiber structures that is independent of the region of integration as long as it encloses all spatial inhomogeneities.

Using this analytical normalization, which is an essential factor in any perturbation theory, we develop perturbation theories for interior and exterior perturbations in fiber geometries supporting leaky modes. The perturbations are considered to be changes in the permittivity and permeability tensors of the fiber, which also extend to the axial, i.e., the translationally invariant direction. We formulate the exterior perturbation theory to also treat wavelength as a perturbation. This is highly useful to obtain important fiber quantites such as group velocity as a simple post processing step instead of repeatedly solving Maxwell's equations for different wavelengths. We demonstrate the accuracy of both perturbation theories on analytically solvable capillary fibers and the more complicated photonic crystal fibers. We also demonstrate the usefulness of a perturbation theory in studying disorder, which involves averaging over many realizations.

Furthermore, we present a theoretical study of a novel design to reduce the confinement loss of the fundamental core mode in photonic bandgap fibers with high index strands. This is done by modifying the radius of specific strands, which we call "corner strands", in the core surround. We demon-

strate the usefulness of the analytical normalization in optimizing the fiber design by providing a physically meaningful way of comparing field confinement for different fiber structures. As fundamental working principle, we show that varying the radius of the corner strands leads to backscattering of light back to the core. By using an optimal radius for these corner strands in each transmission window, the losses are decreased by orders of magnitude in comparison to the unmodified cladding structure. We do a parametric analysis of this phenomenon by varying different structural properties such as radius, pitch and the radius-to-pitch ratios to find the optimal design. Thus, we generalize the previously studied case of missing corner strands which only works for certain radius-to-pitch ratios in the first bandgap. This design can be adapted to any photonic bandgap fiber including hollow core photonic crystal fibers and light cage structures.

Zusammenfassung

Optische Fasern leiten Licht in einem von einem Mantel umgebenen zentralen Kern. Die am weitesten verbreiteten Fasern sind Stufenindexfasern, die Licht durch Ausnutzung von interner Totalreflektion im Faserkern leiten. Vor kurzem wurde eine neue Klasse von Fasern mit mikrostrukturiertem Mantel entwickelt, zu denen auch photonische Kristallfasern gehören. Diese Fasern haben ein periodisches Brechungsindexprofil im Mantel und leiten Licht durch Ausnutzung eines Bandlückeneffekts oder modifizierter interner Totalreflektion. Photonische Kristallfasern versprechen die Leitfähigkeiten von traditionellen Stufenindexfasern zu übersteigen und werden deshalb ausgiebig erforscht. Jedoch unterstützen diese neuen Fasern Leckmoden, im Unterschied zu den perfekt geführten oder gebundenen Moden der konventionellen Stufenindexfasern. Leckmoden sind Lösungen der Maxwell-Gleichungen, die Energie in die transversale Richtung der Faser abstrahlen. Dieser Energieverlust führt zu anwachsenden Feldern im homogenen Äußeren der Faser. Durch diese anwachsenden Felder im Äußeren war die Normierung von Leckmoden eine für lange Zeit bestehende Herausforderung.

Die Normierung von gebundenen Moden, die exponentiell abfallende Felder aufweisen, wenn wir uns vom Faserkern wegbewegen, wird erreicht durch Nutzung eines Integrals des zeitgemittelten Poynting-Vektors über die *xy* Ebene. Dieser Ausdruck divergiert jedoch für den Fall von Leckmoden. In dieser Arbeit leiten wir eine allgemeine analytische Normierung für Leckmoden und für gebundene Moden in Faserstrukturen her, die unabhängig von dem Integrationsvolumen ist, solange dieses alle räumlichen Inhomogenitäten umschließt.

Unter Verwendung dieser analytischen Normierung, die einen wesentlichen Faktor jeder Störungstheorie darstellt, entwickeln wir zwei Störungstheorien für innere und äußere Störungen in Fasergeometrien, die Leckmoden unterstützen. Die Störungen werden als Änderungen der Permittivitäts- und Permeabilitätstensoren der Faser betrachtet, die sich auch über die axiale, d.h. die translationsinvariante Richtung erstrecken. Wir erweitern die externe Störungstheorie dazu, auch Wellenlänge als Störung zu behandeln. Dies ist sehr nützlich um wichtige Faserkenngrößen wie Gruppengeschwindigkeit als einfachen Nachbereitungsschritt zu erhalten, anstatt wiederholt die Maxwell-Gleichungen für verschiedene Wellenlängen zu lösen. Wir demonstrieren die Genauigkeit von beiden Störungstheorien an analytisch lösbaren Kapillarfasern und den komplizierteren photonischen Kristallfasern. Wir demonstrieren auch die Nützlichkeit einer Störungstheorie bei der Untersuchung von Unordnung, welche Mittelung über viele Realisierungen beinhaltet.

Des Weiteren präsentieren wir eine theoretische Untersuchung eines neuartigen und leicht herstellbaren Designs zur Reduzierung der Einschränkungsverluste der fundamentalen Kernmode in photonischen Bandlückenfasern mit hochbrechenden Strängen. Dies wird durch Modifikation des Radius bestimmter Stränge in der Kernumfassung, die wir als "Eckstränge" bezeichnen, erreicht. Wir demonstrieren die Nützlichkeit der analytischen Normierung zur Optimierung von Faserdesigns, indem wir eine physikalisch sinnvolle Art und Weise bereitstellen, die Feldbeschränkung zu vergleichen. Als fundamentales Funktionsprinzip zeigen wir, dass Variation des Radius der Eckstränge zur Rückstreuung von Licht zurück in den Kern führt. Durch Nutzen eines optimalen Radius für die Eckstränge in jedem Transmissionsfenster werden die Verluste, im Vergleich zu der unmodifizierten Mantelstruktur, um Größenordnungen reduziert. Wir führen eine parametrische Analyse dieses Phänomens durch, indem wir verschiedene strukturelle Eigenschaften wie Radius, Abstand und Radius-zu-Abstand-Verhältnis variieren, um das optimale Design zu finden. Auf diese Weise verallgemeinern wir den bereits untersuchten Fall von fehlenden Ecksträngen, der nur für bestimmte Radius-zu-Abstand-Verhältnisse innerhalb der ersten Bandlücke funktioniert. Wir zeigen, dass unser Ansatz auf jegliche photonische Bandlückenfaser einschließlich photonischer Hohlkernkristallfasern und Lichtkäfigstrukturen angepasst werden kann.

Publications

Published:

- S. Upendar, I. Allayarov, M. A. Schmidt, and T. Weiss, "Analytical mode normalization and resonant state expansion for bound and leaky modes in optical fibers-an efficient tool to model transverse disorder," Opt. Express **26**, 22536–22546 (2018).

- I. Allayarov, S. Upendar, M. A. Schmidt, and T. Weiss, "Analytic mode normalization for the Kerr nonlinearity parameter: Prediction of nonlinear gain for leaky modes," Physical Review Letters **121**, 213905 (2018).

Publications in preparation/submitted:

- S. Upendar, R. F. Ando, M. A. Schmidt, and T. Weiss, "Orders of magnitude loss reduction in photonic bandgap fibers by engineering the core surround", in preparation.

- S. Upendar, M. A. Schmidt, and T. Weiss, "What optical fiber modes reveal: Group velocity and effective index for external perturbations", in preparation.

- J. Kim, B. Jang, J. Gargiulo, J. Bürger, J. Zhao, S. Upendar, T. Weiss, S. Maier, and M. Schmidt, "The optofluidic light cage - an innovative approach for integrated spectroscopy using an on-chip anti-resonance hollow core waveguide", Analytical Chemistry, accepted.

Patents:

- "Wellenleiter und Faserlaser", anti-resonant waveguide to reduce orders of magnitude confinement loss by corner strand modification, patent applied to Deutsches Patent- und Markenamt, Patent pending.

Conferences:

- S. Upendar, I. Allayarov, M. A. Schmidt, and T. Weiss: Resonant State Expansion in Fiber Geometries, International School and Con-

ference on Disorder in Materials Science (DisoMAT), Potsdam (Germany), 2019.

- S. Upendar, I. Allayarov, M. A. Schmidt, and T. Weiss: Resonant state expansion for exterior perturbations in photonic crystal fibers, DPG Fruhjahrstagung der Sektion Atome, Molekule, Quantenoptik und Plasmen (SAMOP), Rostock (Germany), 2019.

- I. Allayarov, S. Upendar, M. A. Schmidt, and T. Weiss: A New Theoretical Formulation for the Nonlinear Pulse Propagation in Waveguide Geometries, OSA Nonlinear Optics (NLO), Hawaii (USA), 2019.

- I. Allayarov, S. Upendar, M. A. Schmidt, and T. Weiss: The impact of a new approach for the Kerr nonlinearity parameter on four-wave mixing, DPG Fruhjahrstagung der Sektion Atome, Molekule, Quantenoptik und Plasmen (SAMOP), Rostock (Germany), 2019.

- S. Upendar, I. Allayarov, G. Li, M. Schmidt, and T. Weiss: "Resonant State Expansion in Fiber Geometries." In Conference on Lasers and Electro-Optics Pacific Rim, pp. W4E-6. Optical Society of America, Hong Kong, 2018.

- S. Upendar, I. Allayarov, M. A. Schmidt, and T. Weiss: Resonant state expansion for disordered claddings in photonic crystal fibers, DPG Fruhjahrstagung der Sektion Kondensierte Materie (SKM), Berlin (Germany), 2018.

- I. Allayarov, S. Upendar, M. A. Schmidt, and T. Weiss: A new definition for the Kerr nonlinearity parameter, DPG Fruhjahrstagung der Sektion Atome, Molekule, Quantenoptik und Plasmen (SAMOP), Erlangen (Germany), 2018.

- I. Allayarov, S. Upendar, M. A. Schmidt, and T. Weiss: A new definition for the Kerr nonlinearity parameter, XXVI International Workshop on Optical Wave and Waveguide theory and Numerical Modelling (OWTNM), Bad Sassendorf (Germany), 2018.

- S. Upendar, G. Li, M. Nesterov M. A. Schmidt, and T. Weiss: Photonic crystal fibers with disordered claddings, DPG Fruhjahrstagung der Fachverband Halbleiterphysik, Dresden (Germany), 2017.

1 Introduction to fibers

There is a theory which states that if ever anyone discovers exactly what the Universe is for and why it is here, it will instantly disappear and be replaced by something even more bizarre and inexplicable. There is another theory which states that this has already happened.

Hitchhiker's guide to the Galaxy, Douglas Adams

Optical fibers guide light in a central core which is surrounded by a cladding. Depending on the type of the fiber and its guiding mechanism, the cladding can be microstructured or comprise of a homogeneous medium. The working concept of an optical fiber was known from the 19th century or earlier, which used total internal reflection as its guiding mechanism. The practical applications did not start till the 20th century, with the invention of the ruby-laser, which could be used as a coherent light source. After the discovery of the correct material for long distance communication systems, i.e., silica glass, optical fibers started to have much lower losses than their metallic counterparts. They are also immune to interference from the surrounding and transmit data with high bandwidths. Hence, they soon replaced metallic wires in telecommunications [1]. However, now optical fibers are used in many more applications like sensing [1–3], biochemistry [3], medicine [4, 5], image processing [6], non-linear effects [7] such as second and third harmonic generation [8], four wave mixing [9] and so on. Here, we briefly describe different types of optical fibers along with their guiding mechanisms.

1.1 Types of optical fibers

Optical fibers with a homogeneous cladding can be broadly classified into 3 types depending on the core refractive index and how it compares to the refractive index of the cladding. Note that in fabricated optical fibers the cladding is split into inner and outer claddings, also called the jacket. However, the effect of the jacket is completely ignored in the following work and only a homogeneous exterior background is considered.

- Step-index fibers: They usually comprise of a circular core of radius r with the refractive index of the core greater than the cladding refractive index, i.e., $n_{core} > n_{clad}$. The guiding mechanism is total internal reflection, due to the higher core index.

- Graded index fibers: Graded index fibers have a core refractive index that gradually decreases with increasing core radius r. This results in continual refocusing of light into the core.

- Capillary fibers: Capillary fibers have a core index which is smaller than the cladding refractive index, i.e., $n_{core} < n_{clad}$. The main guiding mechanism is reflection at the core-cladding interface.

The refractive index profiles of step (a), graded (b) and capillary (c) fibers are plotted in Fig. 1.1.
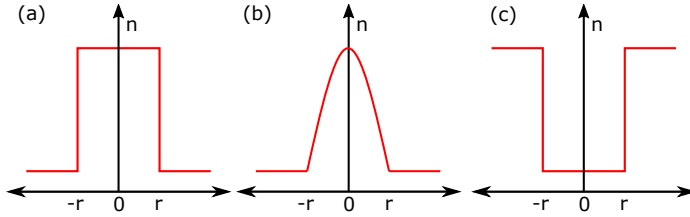
Figure 1.1: The refractive index profile as a function of radius for (a) step-index (b) graded index and (c) capillary fibers.

We now move to fibers which have a microstructured cladding. When a cladding has a periodic change in refractive index, in one or two dimensions, they are called photonic crystal fibers [10]. The third dimension is the direction in which light is guided along the fiber. Hence, it is translationally invariant and shall henceforth be referred to as the z direction. The core of these fibers is formed by creating a defect in the periodic cladding structure. Note that theoretically in every fiber there is a homogeneous exterior, which for photonic crystal fibers is beyond the finite microstructured cladding. Schematics of photonic crystal fibers of 1-D and 2-D periodicity are shown in Fig. 1.2 (a) and (b-c), respectively. The schematic (b) denotes high index rods in a low index background while (c) shows low index rods in a high index background. The guidance mechanism of these fiber structures varies depending on the fiber parameters. Photonic crystal and microstructured fibers guide light by using the following effects:

- Photonic bandgap (PBG) effect: Similar to solid state physics where the periodicity in potential due to the lattice of solids creates a bandgap where no electronic states exist [11], in photonics the periodic refractive index profile leads to a photonic bandgap. In the photonic bandgap the density of photonic states is zero. Creating a defect, also called the core, in this periodic lattice then traps light within the defect core, due to the presence of the bandgap. The main advantage of the bandgap effect is that it can be used to trap light in air or a low refractive index media, which is not possible in conventional step-index fibers where guidance can occur only in the high index medium. This can be highly useful in removing losses due to material absorption which occurs when guiding light in high index media.

  The density of states (DOS) for a 2-D photonic crystal is shown in Fig 1.2 (d) for a triangular lattice unit cell. The refractive index of the strand (also called inclusion) in the unit cell is $n_{strand} = 1.59$ with a background refractive index of $n = 1.44$. The ratio of radius-to-pitch

$r/\Lambda = 0.2$, where the pitch Λ denotes the center to center interstrand distance. Note that x and y axis of the density of states plot is unitless with β denoting the propagation constant, $k_0 = 2\pi/\lambda$ is the wavenumber and λ is the wavelength. The propagation constant describes how the amplitude and phase of light guided in the fiber varies in the direction of translational invariance, which we consider as the z direction. Guidance within the defect core occurs in regions where $\beta < nk_0$. In Fig. 1.2 (d), we see zero DOS that satisfies this condition. Hence, photonic bandgaps of first and higher orders are observed. The absolute value of the z component of the Poynting vector of the fundamental core mode of the fiber whose DOS is shown in panel (d) is plotted in Fig. 1.2 (e) at a wavelength of 1.71 μm, which lies in the first bandgap for a period Λ of 3.82 μm. The schematic of the fiber is as in panel (b). Examples of fibers that use photonic bandgap effects are Bragg or omniguide photonic crystal fibers [12], high index photonic crystal fibers [see Fig. 1.2 (a,b)] and hollow core photonic crystal fibers [10, 13, 14].

- Modified total internal reflection: Some photonic crystal fibers do not create a photonic bandgap due to the choice of materials and fiber parameters even though they consist of a periodically varying refractive index cladding. The first working photonic crystal fiber was a silica fiber with periodic air inclusions similar to the schematic in Fig. 1.2 (c). Due to the presence of the low index air strands in the cladding, the overall refractive index of the cladding is lower than the high index silica core. Hence, even though no PBG was created, the fiber guided light by modified total internal reflection similar to a conventional step-index fiber [10]. By manipulating the fiber parameters it has been shown that such fibers can also be endlessly single mode [15].

- ARROW model: There is another class of fibers which do have a microstructured cladding but it is not periodic. The number of cladding rings is very few, limited to one or two around a central core and hence they do not create a bandgap effect. In such cases, light guidance can occur because of an anti resonant reflection of light from the cladding structure back to the core. Such fibers are called anti resonant reflecting optical waveguides (ARROW) [16, 17].

As photonic crystal fibers possess multiple parameters which can be manipulated in the design of microstructured claddings, such as shape, distance, materials and so on, the possibilities are endless and hence they can be tailored to suit many applications.
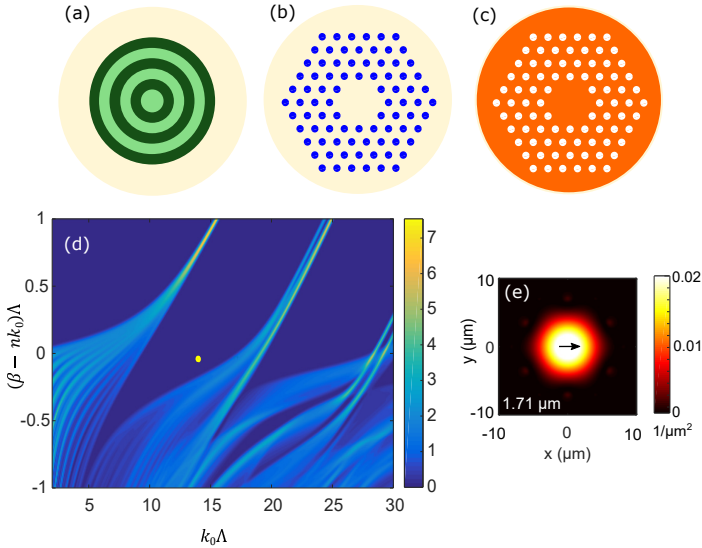
Figure 1.2: Schematics of photonic crystal fibers with periodicity in 1-D (a) and 2-D (b,c). Panel (b) represents high index strand fibers in a low index background while (c) represents a low index strand inclusions in a high index background. Panel (d) shows the density of states for a 2-D photonic crystal with a background index of $n = 1.44$ and strand index $n_{strand} = 1.59$ with pitch $\Lambda = 3.82$ μm and the radius-to-pitch radio of 0.2. Here, β denotes the propagation constant. (e) The fundamental core mode of the fiber with a defect core for the density of states plot in (d) in the first bandgap (indicated by the yellow dot in (d)) at a wavelength of 1.71 μm. The schematic of the fiber is shown in panel (b). The arrow in panel (e) indicates x polarized modes.

1.2 Bound and leaky modes

Maxwell's equations govern how electromagnetic waves travel within an optical fiber. By solving the Maxwell's equations with appropriate boundary conditions we get modes of the fiber that are described by the propagation constant β. Modes are the allowed pathways for the electric and magnetic fields within the fiber. For bound modes the value of β is real while for leaky modes we get a complex β. The significance of the presence or absence of the imaginary part of β is if the mode is lossy or not.

When a mode is bound then its energy lies completely within the core. Outside the core region, the fields and hence energy in the fiber decays exponentially. Bound modes are supported by step-index fibers above the cut off frequency. The cross section over the x axis of the z component of the absolute value of the Poynting vector S_z for a bound mode is plotted in Fig. 1.3

(b) for a step-index fiber with radius $r = 1$ μm. The core index is 1.45 and the cladding index is 1. Note that completely bound modes are only theoretically possible. In fabricated fibers, due to fabricational errors, material impurities, bending of the fiber and other scattering processes, losses are always induced into the fiber and the mode is not perfectly confined.

In the case of leaky modes, which has a complex β, the mode is not perfectly guided within the core and leaks out to the exterior. Due to this leakage of fields and thus energy to the exterior, the fields in the exterior grow in space as we move away from the fiber core. However, these leaky modes satisfy causality because the farther away from the fiber we move, more energy that had escaped from the fiber at a previous point in the z direction accumulates (see Fig. 1.4). Most fibers support leaky modes like capillary and photonic crystal fibers. Even bound modes of step-index fibers become leaky below the cutoff frequency. The cross section of S_z over the x axis of the fundamental core mode of a capillary fiber with core index 1 and cladding index 1.45 is shown in Fig. 1.3 (a), where the growth of energy in the exterior is evident.
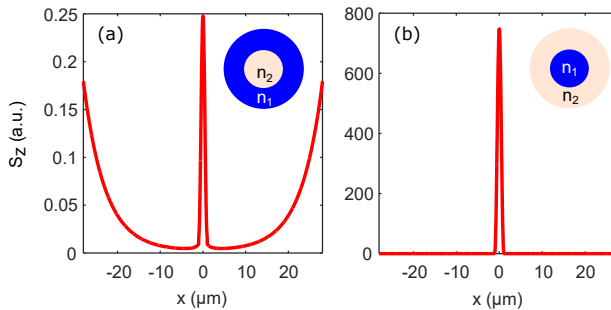

Figure 1.3: The absolute value of the z component of the time averaged Poynting vector of the fundamental core mode as a function of the x axis for a capillary fiber (a) and a step-index fiber (b). The radius of the fiber is 1 μm and the wavelength is 0.8 μm. As shown in the schematic in the insets of (a) and (b), the refractive indices of the core and cladding have been inverted to form the step-index and capillary fibers. Here, $n_1 = 1.45$ and $n_2 = 1$. We observe that the capillary fiber has fields that grow away from the fiber core while the step-index fiber has fields that decay in the homogeneous exterior.
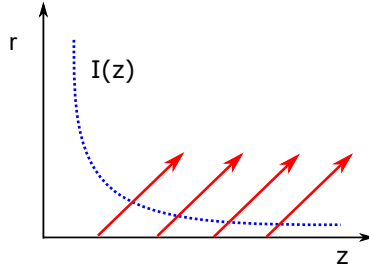
Figure 1.4: Schematic of the decrease in intensity (blue dotted line) with respect to the axial *z* direction. This decrease in intensity is then radiated to the *xy* plane (red arrows).

1.3 Perturbation theories

Perturbation theory is an approximate method that provides the solutions of a so-called complicated system by using the solutions of a simpler system. Historically, perturbation theories were very essential as computational capabilities were low and real world problems were not easily analytically solvable. However, even with the current computational cabilities perturbation theories have proved to be useful in giving deeper physical insights into the problems of interest. They are sometimes faster in giving results for complicated problems than full numerical simulations [18–21], which is highly useful in design optimization of structures.

Perturbation theories were most common in quantum mechanics [22], because the normalization of the wavefunction is very well defined and the operators are Hermitian, which results in real eigenvalues. The normalization is a key factor in any perturbation theory as differential equations (like the Schroedinger equation) give solutions only upto an arbitrary constant factor. Hence, to assign the correct weight to each solution they must be normalized correctly. In quantum mechanics, the normalization of the wavefunction is defined as

$$\int_{-\infty}^{\infty} |\psi_n^{(0)}|^2 d^3\mathbf{r} = 1 \tag{1.1}$$

due to the probabilistic nature of the wavefunction $\psi_n^{(0)}$. The most famous perturbation theory, the Rayleigh-Schroedinger perturbation theory [23], uses a power series expansion for the eigenenergy E_n and wavefunction ψ_n of the perturbed system in terms of the unperturbed system as

$$E_n = E_n^{(0)} + \lambda E_n^{(1)} + \lambda^2 E_n^{(2)} + ... \tag{1.2}$$

and

$$\psi_n = \psi_n^{(0)} + \lambda \psi_n^{(1)} + \lambda^2 \psi_n^{(2)} + ... \tag{1.3}$$

where $E_n^{(0)}$ and $\psi_n^{(0)}$ are, respectively, the eigenvalues and eigenvectors of the unperturbed system and $E_n^{(m)}$ and $\psi_n^{(m)}$ are the correction terms to the mth order. The perturbation is taken to be λV, to give the perturbed Schroedinger equation as

$$\mathbb{H}\psi_n = (\mathbb{H}_0 + \lambda V)\psi_n = E_n \psi_n \tag{1.4}$$

where $\mathbb{H}_0$ is the unperturbed Hamiltonian. By substituting the expansions of Eqs. (1.2) and (1.3) in Eq. (1.4) and equating different orders of λ, we obtain with some additional mathematics, the correction terms in Eqs. (1.2) and (1.3). The artificial factor λ is introduced to switch the perturbation "on" and "off", as when $\lambda \to 0$, we go to the unperturbed system and its maximum value of $\lambda = 1$ describes the full perturbation.

Another lesser known perturbation theory in quantum mechanics is the Brillouin-Wigner perturbation theory [24], which expresses the wavefunctions of the perturbed system as a linear superposition over the complete set of wavefunctions of the unperturbed system, i.e.,

$$\psi_{n'} = \sum_n a_n \psi_n^{(0)}. \tag{1.5}$$

Substituting this expansion in Eq. (1.4), and taking $\lambda \to 1$, we have

$$\sum_n a_n(E_{n'} - E_n^{(0)})\psi_n^{(0)} = \sum_n a_n V \psi_n^{(0)}. \tag{1.6}$$

Considering the perturbation till the mth order, we multipy the above equation by $\psi_m^{(0)*}$ and integrate over all space. This results in an iterative solution for the energy of the perturbed system upto the mth order which can be easily solved. Note that $*$ denotes complex conjugated quantities.

Perturbation theories in electromagnetism are much less common since the solutions of open optical systems support leaky modes and the operators are in general non-Hermitian. As with the case of leaky modes in fiber geometries, these modes radiate energy to the far field and hence have growing fields as we move away from the system. Normalizing the fields as an integral over all space diverges [25]. Even in quantum mechanics, decaying states with a complex eigenvalue grow exponentially in the exterior and cannot be normalized [26].

Recently, the problem of normalizing leaky modes in many open optical systems of 1-, 2- and 3-D has been solved by using an analytical normalization formulated from the Mittag-Leffler expansion and the reciprocity theorem [25]. With this normalization, perturbation theories in open optical

systems called resonant state expansion (RSE) have been developed, which treat the resonant states of the perturbed system as a linear superposition of the resonant states of the unperturbed system similar to the Brillouin-Wigner perturbation theory in quantum mechanics. This results in a matrix eigenvalue problem, which can be very easily solved numerically. Note that in real calculations a truncated basis is used to form the eigenvalue problem. Resonant states are the solutions of the Maxwell's equations in the absence of source terms satisfying outgoing boundary conditions and form a discrete set of poles in the complex β plane.

The resonant state expansion has been applied to many optical systems [27, 28] such as 3-D spheres, planar waveguides [18], dispersive materials [21, 29] and has proven to be capable of predicting the solutions of the perturbed system to a very high level of accuracy. It has also been extended to periodic systems like arrays of nano-antennas [30, 31] and anisotropic, magnetic and chiral systems [32]. In Fig. 1.5, we show the calculations done by T. Weiss et al. in Ref. [31], for a periodic array of nano-antennas. They compare the resonance energy and linewidth of a perturbed system, where the antennas have been shifted over by s nm [see Fig. 1.5 (a) and (b)], to the full numerical solutions using the Fourier modal method (FMM). We see from panels (b-e) of Fig. 1.5, that there is a very good agreement between the exact numerical solutions and the approximated perturbation theory.

1.4 How the thesis is distributed

In this thesis, we develop a perturbation theory for propagating modes in fiber structures. For this we use the resonant state expansion formalism and adapt it to fiber geometries.

In Chapter 2, we derive the analytical normalization for bound and leaky modes in fibers. This normalization is then used to gauge the correct weight of the modes in the expansion of the Green's dyadic in terms of the resonant states.

In Chapter 3, we derive the resonant state expansion for structural perturbations in fiber structures. We illustrate the effectiveness of the resonant state expansion by comparing the results with exact analytical and numerical solutions. This is done for different fiber structures like capillary and photonic crystal fibers that support leaky modes.

In Chapter 4, we show that the previously derived perturbation theory is only applicable for perturbations in the interior. We derive a new first-order perturbation theory, by using the resonant states of the system, for material perturbations in the homogeneous exterior, like changes in permittivity and permeability. We also develop the first-ever perturbation theory that treats
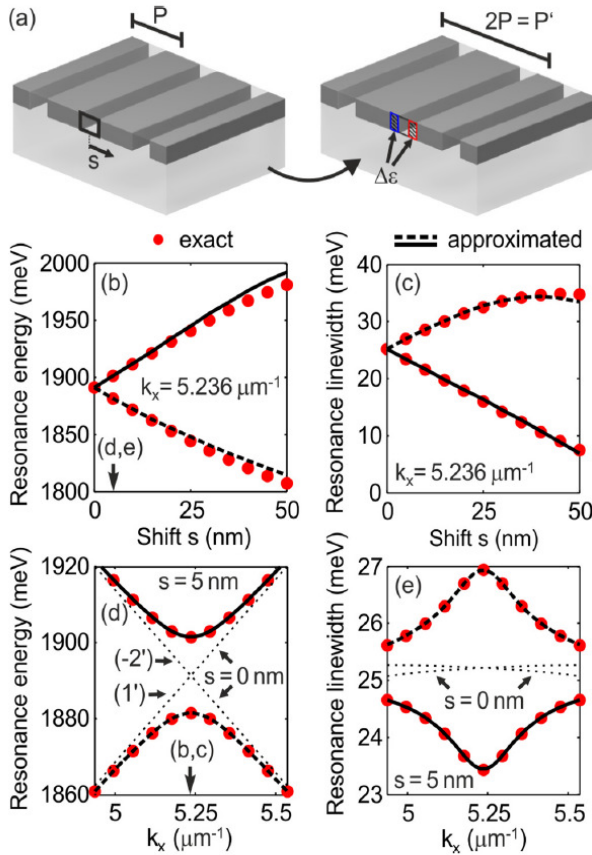
Figure 1.5: The schematic of a periodic array of nano-antennas with a shift of s nm (a), which results in a perturbation of $\Delta\varepsilon$ as shown in (b). The comparison of the resonance energy and linewidth as a function of shift s and k_x is displayed in panels (b-e). It is seen that the resonant state expansion provides a very good agreement with the full numerical solutions. The following figure is taken from Ref. [31] with permission from the publisher (American Physical Society).

wavelength as a perturbation for leaky modes, which allows quick calculations of important fiber parameters. We apply this to different fiber systems like capillary fibers, photonic crystal fibers and light cage structures.

In Chapter 5, we discuss losses in photonic bandgap fibers and how to improve confinement loss in high-index photonic bandgap fibers in first and higher order bandgaps. We provide design rules to reduce confinement loss by orders of magnitude by modifying the core surround. We show that our method can be applied to different fiber geometries by doing a parametric analysis of structural changes such as strand radius and period.

In Chapter 6, we show additional applications of the normalization derived in the previous chapters. We briefly discuss how it can be used to redefine the Kerr non-linearity parameter. We also show that the normalization is useful for theoretically calculating parameters, like fraction of fields in the strands of a fiber, which are not experimentally available.

In Chapter 7, we conclude our work and provide a brief outlook for further applications of the developed theories.

2 Analytical normalization of leaky modes in optical fibers

Most of the time I am sunk in thought, but at some point on each walk there comes a moment when I look up and notice, with a kind of first-time astonishment, the amazing complex delicacy of the world, the casual ease with which elemental things come together to form a composition that is-whatever the season, wherever I put my besotted gaze-perfect.

Walk in the woods, Bill Bryson

Parts of this work is already published in *S. Upendar, I. Allayarov, M. A. Schmidt, and T. Weiss, "Analytical mode normalization and resonant state expansion for bound and leaky modes in optical fibers-an efficient tool to model transverse disorder," Opt. Express* **26**, *22536–22546 (2018)*.

2.1 Introduction

In order to develop a perturbation theory for propagating modes in fibers or compare field distributions of different modes in fiber structures, the normalization is a very important quantity. The normalization integral for bound modes in fiber structures is [33]

$$N_n = \frac{c}{8\pi} \int_R dA \, Re(E_{n\rho} H^*_{n\phi} - E_{n\phi} H^*_{n\rho}). \qquad (2.1)$$

The integral is taken over a circle of radius R outside the region of spatial inhomogeneities. The integrand is the z component of the time averaged Poynting vector S_z with the $*$ denoting complex conjugated quantities. Since the fields of bound modes decay exponentially as we move away from the fiber structure, taking the limit of $R \rightarrow \infty$ gives a constant value for N_n. Fiber structures such as photonic bandgap fibers, capillary fibers, hollow core photonic crystal fibers and so on, support leaky modes. Leaky modes or quasinormal modes radiate energy to the far field and hence have fields that grow as we move away from the fiber. Examples of fibers with leaky modes are shown in Fig. 2.1 (a) and (b), for a capillary fiber and a photonic crystal fiber, respectively. The absolute value of the time-averaged S_z is plotted in Fig. 2.1 (a) for a capillary fiber with $n_{\text{core}} = 1$ and $n_{\text{clad}} = 1.44$ and $r = 1$ μm for the fundamental core mode. The time averaged S_z for a higher order mode is plotted in Fig. 2.1 (b) with index of inclusions as 1 and the background index as 1.44. The period is $\Lambda = 2.3$ μm with the radius of inclusions being $r = 0.25$ μm. The wavelength used for both the structures is 1 μm. From the figure, it is clear that the normalization of Eq. (2.1) will diverge when $R \rightarrow \infty$. Otherwise, we would have a normalization constant dependent on the radius of integration.

This problem of normalization of leaky modes is not new. It is also not just limited to fiber geometries. Hence, many work-arounds to this fundamental problem have been developed such as applying perfectly matched layers (PMLs) or complex coordinate transformations in the exterior. In the paper by C. Sauvan et al. in Ref. [34], the demonstration of perfectly matched layers on quasinormal or leaky modes of an open cavity is shown. The exponential growth of the fields in the homogeneous exterior due to leaky modes is completely suppressed by the addition of the perfectly matched layers and the
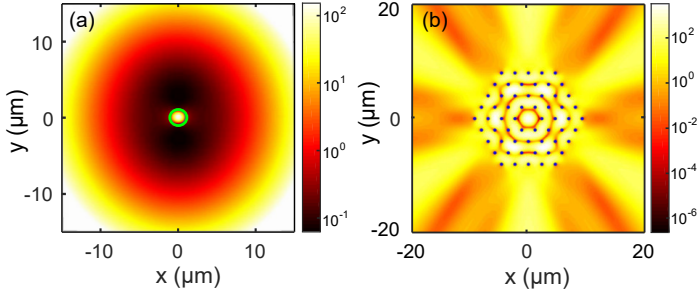
Figure 2.1: (a) Axial component of the time-averaged Poynting vector of the fundamental core mode of a step-index fiber with refractive indices of 1 and 1.44 in the core and cladding region, respectively, and a core radius of 1 μm (core region indicated by the green solid line) at a wavelength of 1 μm. (b) Axial component of the time-averaged Poynting vector for a higher-order core mode of a silica-air photonic crystal fiber with four rings of air holes of radius 0.25 μm and pitch 2.3 μm around a single-defect core. The refractive index of silica is taken as 1.44. The considered wavelength is 1 μm. Both modes in (a) and (b) exhibit fields that grow in the exterior with distance from the core.

integral for the normalization now includes this region of PMLs. Note that the addition of the PMLs keeps the outgoing boundary condition of the leaky modes intact. The key problem with this work around is that it may not be easy to implement PMLs in all mode solvers. Also, the use of PMLs gives rise to additional modes in the structure that may not be physical modes. Another solution is the complex coordinate transformation proposed by R. Sammut and A. W. Synder in Ref. [35], where the contour of integration is taken to the complex plane such that the growth due to the imaginary propagation constant is negated in the complex plane. Note that in Ref. [35], the real valued Poynting vector is used instead of the time averaged one of Eq. (2.1). However, it is mathematically taxing to apply these complex coordinate transformations, which are similar to PMLs, but from a different viewpoint.

Analytical normalizations have already been successfully derived for many open optical systems supporting leaky modes [25, 27, 28]. Here, we apply a similar approach for propagating modes in fiber geometries and obtain an analytical expression for the normalization which can be applied to leaky as well as bound solutions as a simple post processing step.

2.2 Deriving the Green's dyadic

In Gaussian units, the curl Maxwell's equations can be summarized in real space and frequency domain with time dependence $\exp(-i\omega t)$ by the compact operator form

$$\underbrace{\begin{pmatrix} k_0\varepsilon & -\nabla\times \\ -\nabla\times & k_0\mu \end{pmatrix}}_{\equiv \mathbb{M}_0}\underbrace{\begin{pmatrix} \mathbf{E} \\ i\mathbf{H} \end{pmatrix}}_{\equiv \mathbb{F}} = \underbrace{\begin{pmatrix} \mathbf{J}_E \\ i\mathbf{J}_H \end{pmatrix}}_{\equiv \mathbb{J}}, \tag{2.2}$$

with electric and magnetic fields $\mathbf{E}$ and $\mathbf{H}$, respectively, permittivity and permeability tensors ε and μ, respectively, and $k_0 = \omega/c$. The right-hand side contains the electric source term $\mathbf{J}_E = -4\pi i\mathbf{j}/c$ with current density $\mathbf{j}$, and the magnetic source term $\mathbf{J}_H$ that has been introduced for the sake of symmetry.

For optical fibers, the permittivity and permeability tensors are translationally symmetric along the direction of propagation, which we choose as the z direction of our coordinate system. Defining the Fourier transform in this direction as

$$\hat{f}(\mathbf{r}_\parallel;\beta) = \frac{1}{2\pi}\int\limits_{-\infty}^{\infty} \mathrm{d}z f(\mathbf{r}_\parallel;z)e^{-i\beta z}, \tag{2.3}$$

with $\mathbf{r}_\parallel$ being the projection of $\mathbf{r}$ to the xy plane and the hat denoting Fourier transformed quantities, the Fourier transform of Eq. (2.2) yields

$$\begin{pmatrix} k_0\varepsilon & -\hat{\nabla}_\beta\times \\ -\hat{\nabla}_\beta\times & k_0\mu \end{pmatrix}\begin{pmatrix} \hat{\mathbf{E}} \\ i\hat{\mathbf{H}} \end{pmatrix} = \begin{pmatrix} \hat{\mathbf{J}}_E \\ i\hat{\mathbf{J}}_H \end{pmatrix}, \quad \text{with} \quad \hat{\nabla}_\beta \equiv \begin{pmatrix} \partial_x \\ \partial_y \\ i\beta \end{pmatrix}. \tag{2.4}$$

The Green's dyadic [36] of Eq. (2.4) satisfies the relation

$$\hat{\mathbb{M}}_0(\mathbf{r}_\parallel;\beta)\hat{\mathbb{G}}(\mathbf{r}_\parallel,\mathbf{r}'_\parallel;\beta) = \delta(\mathbf{r}_\parallel - \mathbf{r}'_\parallel), \tag{2.5}$$

and provides the solutions $\hat{\mathbb{F}}$ of Eq. (2.4) for a given source $\hat{\mathbb{J}}$ as

$$\hat{\mathbb{F}}(\mathbf{r}_\parallel) = \int \mathrm{d}\mathbf{r}'_\parallel \, \hat{\mathbb{G}}(\mathbf{r}_\parallel,\mathbf{r}'_\parallel;\beta)\hat{\mathbb{J}}(\mathbf{r}'_\parallel). \tag{2.6}$$

Resonant states are solutions of Eq. (2.4) in the absence of sources for outgoing boundary conditions with eigenvectors $\hat{\mathbb{F}}_n$ and eigenvalues β_n. This gives

$$\hat{\mathbb{M}}_0(\mathbf{r}_\parallel;\beta_n)\hat{\mathbb{F}}_n = 0. \tag{2.7}$$

Using the Mittag-Leffler theorem [37], we expand the Green's dyadic of the Maxwell's equations in terms of the resonant states, which denote a countable

number of poles in the complex β plane, as

$$\hat{\mathbb{G}}(\mathbf{r}_\parallel, \mathbf{r}'_\parallel; \beta) = \sum_n \frac{\hat{\mathbb{R}}_n(\mathbf{r}_\parallel, \mathbf{r}'_\parallel)}{\beta - \beta_n} + \Delta \hat{\mathbb{G}}_{\text{cuts}}, \tag{2.8}$$

Here, $\hat{\mathbb{R}}_n(\mathbf{r}_\parallel, \mathbf{r}'_\parallel)$ is the residue of the Green's dyadic when $\beta \to \beta_n$. Additionally, $\Delta \hat{\mathbb{G}}_{\text{cuts}}$ denotes cut contributions due to branch cuts in the involved analytical functions, which here are Bessel and Hankel functions. In the following, we will focus on the contribution of the resonant states, keeping in mind that the cut contributions can be treated in a similar manner in numerical calculations [28, 30]. This assumption is valid as long as the solutions of the Maxwell's equations, i.e., the poles are far away from the cut. To derive the exact form of this residue, we write the Maxwell's equations with a source term that vanishes at resonance, as

$$\hat{\mathbb{M}}_0(\mathbf{r}_\parallel; \beta)\hat{\mathbb{F}} = (\beta - \beta_n)\sigma_n(\mathbf{r}_\parallel). \tag{2.9}$$

The source term on the right hand side can have any arbitrary form such that it goes to zero as $\beta \to \beta_n$, and $\sigma_n(\mathbf{r}_\parallel)$ vanishes outside the region of spatial inhomogeneities. Taking the source term and convoluting it with the Green's dyadic of Eq. (2.8) in the limit of $\beta \to \beta_n$, we obtain

$$\hat{\mathbb{F}}_n(\mathbf{r}_\parallel) = \lim_{\beta \to \beta_n} \hat{\mathbb{F}}(\mathbf{r}_\parallel; \beta) = \lim_{\beta \to \beta_n} \sum_{n'} \frac{\beta - \beta_n}{\beta - \beta_{n'}} \int d\mathbf{r}'_\parallel \, \hat{\mathbb{R}}_{n'}(\mathbf{r}_\parallel, \mathbf{r}'_\parallel)\sigma_n(\mathbf{r}'_\parallel). \tag{2.10}$$

We know that

$$\lim_{\beta \to \beta_n} \frac{\beta - \beta_n}{\beta - \beta_{n'}} = \delta_{n,n'}, \tag{2.11}$$

from which we deduce that the form of the residue is

$$\hat{\mathbb{R}}_n(\mathbf{r}_\parallel, \mathbf{r}'_\parallel) = \frac{-1}{2N_n} \hat{\mathbb{F}}_n(\mathbf{r}_\parallel) \otimes \hat{\mathbb{Q}}_n(\mathbf{r}'_\parallel) \tag{2.12}$$

with

$$\int d\mathbf{r}'_\parallel \, \hat{\mathbb{Q}}_n(\mathbf{r}'_\parallel)\sigma_n(\mathbf{r}'_\parallel) = -2N_n. \tag{2.13}$$

Note that we have introduced an additional factor of -1/2 along with the normalization constant N_n for later convenience. We can now deduce the exact form of $\hat{\mathbb{Q}}_n(\mathbf{r}'_\parallel)$ from the reciprocity principle, as shown below.

Let us consider two source currents $\hat{\mathbb{J}}_1(\mathbf{r}_\parallel, \beta)$ and $\hat{\mathbb{J}}_2(\mathbf{r}_\parallel, -\beta)$ for the fields $\hat{\mathbb{F}}_1(\mathbf{r}_\parallel, \beta)$ and $\hat{\mathbb{F}}_2(\mathbf{r}_\parallel, -\beta)$, respectively. Taking the Maxwell's equations for source $\hat{\mathbb{J}}_1(\mathbf{r}_\parallel, \beta)$ and multiplying it with $\hat{\mathbb{F}}_2(\mathbf{r}_\parallel, -\beta)$ and taking the Maxwell's

equations for source $\hat{\mathbb{J}}_2(\mathbf{r}_\parallel, -\beta)$ and multiplying it with $\hat{\mathbb{F}}_1(\mathbf{r}_\parallel, \beta)$ and subtracting the two equations, we get

$$
\begin{aligned}
&\hat{\mathbb{F}}_2(\mathbf{r}_\parallel, -\beta) \cdot \hat{\mathbb{M}}_0(\mathbf{r}_\parallel, \beta)\hat{\mathbb{F}}_1(\mathbf{r}_\parallel, \beta) - \hat{\mathbb{F}}_1(\mathbf{r}_\parallel, \beta) \cdot \hat{\mathbb{M}}_0(\mathbf{r}_\parallel, -\beta)\hat{\mathbb{F}}_2(\mathbf{r}_\parallel, -\beta) \\
&= \hat{\mathbb{F}}_2(\mathbf{r}_\parallel, -\beta) \cdot \hat{\mathbb{J}}_1(\mathbf{r}_\parallel, \beta) - \hat{\mathbb{F}}_1(\mathbf{r}_\parallel, \beta) \cdot \hat{\mathbb{J}}_2(\mathbf{r}_\parallel, -\beta).
\end{aligned}
\tag{2.14}
$$

Taking symmetric permittivity and permeability tensors, i.e., $\varepsilon = \varepsilon^T$ and $\mu = \mu^T$, where the superscript T denotes transpose and using the vector identity

$$
\mathbf{B} \cdot \hat{\nabla}_k \times \mathbf{A} - \mathbf{A} \cdot \hat{\nabla}_{-k'} \times \mathbf{B} = \nabla_\parallel \cdot (\mathbf{A} \times \mathbf{B}) + i(k - k')(\mathbf{A} \times \mathbf{B})_z
\tag{2.15}
$$

where $\nabla_\parallel$ is the in-plane gradient, in Eq. (2.14) we get

$$
\begin{aligned}
&\nabla_\parallel \cdot (\hat{\mathbb{E}}_2(\mathbf{r}_\parallel, -\beta) \times \hat{\mathbb{H}}_1(\mathbf{r}_\parallel, \beta) - \hat{\mathbb{E}}_1(\mathbf{r}_\parallel, \beta) \times \hat{\mathbb{H}}_2(\mathbf{r}_\parallel, -\beta)) \\
&= \hat{\mathbb{F}}_2(\mathbf{r}_\parallel, -\beta) \cdot \hat{\mathbb{J}}_1(\mathbf{r}_\parallel, \beta) - \hat{\mathbb{F}}_1(\mathbf{r}_\parallel, \beta) \cdot \hat{\mathbb{J}}_2(\mathbf{r}_\parallel, -\beta).
\end{aligned}
\tag{2.16}
$$

Integrating the above equation outside the region of spatial inhomogeneities, we see that the first line goes to zero as the fields must satisfy the same outgoing boundary conditions. This then results in

$$
\int d\mathbf{r}_\parallel(\hat{\mathbb{F}}_2(\mathbf{r}_\parallel, -\beta) \cdot \hat{\mathbb{J}}_1(\mathbf{r}_\parallel, \beta) - \hat{\mathbb{F}}_1(\mathbf{r}_\parallel, \beta) \cdot \hat{\mathbb{J}}_2(\mathbf{r}_\parallel, -\beta)) = 0.
\tag{2.17}
$$

Writing $\hat{\mathbb{F}}_1(\mathbf{r}_\parallel, \beta)$ and $\hat{\mathbb{F}}_2(\mathbf{r}_\parallel, -\beta)$ in terms of the Green's dyadic from Eq. (2.6), we have

$$
\int d\mathbf{r}_\parallel \hat{\mathbb{G}}(\mathbf{r}_\parallel, \mathbf{r}'_\parallel; -\beta)\hat{\mathbb{J}}_2(\mathbf{r}_\parallel, -\beta) \cdot \hat{\mathbb{J}}_1(\mathbf{r}_\parallel, \beta) - \hat{\mathbb{G}}(\mathbf{r}_\parallel, \mathbf{r}'_\parallel; \beta)\hat{\mathbb{J}}_1(\mathbf{r}_\parallel, \beta) \cdot \hat{\mathbb{J}}_2(\mathbf{r}_\parallel, -\beta) = 0.
\tag{2.18}
$$

To satisfy the above equation for arbitrary sources, we must have

$$
\hat{\mathbb{G}}(\mathbf{r}_\parallel, \mathbf{r}'_\parallel; \beta) = \hat{\mathbb{G}}^T(\mathbf{r}_\parallel, \mathbf{r}'_\parallel; -\beta),
\tag{2.19}
$$

which results in

$$
\hat{\mathbb{Q}}(\mathbf{r}_\parallel) = \hat{\mathbb{F}}(\mathbf{r}_\parallel, -\beta) \equiv \hat{\mathbb{F}}^R(\mathbf{r}_\parallel).
\tag{2.20}
$$

Hence, the Green's dyadic can be written as

$$
\hat{\mathbb{G}}(\mathbf{r}_\parallel, \mathbf{r}'_\parallel; \beta) = -\sum_n \frac{\hat{\mathbb{F}}_n(\mathbf{r}_\parallel) \otimes \hat{\mathbb{F}}_n^R(\mathbf{r}'_\parallel)}{2N_n(\beta - \beta_n)},
\tag{2.21}
$$

with $\otimes$ denoting the outer vector product, and N_n being the normalization constant in order to assign the appropriate weight to the resonant states, since Eq. (2.7) provides the resonant field distributions only up to a constant factor. The superscript R denotes the reciprocal conjugate resonant state, which is a solution of Eq. (2.7) at $-\beta_n$. Note that Eq. (2.21) is only valid within the regions of spatial inhomogeneities of the fiber, where the leaky modes do not exhibit any growth.

2.3 Normalization

We start similar to the Green's dyadic derivation, with the Maxwell's equation and a source term that vanishes at resonance as in Eq. (2.9). The source term $\sigma_n(\mathbf{r}_\parallel)$ is again chosen to vanish outside the region of spatial inhomogeneities. The source term is then convoluted with the Green's dyadic resulting in Eq. (2.10) at the limit $\beta \to \beta_n$ with $\hat{\mathbf{Q}}_n(\mathbf{r}'_\parallel) \equiv \hat{\mathbb{F}}_n^R(\mathbf{r}'_\parallel)$ satisfying Eq. (2.13).

To derive the normalization equation, we multiply Eq. (2.9) with $\hat{\mathbb{F}}_n^R(\mathbf{r}_\parallel)$ and subtract a zero in the form of

$$0 = \hat{\mathbb{F}}(\mathbf{r}_\parallel; \beta) \cdot \hat{\mathbb{M}}_0(\mathbf{r}_\parallel; -\beta_n)\hat{\mathbb{F}}_n^R(\mathbf{r}_\parallel), \tag{2.22}$$

to obtain,

$$\hat{\mathbb{F}}_n^R(\mathbf{r}_\parallel)\cdot\hat{\mathbb{M}}_0(\mathbf{r}_\parallel;\beta)\hat{\mathbb{F}}(\mathbf{r}_\parallel;\beta)-\hat{\mathbb{F}}(\mathbf{r}_\parallel;\beta)\cdot\hat{\mathbb{M}}_0(\mathbf{r}_\parallel;-\beta_n)\hat{\mathbb{F}}_n^R(\mathbf{r}_\parallel) = (\beta-\beta_n)\hat{\mathbb{F}}_n^R(\mathbf{r}_\parallel)\cdot\sigma_n(\mathbf{r}_\parallel). \tag{2.23}$$

Dividing by $\beta - \beta_n$, integrating over the spatial inhomogeneities in the limit $\beta \to \beta_n$, and using that $\varepsilon^T = \varepsilon$ as well as $\mu^T = \mu$ for reciprocal systems, we get

$$-2N_n = \lim_{\beta \to \beta_n} \int d\mathbf{r}_\parallel \frac{-i}{\beta - \beta_n} \nabla_\parallel \cdot [\hat{\mathbf{E}}(\mathbf{r}_\parallel;\beta) \times \hat{\mathbf{H}}_n^R(\mathbf{r}_\parallel) - \hat{\mathbf{E}}_n^R(\mathbf{r}_\parallel) \times \hat{\mathbf{H}}(\mathbf{r}_\parallel;\beta)]$$
$$+ \int d\mathbf{r}_\parallel [\hat{\mathbf{E}}_n(\mathbf{r}_\parallel) \times \hat{\mathbf{H}}_n^R(\mathbf{r}_\parallel) - \hat{\mathbf{E}}_n^R(\mathbf{r}_\parallel) \times \hat{\mathbf{H}}_n(\mathbf{r}_\parallel)]_z. \tag{2.24}$$

Here, we have used the vector identity of Eq. (2.15). The subscript z indicates the integration of the z component in the second term. The first term can be converted to a line integral by using the divergence theorem. The curve of integration can be taken as a circle of radius R outside the region of inhomogeneities. This gives,

$$-2N_n = \lim_{\beta \to \beta_n} \int \hat{\rho} \cdot d\phi \frac{-iR}{\beta - \beta_n} [\hat{\mathbf{E}}(\mathbf{r}_\parallel;\beta) \times \hat{\mathbf{H}}_n^R(\mathbf{r}_\parallel) - \hat{\mathbf{E}}_n^R(\mathbf{r}_\parallel) \times \hat{\mathbf{H}}(\mathbf{r}_\parallel;\beta)]$$
$$+ \int d\mathbf{r}_\parallel [\hat{\mathbf{E}}_n(\mathbf{r}_\parallel) \times \hat{\mathbf{H}}_n^R(\mathbf{r}_\parallel) - \hat{\mathbf{E}}_n^R(\mathbf{r}_\parallel) \times \hat{\mathbf{H}}_n(\mathbf{r}_\parallel)]_z. \tag{2.25}$$

For evaluating the limit $\beta \to \beta_n$, we carry out a Taylor expansion around β_n as

$$\hat{\mathbb{F}}(\mathbf{r}_\parallel;\beta) = \hat{\mathbb{F}}_n(\mathbf{r}_\parallel)+(\beta-\beta_n)\frac{\partial \hat{\mathbb{F}}(\mathbf{r}_\parallel;\beta)}{\partial \beta}\bigg|_{\beta_n} + \frac{(\beta - \beta_n)^2}{2} \frac{\partial^2 \hat{\mathbb{F}}(\mathbf{r}_\parallel;\beta)}{\partial \beta^2}\bigg|_{\beta_n} + \dots . \tag{2.26}$$

Substituting Eq. (2.26) in Eq. (2.25), we get two line integral, one which contains terms of $\hat{\mathbb{F}}_n$ and $\hat{\mathbb{F}}_n^R$ and the other which has its first order derivative with respect to β. The higher order terms go to zero. We write the first line term as

$$\int \hat{\rho} \cdot \mathrm{d}\phi \; \frac{-iR}{\beta - \beta_n} [\hat{\mathbf{E}}_n(\mathbf{r}_\parallel) \times \hat{\mathbf{H}}_n^R(\mathbf{r}_\parallel) - \hat{\mathbf{E}}_n^R(\mathbf{r}_\parallel) \times \hat{\mathbf{H}}_n]. \tag{2.27}$$

When using that, due to symmetry, the in-plane components of the electric field and the z component of the magnetic field of resonant states with eigenvalues β_n and $-\beta_n$ are identical, while we have to multiply all other components with -1 in order to convert $\hat{\mathbb{F}}_n^R$ into $\hat{\mathbb{F}}_n$, the above equation goes to zero. Therefore, only the line integral with the first-order derivatives with respect to β remain. Hence, the normalization expression reduces to

$$N_n = \frac{\beta_n R}{2i\varkappa_n} \int\limits_0^{2\pi} \mathrm{d}\phi \left(\frac{\partial \hat{E}_{n,\phi}}{\partial \varkappa} \hat{H}_{n,z} + \frac{\partial \hat{E}_{n,z}}{\partial \varkappa} \hat{H}_{n,\phi} - \frac{\partial \hat{H}_{n,\phi}}{\partial \varkappa} \hat{E}_{n,z} - \frac{\partial \hat{H}_{n,z}}{\partial \varkappa} \hat{E}_{n,\phi} \right)$$
$$+ \int \mathrm{d}\mathbf{r}_\parallel \, (\hat{E}_{n,\rho} \hat{H}_{n,\phi} - \hat{E}_{n,\phi} \hat{H}_{n,\rho}). \tag{2.28}$$

Here $\varkappa_n$ denotes the radial propagation constant. We have converted the derivative with respect to β to a derivative with respect to $\varkappa$ by using the relation

$$\varkappa_n^2 = \varepsilon \mu k_0^2 - \beta_n^2. \tag{2.29}$$

From solving the Maxwell's equations in homogeneous and isotropic media, we know that the z component of the outgoing electric and magnetic fields have the form [33, 45]

$$\hat{E}_z = \sum_n \hat{E}_{0n} H_n^{(1)}(\varkappa\rho) e^{in\phi}, \tag{2.30}$$

$$\hat{H}_z = \sum_n \hat{H}_{0n} H_n^{(1)}(\varkappa\rho) e^{in\phi}, \tag{2.31}$$

where $H_n^{(1)}(x)$ denotes the Hankel functions of the first kind. The coefficients $\hat{E}_{0n}$ and $\hat{H}_{0n}$ correspond to transverse magnetic and transverse electric fields respectively, while the full fields are a superposition of the two contributions. Due to the dependence of the z component of the fields solely on ρ and $\varkappa$, the derivative with respect to $\varkappa$ can be converted to spatial derivatives by using the following relations:

$$\frac{\partial \hat{E}_z}{\partial \varkappa} = \frac{\rho}{\varkappa} \frac{\partial \hat{E}_z}{\partial \rho}, \qquad \frac{\partial \hat{H}_z}{\partial \varkappa} = \frac{\rho}{\varkappa} \frac{\partial \hat{H}_z}{\partial \rho}. \tag{2.32}$$

The $\hat{E}_\phi$ and $\hat{H}_\phi$ field components can be derived from the $\hat{E}_z$ and $\hat{H}_z$ field components as [47]

$$\hat{E}_\phi = \frac{i\beta}{\varkappa^2 \rho} \frac{\partial \hat{E}_z}{\partial \phi} - \frac{ik_0\mu}{\varkappa^2} \frac{\partial \hat{H}_z}{\partial \rho}, \qquad \hat{H}_\phi = \frac{i\beta}{\varkappa^2 \rho} \frac{\partial \hat{H}_z}{\partial \phi} + \frac{ik_0\varepsilon}{\varkappa^2} \frac{\partial \hat{E}_z}{\partial \rho}, \qquad (2.33)$$

and they can be differentiated with respect to $\varkappa$ by using the relations for $\hat{E}_z$ and $\hat{H}_z$ given in Eq. (2.32). Substituting in Eq. (2.28) $\hat{E}_\phi$ and $\hat{H}_\phi$ by Eq. (2.33) and using that

$$\int\limits_0^{2\pi} \mathrm{d}\phi \, \frac{\partial f}{\partial \phi} g = - \int\limits_0^{2\pi} \mathrm{d}\phi \, f \frac{\partial g}{\partial \phi}, \qquad (2.34)$$

with f and g being components of $\hat{\mathbf{E}}_n$ and $\hat{\mathbf{H}}_n$, respectively, we arrive at

$$N_n = S_n + L_n, \qquad (2.35)$$

with the surface term

$$S_n = \int\limits_0^R \rho\mathrm{d}\rho \int\limits_0^{2\pi} \mathrm{d}\phi \, (\hat{E}_{n,\rho}\hat{H}_{n,\phi} - \hat{E}_{n,\phi}\hat{H}_{n,\rho}), \qquad (2.36)$$

which is proportional to the integral over the z component of the real-valued Poynting vector, and the line term

$$
\begin{aligned}
L_n = & \frac{\varepsilon\mu k_0^2 + \beta_n^2}{2\varkappa_n^4} \int\limits_0^{2\pi} \mathrm{d}\phi \left(\hat{E}_{n,z}\frac{\partial \hat{H}_{n,z}}{\partial \phi} - \hat{H}_{n,z}\frac{\partial \hat{E}_{n,z}}{\partial \phi} \right)_R \\
& + \frac{k_0\beta_n R^2}{2\varkappa_n^4} \int\limits_0^{2\pi} \mathrm{d}\phi \left\{ \mu\left[\left(\frac{\partial \hat{H}_{n,z}}{\partial \rho}\right)^2 - \rho\hat{H}_{n,z}\frac{\partial}{\partial \rho}\left(\frac{1}{\rho}\frac{\partial \hat{H}_{n,z}}{\partial \rho}\right) \right] \right. \\
& + \left. \varepsilon\left[\left(\frac{\partial \hat{E}_{n,z}}{\partial \rho}\right)^2 - \rho\hat{E}_{n,z}\frac{\partial}{\partial \rho}\left(\frac{1}{\rho}\frac{\partial \hat{E}_{n,z}}{\partial \rho}\right) \right] \right\}_R,
\end{aligned}
\qquad (2.37)
$$

where the subscript R indicates that the integrand is evaluated at radius R.

Note that this normalization is applicable for both bound as well as leaky modes. For bound modes, due to the exponential decay of the fields in the exterior, the line term automatically goes to zero. This can be seen in Fig. 2.2 (b) for a step-index fiber with core index 1.20 and cladding index 1. The radius of the core is 0.3 μm. The absolute value of S_z for the fundamental core mode is plotted in Fig. 2.2 (a) at a wavelength of 1 μm. We see in Fig. 2.2 (b), that the radius of normalization needs to span over nearly 6 times the
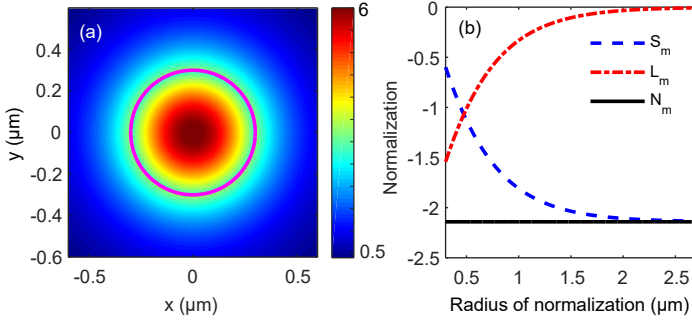
Figure 2.2: (a) Axial component of the time-averaged Poynting vector of the fundamental core mode (in a.u.) for a single ring fiber with refractive indices of 1.20 (theoretical value) and 1.00 in the core and cladding region, respectively at a wavelength of 1.00 μm. The effective index of the mode is $n_{\text{eff}} = 1.0174$. The radius of the core is 0.3 μm denoted by the magenta line. (b) The normalization as a function of the radius of normalization. The surface term (blue dashed line) and line term (red dotted-dashed line) of the normalization Eq. (2.35) are also plotted in (b). We see that the exponential decay of the surface and line terms occurs far away from the core radius.

radius of the core for the surface term (blue dashed line) to converge to the normalization (with an absolute error of 10^{-3}) and the line term (red dashed dotted line) to go to zero. However, the analytical normalization (black solid line) is independent of the radius of integration, which drastically helps to reduce the computational domain.

In Fig. 2.3 (a) we show the z component of the absolute value of the Poynting vector for a higher order mode of a capillary fiber with $n_{\text{core}} = 1$ and $n_{\text{clad}} = 1.45$. The radius of the fiber is $r = 5$ μm and the wavelength is 1 μm. The effective index of the shown mode is $0.3861 + 0.0690i$. Since, this mode has a complex effective index n_{eff} that is related to the propagation constant as $\beta = k_0 n_{\text{eff}}$ where k_0 denotes the wavenumber, the shown mode is leaky with fields that grow in the exterior. In panels (c) and (d) the real and imaginary parts of the line and surface integrals of the normalization are plotted as a function of the radius of normalization for the considered leaky fiber mode as shown in (a). We see that as we move away from the fiber core the surface term diverges, but the divergence of the line term completely balances out the divergence of the surface term so that their sum provides a constant value, as seen in the black line for both the real and imaginary parts. Since the normalization should be a constant value hence, we can say from Eq. (2.35), that

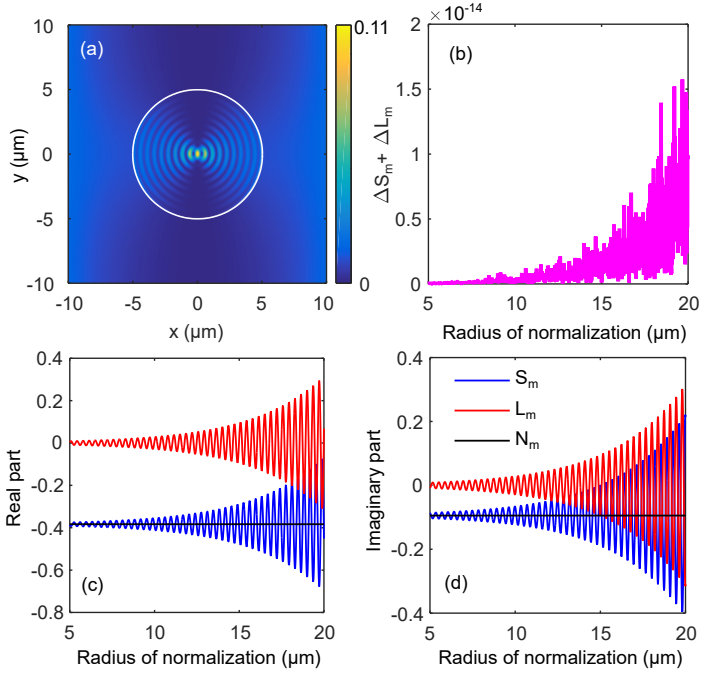$$\Delta S_m + \Delta L_m = 0, \tag{2.38}$$

Figure 2.3: (a) Axial component of the time-averaged Poynting vector of a higher order mode of a capillary fiber (in a.u.) with refractive indices of 1 and 1.45 in the core and cladding region, respectively, and a core radius of 5 μm (core region indicated by the white solid line) at a wavelength of 1 μm. The effective index of the mode is $n_{\text{eff}} = 0.3861 + 0.0690i$. (b) The sum of the change in the surface term and the line term, which theoretically should be zero due to the constant normalization as a function of radius of normalization. The bottom panels depict the real (c) and imaginary (d) parts of the surface term (blue solid line) and line term (red solid line) and the normalization Eq. (2.35) (black solid line) as a function of the radius of normalization. Evidently, the divergence of the fields is manifested in the surface and line terms, while it is countervailed in their sum as the normalization constant.

where ΔS_m and ΔL_m represent the change in the surface and line integral terms as a function of the radius of normalization. This sum is plotted in Fig. 2.3 (b). The expression of the surface and line terms are evaluated analytically. Our calculation of Eq. (2.38) gives values to the order of 10^{-14}, which is the computational precision of our numerical method.
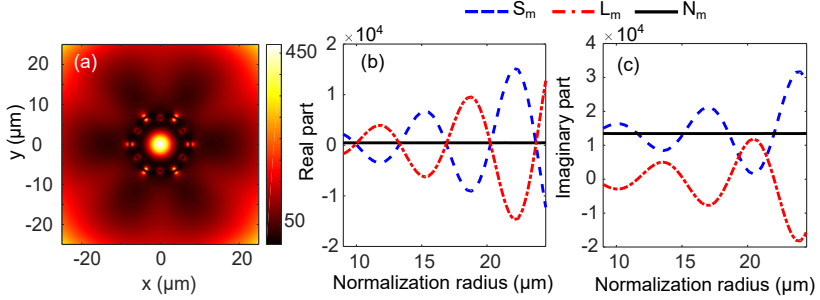

Figure 2.4: (a) Axial component of the time-averaged Poynting vector of the fundamental core mode (in a.u.) of a single ring fiber with refractive indices of 1.62 and 1.44 in the inclusions and background region, respectively at a wavelength of 1.48 μm. The effective index of the mode is $n_{\text{eff}} = 1.436 + 1.138e - 03$. The panels (b) and (c) depict the real and imaginary parts, respectively of the surface term (blue dashed line) and line term (red dotted-dashed line) of the normalization of Eq. (2.35) as a function of the normalization radius. We see that even for a more complex structure taking the surface and line integrals outside the region of spatial inhomogeneities gives a constant normalization (black solid line).

We now move to a structure which cannot be solved analytically and it doesn't possess a clearly marked distinction between the core and the homogeneous cladding as in the case of the capillary fiber structure. We select a single ring 12 strand fiber with index of inclusions as 1.62 placed in a background index of 1.44. The radius of the strands are 0.764 μm and the pitch is 3.82 μm. The fundamental core mode at a wavelength of 1.48 μm is plotted in Fig. 2.4 (a), where the absolute value of S_z is plotted in arbitrary units. The plots of the real and imaginary parts of the surface and line integral and their sum as a function of the normalization radius is plotted in Fig. 2.4 (b) and (c), respectively. The radius of normalization in the x axis is chosen such that it encloses all regions of spatial inhomogeneities from the lower limit. We see that we get a constant normalization for increasing values of surface and line integrals with increasing radius of integration.

In conclusion, in this chapter we have derived the Green's dyadic for propagating modes in fiber geometries from the Mittag-Lefler theorem. Using the Green's dyadic, we have arrived at the correct analytical mode normalization

for bound and leaky modes in fibers. We have demonstrated that the analytical normalization is constant with respect to the radius of integration for modes of different fiber structures.

3 Resonant state expansion for propagating modes

Even if there is only one possible unified theory, it is just a set of rules and equations. What is it that breathes fire into the equations and makes a universe for them to describe? The usual approach of science, of constructing a mathematical model, cannot answer the questions of why there should be a universe for the model to describe. Why does the universe go to all the bother of existing?

A brief history of time, Stephen Hawking

Parts of this work is already published in *S. Upendar, I. Allayarov, M. A. Schmidt, and T. Weiss, "Analytical mode normalization and resonant state expansion for bound and leaky modes in optical fibers-an efficient tool to model transverse disorder," Opt. Express **26**, 22536–22546 (2018).*

3.1 Introduction

After deriving the correct analytical normalization for bound and leaky modes we now apply it to a perturbation theory where we treat perturbations in the interior of the fiber structure. This perturbation theory is based on the previously described resonant state expansion where the resonant states of a perturbed system are considered as a linear superposition of the resonant states of the unperturbed system [18, 27, 28, 38]. There are many advantages to such a perturbation theory. First, it gives a deeper understanding of which modes or resonant states interact with each other in the presence of a perturbation. Hence, it gives a deeper physical insight on how to tailor perturbations to the get desired properties from the fiber. Second, it allows to study multiple perturbations of the same underlying system. This is especially useful for studying the influence of structural disorder in fiber structures, where a statistical average over different realizations of disorder is required.

Numerical studies of fiber structures usually consider ideal fibers with perfect core and cladding designs. However, the fabrication process itself leads to multiple deviations from this ideally simulated design, which is known to affect the guiding properties of the fiber [39, 40]. This is especially prominant while fabricating photonic crystal fibers due to the high number of inclusions in their microstructured cladding. Diameter disorder is known to be the most common disorder in the fabrication of photonic crystal fibers. Simulations of these disordered fibers is computationally very taxing due to the lack of symmetry in these systems. There have been many studies in the direction of simulating actually fabricated fibers with the fabrication disorders taken into account [41–44], which use fully vectorial finite element methods.

Here, we present a perturbational approach for solving disordered systems. We consider the ideal ordered structure as the unperturbed system and the disorder is treated as the perturbation. Thereby, repeated solving of the Maxwell's equations for different realizations of disorder can be avoided, as it is time consuming for any solver. In the following chapter, we derive the perturbation theory for internal perturbations using the Green's dyadic and analytical mode normalization for propagating modes in a fiber. We then apply this perturbation theory to two test systems of a capillary fiber, which is analytically solvable and a silica-air photonic crystal fiber where we study the effects of diameter disorder on the fundamental core mode by averaging over

multiple realizations of disorder.

3.2 Theory

We start out with Maxwell's equations [with an implicit time dependence of $e^{-i\omega t}$] for the resonant states of the unperturbed system denoted with subscript n as in Eq. (2.7). We then determine the resonant states of a perturbed system (denoted by subscript ν) with perturbation $\Delta\varepsilon$ and $\Delta\mu$ that exhibits the same translational symmetry as permittivity ε and permeability μ and vanish outside the regions of spatial inhomogeneities. Hence, the perturbations are strictly internal in nature and carry forward to the axial, i.e., the z direction.

The Maxwell operator $\hat{\mathbb{M}}$ of the perturbed system can be separated into the operator $\hat{\mathbb{M}}_0$ of the unperturbed system and the deviation $\Delta\hat{\mathbb{M}}$ as $\hat{\mathbb{M}} = \hat{\mathbb{M}}_0 + \Delta\hat{\mathbb{M}}$, with

$$\Delta\hat{\mathbb{M}}(\mathbf{r}_\parallel) = \begin{pmatrix} k_0\Delta\varepsilon(\mathbf{r}_\parallel) & 0 \\ 0 & k_0\Delta\mu(\mathbf{r}_\parallel) \end{pmatrix}. \tag{3.1}$$

Thus, we can recast Eq. (2.7) in the form

$$\hat{\mathbb{M}}_0(\mathbf{r}_\parallel; \beta_\nu)\hat{\mathbb{F}}_\nu(\mathbf{r}_\parallel) = -\Delta\hat{\mathbb{M}}(\mathbf{r}_\parallel)\hat{\mathbb{F}}_\nu(\mathbf{r}_\parallel), \tag{3.2}$$

where $\hat{\mathbb{F}}_\nu$ is the resonant field distribution of a resonant state in the perturbed system with propagation constant β_ν. Since we know that the Green's dyadic of Eq. (2.7) satisfies the relation of Eq. (2.5) and provides the solutions $\hat{\mathbb{F}}$ satisfying the Maxwell's equations for an arbitrary source $\hat{\mathbb{J}}$ as in Eq. (2.6), we obtain

$$\hat{\mathbb{F}}_\nu(\mathbf{r}_\parallel) = -\int d\mathbf{r}_\parallel'\, \hat{\mathbb{G}}(\mathbf{r}_\parallel, \mathbf{r}_\parallel'; \beta_\nu)\Delta\hat{\mathbb{M}}(\mathbf{r}_\parallel')\hat{\mathbb{F}}_\nu(\mathbf{r}_\parallel'). \tag{3.3}$$

Using the form of the Green's dyadic as derived in the previous chapter, ignoring any contribution from branch cuts of the analytical functions and substituting it in the above equation, we get

$$\hat{\mathbb{F}}_\nu(\mathbf{r}_\parallel) = \sum_n \frac{1}{2N_n(\beta_\nu - \beta_n)}\, \hat{\mathbb{F}}_n(\mathbf{r}_\parallel) \int d\mathbf{r}_\parallel'\, \hat{\mathbb{F}}_n^R(\mathbf{r}_\parallel') \cdot \Delta\hat{\mathbb{M}}(\mathbf{r}_\parallel')\hat{\mathbb{F}}_\nu(\mathbf{r}_\parallel'). \tag{3.4}$$

Next, we construct the resonant states of the perturbed system as a linear combination of the normalized resonant states of the unperturbed system:

$$\hat{\mathbb{F}}_\nu(\mathbf{r}_\parallel) = \sum_n b_n^{(\nu)}\hat{\mathbb{F}}_n(\mathbf{r}_\parallel). \tag{3.5}$$

Using this ansatz in Eq. (3.4), we get

$$\sum_n b_n^{(v)} \hat{\mathbb{F}}_n(\mathbf{r}_\parallel) = \sum_n \frac{1}{2N_n(\beta_v - \beta_n)} \hat{\mathbb{F}}_n(\mathbf{r}_\parallel) \int d\mathbf{r}_\parallel' \; \hat{\mathbb{F}}_n^R(\mathbf{r}_\parallel') \cdot \Delta\hat{\mathbb{M}}(\mathbf{r}_\parallel') \sum_{n'} b_{n'}^{(v)} \hat{\mathbb{F}}_{n'}(\mathbf{r}_\parallel'). \tag{3.6}$$

Equating it for each n independently, we obtain

$$b_n^{(v)} \hat{\mathbb{F}}_n(\mathbf{r}_\parallel) = \frac{1}{2N_n(\beta_v - \beta_n)} \hat{\mathbb{F}}_n(\mathbf{r}_\parallel) \int d\mathbf{r}_\parallel' \; \hat{\mathbb{F}}_n^R(\mathbf{r}_\parallel') \cdot \Delta\hat{\mathbb{M}}(\mathbf{r}_\parallel') \sum_{n'} b_{n'}^{(v)} \hat{\mathbb{F}}_{n'}(\mathbf{r}_\parallel'), \tag{3.7}$$

which can be rewritten as,

$$\beta_v b_n^{(v)} = \beta_n b_n^{(v)} + \frac{1}{2} \sum_{n'} V_{nn'} b_{n'}^{(v)}, \tag{3.8}$$

where

$$V_{nn'} = \int d\mathbf{r}_\parallel \; \hat{\mathbb{F}}_n^R(\mathbf{r}_\parallel) \cdot \Delta\mathbb{M}(\mathbf{r}_\parallel)\hat{\mathbb{F}}_{n'}(\mathbf{r}_\parallel). \tag{3.9}$$

The above equations describe a linear eigenvalue problem with β_v as the eigenvalue with $b_n^{(v)}$ as the eigenvector. Note that the sum in Eq. (3.5) is carried out over all resonant states of the unperturbed system, but in real calculations, a truncated basis is used to expand $\hat{\mathbb{F}}_v$. The choice of the basis size has to be taken large enough to accurately account for the perturbations in the system. Note that the fields in Eq. (3.9) have been normalized according to the analytical normalization derived in Chapter 2.

It should be noted that the above equations are given in Gaussian units. However, their transformation to SI units is straight-forward: One simply has to replace the permittivity and permeability by the relative permittivity and permeability, and substitute $\mathbf{H}$ with $Z_0\mathbf{H}^{SI}$ as well as $\mathbb{J}$ with $Z_0\mathbb{J}^{SI}$, with $\mathbb{J}_E^{SI} = -i\mathbf{j}^{SI}$ and Z_0 as the vacuum impedance, while $\mathbf{E}$ has to be replaced by $\mathbf{E}^{SI}$.

3.3 Examples

We now apply this perturbation theory to two example structures of a capillary fiber and a photonic crystal fiber.

3.3.1 Capillary fiber

We consider a capillary fiber with a core refractive index of 1 and a cladding refractive index of 1.44 as our unperturbed system. The radius of the fiber is

8 µm. The fundamental HE_{11} mode and higher order modes are calculated an-alytically by solving the constitutive equations for a capillary fiber [33] with the z and ϕ components of the electric and magnetic fields being continuous over the interface.

We now introduce a perturbation into our system, which is a homogeneous change in refractive index of the fiber in the core region. Hence, the index of the core varies from n_c to $n_c + \Delta n$. The schematic of the capillary fiber with the perturbation is plotted in the inset of Fig. 3.1 (a). Since our perturbation is azimuthally symmetric, the modes required to setup the eigenvalue problem of Eq. (3.8) should have the same azimuthal order as that of the fundamental core mode, which has an azimuthal order of $m = 1$. We setup our eigen-value equation for 154 modes. This includes modes that propagate in both the forward and backward directions, i.e., with β and $-\beta$.

The solutions of the unperturbed fiber are shown in Fig. 3.1 (a) and (c) with black squares at a wavelength of 1 µm. This together comprises of all the 77 modes that are propagating in the positive z direction used to form the eigenvalue problem. Note that the Fig. 3.1 (c) is the enlarged representation of the green box plotted in Fig. 3.1 (a), in order to differentiate closely spaced modes. Similarly, Fig. 3.1 (d) is the enlarged representation of the orange box plotted in Fig. 3.1 (b).

The comparison between the resonant state expansion and analytical solu-tions is plotted in Fig. 3.1 for $\Delta n = 0.07$ in panels (a,c) and for $\Delta n = 0.17$ in panels (b,d) for fundamental and higher order modes. The fundamental mode is indicated by the arrow for both perturbations. We see that, for the fundamental core mode there is a very good agreement between the exact so-lution and resonant state expansion for both magnitudes of perturbation. The predictions from the resonant state expansion match very well with exact so-lutions for the higher order modes as well. However, the agreement for higher order modes reduces with increasing magnitude of perturbation which can be clearly seen in the enhanced axes plot of Fig. 3.1 (d) when compared to Fig. 3.1 (c). Note that the deviation from the unperturbed system is also higher for larger perturbations and hence a larger basis of modes may be needed to fully describe the system.

The relative error defined by

$$\text{Relative error} = \left| 1 - \frac{n_{\text{eff}}^{\text{RSE}}}{n_{\text{eff}}^{\text{exact}}} \right| \tag{3.10}$$

is plotted for a higher order mode with unperturbed effective index 0.03139 + 1.0103i as a function of the number of modes used to form the eigenvalue problem of Eq. (3.8) in Fig. 3.2 (b) till 20 basis states. The spatial distribution of S_z for the considered higher order core mode (in a.u.) at a wavelength of
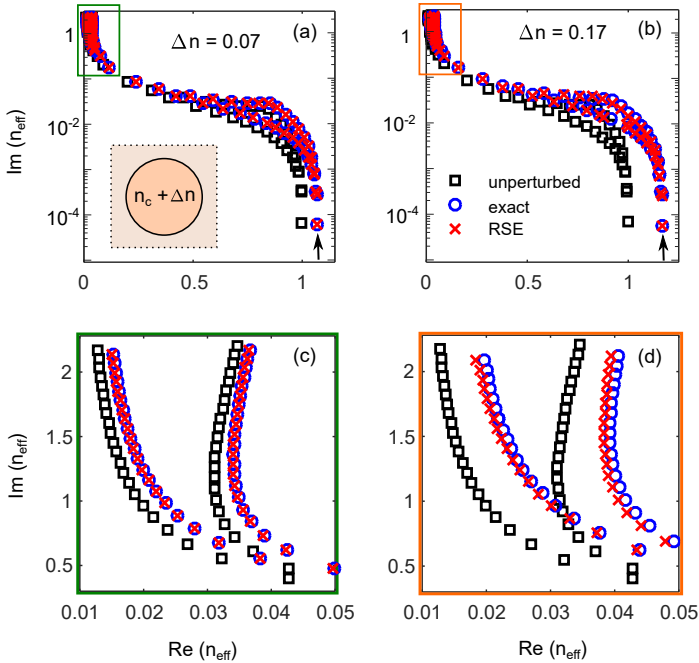
Figure 3.1: Effective refractive indices of modes in a capillary fiber with a homogeneous perturbation in the core region of (a,c) $\Delta n = 0.07$ and (b,d) $\Delta n = 0.17$. The results from the resonant state expansion (RSE, red crosses) are compared with the exact analytical solution (blue circles) for the perturbed system at a wavelength of 1 μm. The unperturbed system has a core index of 1, cladding index of 1.44, and a radius of 8 μm, with its effective refractive indices denoted by black squares. The number of modes used is 154. The black arrow indicates the fundamental core mode. The green rectangle with a high density of modes in panel (a) is enlarged in panel (c), while the orange rectangle of panel (b) is enlarged in panel (d).

1 μm is shown in Fig. 3.2 (a). We see that the error decreases monotonously with increasing number of basis states and we reach a relative error on the order of 10^{-4} and 10^{-3} for perturbations of $\Delta n = 0.07$ and $\Delta n = 0.17$, respectively. It is also observed that the rate of decrease slows down with more added modes, hence it is a slowly converging system.

Note that the order of the addition of new modes in Fig. 3.2 (b) is not by decreasing value of the overlap integral. The modes that are closest in effective index to the unperturbed mode are added to the eigenvalue problem first. Since we expect that finding modes closest to the unperturbed solution is the simplest, we choose this form of convergence. However, it could be possible
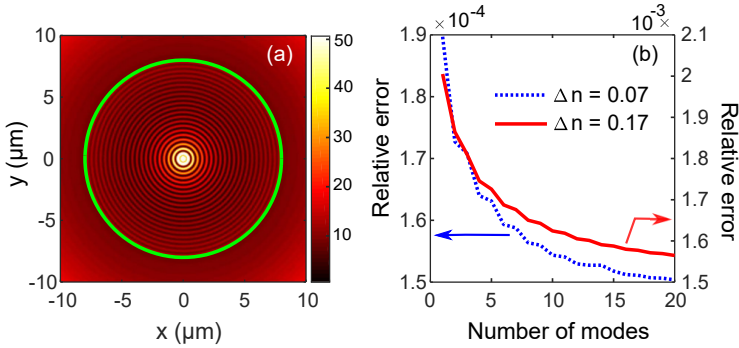
Figure 3.2: (a) Spatial distribution of the time-averaged Poynting vector (in a.u.) of a higher-order core mode supported by a capillary fiber with parameters as used in Fig. 3.1. The fiber core is indicated by the green solid line. The effective index of the unperturbed mode is 0.03139 + 1.0103i. (b) Relative error of the effective index of the higher-order mode with respect to the number of modes used in Eq. (3.8). Two refractive index differences have been considered as perturbations (dashed blue line: $\Delta n = 0.07$, solid red line: $\Delta n = 0.17$).

that the effect of perturbation is such that the modes that are further away in effective index from the considered unperturbed mode might couple better to it in the presence of the perturbation. Hence, the number of basis states should be so chosen that it can describe the perturbed system completely. The relative error for the fundamental core mode is $6.5681e-07$ and $3.3902e-06$ for 154 basis states for a perturbation of $\Delta n = 0.07$ and $\Delta n = 0.17$, respectively.

3.3.2 Silica-air photonic crystal fiber

We now proceed to study diameter disorder in a silica-air photonic crystal fiber. We consider the unperturbed fiber to have four cladding rings of equal radius with $r_0 = 0.25$ μm. The inclusions in the cladding have a refractive index of 1, which corresponds to air. The inclusions are placed in a background medium of index 1.44, corresponding to silica. The inclusions have a triangular lattice [see Fig. 3.3(a)] around the defect core, which comprises of one missing inclusion in the center. The pitch Λ is 2.3 μm, which defines the center-to-center interstrand distance. The poles of the unperturbed system are calculated using the multipole expansion method [45, 46].

We now introduce diameter disorder into the fiber. This is done using the disorder parameter Δ. The radius of each and every inclusion of the fiber is changed within the range of $r_0 - \Delta$ to $r_0 + \Delta$, where $\Delta = 0.1$ μm. The distribution of disorder in the fiber is uniform, with a probability distribution
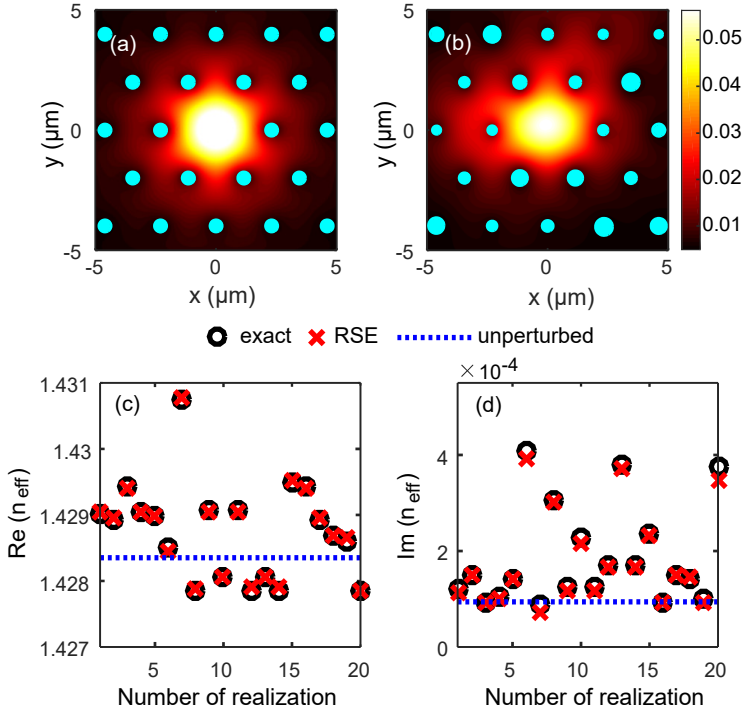
Figure 3.3: Axial component of the time-averaged Poynting vector (in a.u.) of the fundamental core mode of a silica-air photonic crystal fiber with diameter disorder for disorder parameter (a) $\Delta = 0$ μm and (b) $\Delta = 0.1$ μm. The disorder parameter provides the range of radii in the disordered fiber as $r_0 \pm \Delta$, with r_0 being the radius of the air holes in the ordered fiber. The geometrical parameters of the fiber are the same as in Fig. 1(b). Panels (c) and (d) show the comparison of the real and imaginary parts of the effective indices from the resonant state expansion (red crosses) with the exact numerical solution of the perturbed system (black circles) for 20 realizations of disorder at a wavelength of 1.55 μm. The number of modes used for the resonant state expansion is 190. The blue dotted line indicates the effective index for an unperturbed cladding.

of

$$f(r) = \begin{cases} \frac{1}{2\Delta} & \text{for } r_0 - \Delta \leq r \leq r_0 + \Delta \\ 0 & \text{for } r < r_0 - \Delta \text{ or } r > r_0 + \Delta \end{cases} \tag{3.11}$$

The eigenvalue equation for the perturbation is formed with 190 modes, which includes both forward and backward propagating modes. The basis is formed in descending order of the real part of the effective index with the first mode being the fundamental core mode. Since the introduction of the perturbation breaks the symmetry of the fiber, hence coupling of the fundamental mode with modes of other symmetries is possible. Therefore, modes of all symmetries are included in the unperturbed basis [48, 49].

The absolute value of S_z for the fundamental core mode with $n_{\text{eff}} = 1.428 + 9.41e - 05i$ is plotted (in a.u.) for the perfectly ordered fiber in Fig. 3.3 (a) and one realization of diameter disorder with $\Delta = 0.1$ μm in Fig. 3.3 (b) at a wavelength of 1.55 μm. We can see that there is some distortion in the fields due to the disordered cladding. We compare the real and imaginary parts of the effective index between the resonant state expansion and exact numerical solution for different realizations of disorder, which is plotted in Fig. 3.3 (c) and (d), respectively. We see that there is a good agreement between the two methods for the shown realizations. The blue dotted line in (c) and (d) indicates the effective index of the unperturbed system.

Hence, we can now use the perturbation theory to average over many realizations of disorder and study its effects on the guiding properties of the fiber. To do this we range over different values of the disorder parameter Δ and average over 200 realizations of disorder for each Δ. Note that we generate 200 numbers in the range of 0 to 1 and multiply it with the corresponding Δ to create 200 realizations of disorder with disorder strength Δ.

Such a plot for the real and imaginary part of the effective index is shown in Fig. 3.4 (a) and (b), respectively, for the fundamental core mode. The red circles indicate the average perturbed value and the lines indicate the standard deviation, which is calculated as

$$s = \sqrt{\frac{\sum_1^N (x_i - \bar{x})^2}{N - 1}} \tag{3.12}$$

where x_i are the sampling items and $\bar{x}$ is their average. N denotes the number of sampling items. We can see that as we increase the disorder parameter Δ, there is a higher deviation of the average effective index from the unperturbed value (blue dotted line) and the standard deviation grows with increasing Δ. Interestingly, we observe that the average of the real part of effective index seems to show a very linear behavior while the imaginary part has a more quadratic behavior with respect to the disorder parameter. Also note that the
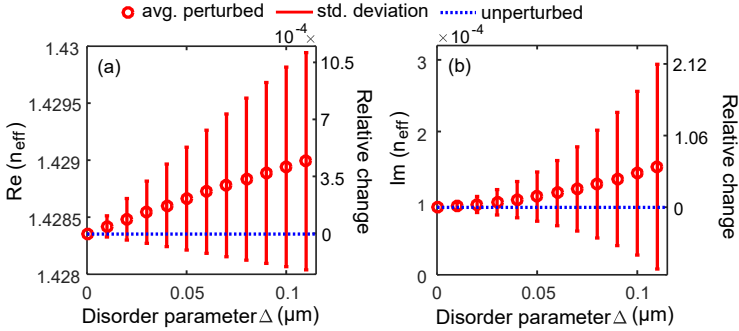
Figure 3.4: Real (a) and imaginary (b) part of the effective index of the fundamental core mode as a function of the disorder parameter Δ averaged over 200 realizations of diameter disorder at a wavelength of 1.55 μm. The averaged real part grows almost linearly with increasing Δ, while the imaginary part is growing quadratically. The standard deviation is indicated by the errorbars. The blue dotted line indicates the effective index of the unperturbed cladding.

number of fiber structures solved to obtain Fig. 3.4 is 2200, which is solved in a matter of seconds using an eigenvalue problem computationally. The relative change in the effective index is plotted as a second y axis in Fig. 3.4 (a) and (b) for the real and imaginary parts of the effective index, respectively.

In conclusion, we have derived a perturbation theory for propagating modes of an optical fiber using the resonant state expansion formalism, which is much faster in treating perturbations such as multiple realizations of disorder than repeatedly solving Maxwell's equations. However, one needs to make sure that the truncated basis used to create the eigenvalue problem of the perturbation theory has enough basis states to fully describe the perturbation.

4 First order perturbation theory: internal and external perturbations

Once upon a midnight dreary, while I pondered, weak and weary, Over many a quaint and curious volume of forgotten lore, While I nodded, nearly napping, suddenly there came a tapping, As of some one gently rapping, rapping at my chamber door. "Tis some visitor," I muttered, "tapping at my chamber door? Only this, and nothing more."

The Raven, Edgar Allan Poe

4.1 Introduction

In the previous chapter, we have dealt with structural and material perturbations in the interior of the fiber. In this chapter, we treat perturbations which occur exclusively in the exterior or throughout, i.e., exterior as well as interior of the fiber, by developing a first order perturbation theory for external perturbations. Perturbation theories that deal with changes in the exterior, for instance, material changes in the homogeneous background, are extremely rare in optics especially for open optical systems. Most perturbation theories as we saw in the previous chapter, deal with internal perturbations [21, 27, 28, 32, 50]. This is because the pole expansion of the Green's dyadic is applicable only in the region of spatial inhomogeneities, as it must have a finite value everywhere except for the poles. This does not hold true for the homogeneous exterior in the case of leaky modes. The first theory for external perturbations of leaky modes was described in Ref. [51] by S. Both et al. In that paper, the resonance shift as a function of homogeneous and isotropic change in refractive index of the background was predicted for two structures: a metallic nanosphere and a periodic array of metal nanoslits. We now adapt this perturbation theory for propagating modes in fiber geometries and treat material changes in the homogeneous background as perturbations of an unperturbed fiber. Additionally, since wavelength is an input parameter in the Maxwell's equations for fibers [see Eq. (2.7)] and not an eigenvalue, we derive the first perturbation theory that treats wavelength as a perturbation which includes bound as well as leaky modes.

Perturbation theories normally involve an integral of quantities such as wavefunction or fields, over the region of perturbation. This so-called overlap integral, was derived for interior perturbations in fiber geometries [see Eq. (3.9)]. When the perturbation lies in the exterior, then the area of integration should ideally be taken as all space, i.e., throughout the homogeneous medium. As we know from different open optical systems, that calculating such an integral does not pose a problem for bound modes which have fields decaying as we move away from the system. However, for leaky modes that have fields growing with distance from the system, such an integral will diverge. This fundamental problem of leaky modes was solved in Ref. [51] by adding an additional surface integral term to the already existing volume integral of previous perturbation theories.

In Fig. 4.1, the schematic of an unperturbed photonic crystal fiber having permittivity ε, permeability μ, and wavenumber k_0 is shown in the top right. A perturbation is then introduced throughout the fiber such that the perturbed system has permittivity ε', permeability μ', and wavenumber k_0', bottom right panel. These perturbations can be introduced individually or simultaneously

into the system. In the first order perturbation theory, these perturbations do not have cross terms, which is not true for higher order perturbation theories that do consist of cross terms. Here we only derive the first order perturbation theory. The dispersion of the fundamental core mode is plotted in Fig. 4.1, for a silica-air photonic crystal fiber. The radius of the fiber inclusions is 0.5 μm and the pitch is 2.3 μm. We see that as we move from ε and μ of the unperturbed system to ε' and μ' of the perturbed system, there is a shift of the dispersion plot with the change in propagation constant indicated by $\Delta\beta$. The change in wavenumber to k_0' from the unperturbed wavenumber of k_0, is also predicted by the perturbation theory as $\Delta\beta_{k_0}$.

Chemical, thermal and biological reactions often lead to a change in the material properties of the medium. Fibers are sensitive to these small changes in the environment and act as sensors for variations in the refractive index [52]. To detect these changes the fields of the fiber need to interact with the changing material. When the perturbation occurs purely in the background of the fiber the sensing method used is called evanescent field sensing [53, 54]. In this method, the cladding modes of photonic crystal fibers that have high field intensities in the exterior, interact with the perturbed background. This effect may be plasmonically enhanced by applying a metal layer in the exterior of the fiber [55]. Fiber optic sensors are also used for temperature and pressure sensing, depending on how the refractive index varies with stress and temperature [56].

Another way of sensing refractive index changes especially in liquids is by placing a hollow core fiber in the liquid background material. This enables the liquid to pass through the fiber core. Hence, the high intensity light trapped within the core interacts with the perturbing background material, which results in increased path lengths and sensitivities [54]. Anti-resonant light cage structures or capillary fibers can be used for such applications as they trap light in a hollow air core [17].

Perturbation theories have proved to be a much faster way for optimizing structures [30, 57–61] where small changes are involved. For the particular case of fiber structures, in addition to adapting the external perturbation theory for material changes, we arrive at a novel perturbation theory that leads to exact values of group velocity by using wavelength (or wavenumber) as a perturbation. Hence, the first order correction term directly gives the tangent to the dispersion curve and we need not solve Maxwell's equations repeatedly for very close wavelengths to obtain a numerical derivative. This perturbation theory is applicable to any fiber structure with bound or leaky modes. Hence, this allows for very quick optimization of the fiber materials and structural parameters to tailor the propagation constant and group velocity to desired values for different applications. We now proceed to derive this first order
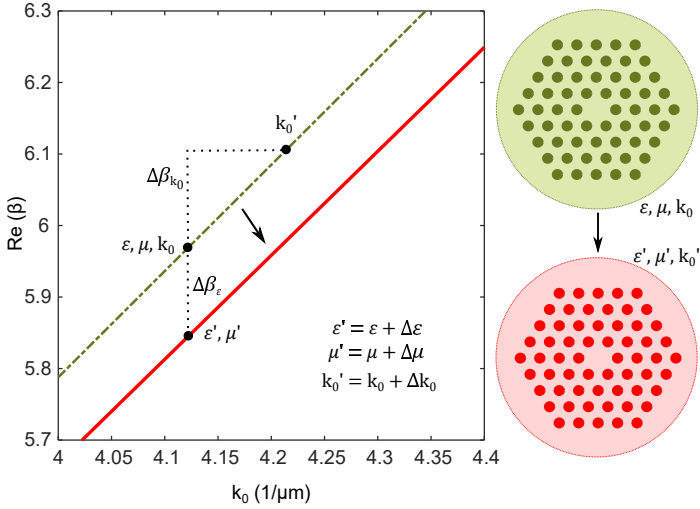
Figure 4.1: The real part of the propagation constant as a function of wavenumber for an unperturbed fiber ε, μ and for an exterior perturbation of ε', μ'. Additionally, the change in wavenumber k_0 can also be treated as a perturbation, with the perturbed wavenumber as k_0'. These perturbations in the first order perturbation theory are treated independent of each other and hence can be applied simultaneously.

perturbation theory for different exterior perturbations.

4.2 Theory

We start out with Fourier transformed Maxwell's equations for the resonant states as described in Eq. (2.7). We then introduce a perturbation in the homogeneous exterior of the fiber. This is defined as

$$\hat{\mathbb{M}} = \hat{\mathbb{M}}_0 + \boldsymbol{\Lambda} \cdot \Delta\hat{\mathbb{M}} = \hat{\mathbb{M}}_0 + \Lambda_{k_0}\Delta\hat{\mathbb{M}}_{k_0} + \Lambda_\varepsilon\Delta\hat{\mathbb{M}}_\varepsilon + \Lambda_\mu\Delta\hat{\mathbb{M}}_\mu, \tag{4.1}$$

where

$$\Delta\hat{\mathbb{M}}_{k_0} = \begin{pmatrix} \Delta k_0\varepsilon & 0 \\ 0 & \Delta k_0\mu \end{pmatrix}, \tag{4.2}$$

$$\Delta\hat{\mathbb{M}}_\varepsilon = \begin{pmatrix} k_0\Delta\varepsilon & 0 \\ 0 & 0 \end{pmatrix}, \tag{4.3}$$

and

$$\Delta\hat{\mathbb{M}}_\mu = \begin{pmatrix} 0 & 0 \\ 0 & k_0\Delta\mu \end{pmatrix}. \tag{4.4}$$

We have introduced the vector $\mathbf{\Lambda}$ with components Λ_ε, Λ_μ and Λ_{k_0} to keep track of each perturbation. We consider the subscript ν for the resonant states of the perturbed system, which also satisfies Eq. (2.7).

As described in the chapters of the normalization and internal perturbation theories, we differentiate between the forward $(+\beta)$ and the reciprocal conjugate, i.e., backward $(-\beta)$ propagating modes [denoted by superscript R]. Multiplying the Max-well's equation for the unperturbed system (denoted by subscript m) with $\hat{\mathbb{F}}_\nu$ and the Maxwell's equation for the perturbed system with $\hat{\mathbb{F}}_m^R$, and subtracting the two equations, we have

$$\hat{\mathbb{F}}_\nu \cdot \hat{\mathbb{M}}_0 \hat{\mathbb{F}}_m^R - \hat{\mathbb{F}}_m^R \cdot (\hat{\mathbb{M}}_0 + \mathbf{\Lambda} \cdot \Delta\hat{\mathbb{M}})\hat{\mathbb{F}}_\nu = 0. \tag{4.5}$$

This is expanded as,

$$\hat{\mathbb{F}}_\nu \cdot \hat{\mathbb{M}}_0 \hat{\mathbb{F}}_m^R - \hat{\mathbb{F}}_m^R \cdot (\hat{\mathbb{M}}_0 + \Lambda_{k_0}\Delta\hat{\mathbb{M}}_{k_0} + \Lambda_\varepsilon\Delta\hat{\mathbb{M}}_\varepsilon + \Lambda_\mu\Delta\hat{\mathbb{M}}_\mu)\hat{\mathbb{F}}_\nu = 0. \tag{4.6}$$

Substituting the matrix forms of $\hat{\mathbb{M}}_0$ and $\hat{\mathbb{F}}$ along with the matrix form of the other perturbation operators and using $\varepsilon = \varepsilon^T$ and $\mu = \mu^T$, we get in matrix-vector notation,

$$\begin{pmatrix} \hat{\mathbb{E}}_\nu \\ i\hat{\mathbb{H}}_\nu \end{pmatrix} \cdot \begin{pmatrix} k_0\varepsilon & -\hat{\nabla}_{-\beta_m}\times \\ -\hat{\nabla}_{-\beta_m}\times & k_0\mu \end{pmatrix}\begin{pmatrix} \hat{\mathbb{E}}_m^R \\ i\hat{\mathbb{H}}_m^R \end{pmatrix}$$
$$-\begin{pmatrix} \hat{\mathbb{E}}_m^R \\ i\hat{\mathbb{H}}_m^R \end{pmatrix} \cdot \begin{pmatrix} k_0\varepsilon + \Lambda_{k_0}\Delta k_0\varepsilon + \Lambda_\varepsilon k_0\Delta\varepsilon & -\hat{\nabla}_{\beta_\nu}\times \\ -\hat{\nabla}_{\beta_\nu}\times & k_0\mu + \Lambda_{k_0}\Delta k_0\mu + \Lambda_\mu k_0\Delta\mu \end{pmatrix}\begin{pmatrix} \hat{\mathbb{E}}_\nu \\ i\hat{\mathbb{H}}_\nu \end{pmatrix} = 0, \tag{4.7}$$

which results in

$$- i\hat{\mathbb{E}}_\nu \cdot \nabla \times \hat{\mathbb{H}}_m^R - i\hat{\mathbb{H}}_\nu \cdot \nabla \times \hat{\mathbb{E}}_m^R - \hat{\mathbb{E}}_m^R \cdot (\Lambda_{k_0}\Delta k_0\varepsilon + \Lambda_\varepsilon k_0\Delta\varepsilon)\hat{\mathbb{E}}_\nu$$
$$+ i\hat{\mathbb{E}}_m^R \cdot \nabla \times \hat{\mathbb{H}}_\nu + i\hat{\mathbb{H}}_m^R \cdot \nabla \times \hat{\mathbb{E}}_\nu + \hat{\mathbb{H}}_m^R \cdot (\Lambda_{k_0}\Delta k_0\mu + \Lambda_\mu k_0\Delta\mu)\hat{\mathbb{H}}_\nu = 0. \tag{4.8}$$

By applying the vector identity of Eq. (2.15) to the Eq. (4.8), we get

$$\nabla_\parallel \cdot (\hat{\mathbb{E}}_\nu \times \hat{\mathbb{H}}_m^R - \hat{\mathbb{E}}_m^R \times \hat{\mathbb{H}}_\nu) + i(\beta_\nu - \beta_m)(\hat{\mathbb{E}}_\nu \times \hat{\mathbb{H}}_m^R - \hat{\mathbb{E}}_m^R \times \hat{\mathbb{H}}_\nu)_z$$
$$+ i\hat{\mathbb{E}}_m^R \cdot (\Lambda_{k_0}\varepsilon\Delta k_0 + \Lambda_\varepsilon k_0\Delta\varepsilon)\hat{\mathbb{E}}_\nu - i\hat{\mathbb{H}}_m^R \cdot (\Lambda_{k_0}\mu\Delta k_0 + \Lambda_\mu k_0\Delta\mu)\hat{\mathbb{H}}_\nu = 0. \tag{4.9}$$

Integrating the above equation over a circular surface of radius R outside the region of spatial inhomogeneities, i.e., the circle encloses all regions of spatial inhomogeneities and using the divergence theorem to convert the sur-

face integral to a line integral, we obtain:

$$
R \int d\phi \, (\hat{E}_{v\phi}\hat{H}^R_{mz} - \hat{E}_{vz}\hat{H}^R_{m\phi} - \hat{E}^R_{m\phi}\hat{H}_{vz} + \hat{E}^R_{mz}\hat{H}_{v\phi})
$$
$$
+ i(\beta_v - \beta_m) \int dA(\hat{E}_{v\rho}\hat{H}^R_{m\phi} - \hat{E}_{v\phi}\hat{H}^R_{m\rho} - \hat{E}^R_{m\rho}\hat{H}_{v\phi} + \hat{E}^R_{m\phi}\hat{H}_{v\rho})
$$
$$
\tag{4.10}
$$
$$
+ i \int dA \, \hat{\mathbf{E}}^R_m \cdot (\Lambda_{k_0}\varepsilon\Delta k_0 + \Lambda_\varepsilon k_0\Delta\varepsilon)\hat{\mathbf{E}}_v
$$
$$
- i \int dA \, \hat{\mathbf{H}}^R_m \cdot (\Lambda_{k_0}\mu\Delta k_0 + \Lambda_\mu k_0\Delta\mu)\hat{\mathbf{H}}_v = 0.
$$

Similar to the Rayleigh-Schroedinger perturbation theory in quantum mechanics [22] and the first order external perturbation theory by S. Both et al. in Ref. [51], we write the propagation constant and fields of the perturbed system as a Taylor series, i.e.,

$$
\beta_v = \beta_m + \mathbf{\Lambda} \cdot \boldsymbol{\beta}^{(1)}_m + O(\mathbf{\Lambda}^2) + ...
$$
$$
= \beta_m + \Lambda_{k_0}\beta^{(1)k_0}_m + \Lambda_\varepsilon\beta^{(1)\varepsilon}_m + \Lambda_\mu\beta^{(1)\mu}_m + ...
$$
$$
\tag{4.11}
$$

and

$$
\hat{\mathbf{F}}_v = \hat{\mathbf{F}}_m + \mathbf{\Lambda} \cdot \hat{\mathbf{F}}^{(1)}_m + O(\mathbf{\Lambda}^2) + ...
$$
$$
= \hat{\mathbf{F}}_m + \Lambda_{k_0}\hat{\mathbf{F}}^{(1)k_0}_m + \Lambda_\varepsilon\hat{\mathbf{F}}^{(1)\varepsilon}_m + \Lambda_\mu\hat{\mathbf{F}}^{(1)\mu}_m + ... ,
$$
$$
\tag{4.12}
$$

which gives

$$
\hat{\mathbf{E}}_v = \hat{\mathbf{E}}_m + \mathbf{\Lambda} \cdot \hat{\mathbf{E}}^{(1)}_m + O(\mathbf{\Lambda}^2) + ...
$$
$$
= \hat{\mathbf{E}}_m + \Lambda_{k_0}\hat{\mathbf{E}}^{(1)k_0}_m + \Lambda_\varepsilon\hat{\mathbf{E}}^{(1)\varepsilon}_m + \Lambda_\mu\hat{\mathbf{E}}^{(1)\mu}_m + ... ,
$$
$$
\tag{4.13}
$$

and

$$
\hat{\mathbf{H}}_v = \hat{\mathbf{H}}_m + \mathbf{\Lambda} \cdot \hat{\mathbf{H}}^{(1)}_m + O(\mathbf{\Lambda}^2) + ...
$$
$$
= \hat{\mathbf{H}}_m + \Lambda_{k_0}\hat{\mathbf{H}}^{(1)k_0}_m + \Lambda_\varepsilon\hat{\mathbf{H}}^{(1)\varepsilon}_m + \Lambda_\mu\hat{\mathbf{H}}^{(1)\mu}_m + ...
$$
$$
\tag{4.14}
$$

Here, $O(\mathbf{\Lambda}^2)$ represents higher orders of $\mathbf{\Lambda}$ terms. $\boldsymbol{\beta}^{(n)}_m$ and $\hat{\mathbf{F}}^{(n)}_m$ are the nth order correction terms to the propagation constant and fields, respectively. Each of the correction terms has a component for ε, μ and k_0 perturbations. Hence, we treat the perturbations independently. Substituting these expansions in Eq. (4.10) and equating the zeroth order terms with respect to Λ_{k_0}, Λ_ε and Λ_μ we obtain,

$$
R \int d\phi(\hat{E}_{m\phi}\hat{H}^R_{mz} - \hat{E}_{mz}\hat{H}^R_{m\phi} - \hat{E}^R_{m\phi}\hat{H}_{mz} + \hat{E}^R_{mz}\hat{H}_{m\phi}) = 0. \tag{4.15}
$$

By converting the reciprocal conjugate modes to forward propagating modes by using the symmetries of the system, as described in Chapter 2, Eq. (4.15) is trivially fulfilled. We now equate the first order terms for Λ_{k_0}, Λ_ε and Λ_μ.

For Λ_{k_0}, we get

$$
\begin{aligned}
&R \int d\phi (\hat{E}_{m\phi}^{(1)k_0} \hat{H}_{mz}^R - \hat{E}_{mz}^{(1)k_0} \hat{H}_{m\phi}^R - \hat{E}_{m\phi}^R \hat{H}_{mz}^{(1)k_0} + \hat{E}_{mz}^R \hat{H}_{m\phi}^{(1)k_0}) \\
&+ i\beta_m^{(1)k_0} \int dA (\hat{E}_{m\rho} \hat{H}_{m\phi}^R - \hat{E}_{m\phi} \hat{H}_{m\rho}^R - \hat{E}_{m\rho}^R \hat{H}_{m\phi} + \hat{E}_{m\phi}^R \hat{H}_{m\rho}) \quad (4.16) \\
&+ i \int dA\ \hat{\mathbb{E}}_m^R \cdot \varepsilon \Delta k_0 \hat{\mathbb{E}}_m - i \int dA\ \hat{\mathbb{H}}_m^R \cdot \mu \Delta k_0 \hat{\mathbb{H}}_m = 0.
\end{aligned}
$$

For Λ_ε, it results in

$$
\begin{aligned}
&R \int d\phi (\hat{E}_{m\phi}^{(1)\varepsilon} \hat{H}_{mz}^R - \hat{E}_{mz}^{(1)\varepsilon} \hat{H}_{m\phi}^R - \hat{E}_{m\phi}^R \hat{H}_{mz}^{(1)\varepsilon} + \hat{E}_{mz}^R \hat{H}_{m\phi}^{(1)\varepsilon}) \\
&+ i\beta_m^{(1)\varepsilon} \int dA (\hat{E}_{m\rho} \hat{H}_{m\phi}^R - \hat{E}_{m\phi} \hat{H}_{m\rho}^R - \hat{E}_{m\rho}^R \hat{H}_{m\phi} + \hat{E}_{m\phi}^R \hat{H}_{m\rho}) \quad (4.17) \\
&+ i \int dA\ \hat{\mathbb{E}}_m^R \cdot k_0 \Delta \varepsilon \hat{\mathbb{E}}_m = 0,
\end{aligned}
$$

while for Λ_μ, we obtain:

$$
\begin{aligned}
&R \int d\phi (\hat{E}_{m\phi}^{(1)\mu} \hat{H}_{mz}^R - \hat{E}_{mz}^{(1)\mu} \hat{H}_{m\phi}^R - \hat{E}_{m\phi}^R \hat{H}_{mz}^{(1)\mu} + \hat{E}_{mz}^R \hat{H}_{m\phi}^{(1)\mu}) \\
&+ i\beta_m^{(1)\mu} \int dA (\hat{E}_{m\rho} \hat{H}_{m\phi}^R - \hat{E}_{m\phi} \hat{H}_{m\rho}^R - \hat{E}_{m\rho}^R \hat{H}_{m\phi} + \hat{E}_{m\phi}^R \hat{H}_{m\rho}) \quad (4.18) \\
&- i \int dA\ \hat{\mathbb{H}}_m^R \cdot k_0 \Delta \mu \hat{\mathbb{H}}_m = 0.
\end{aligned}
$$

The Eqs. (4.16 - 4.18) can be combinedly written as,

$$
\begin{aligned}
&R \int d\phi (\hat{\mathbf{E}}_{m\phi}^{(1)} \hat{H}_{mz}^R - \hat{\mathbf{E}}_{mz}^{(1)} \hat{H}_{m\phi}^R - \hat{E}_{m\phi}^R \hat{\mathbf{H}}_{mz}^{(1)} + \hat{E}_{mz}^R \hat{\mathbf{H}}_{m\phi}^{(1)}) \\
&+ i\boldsymbol{\beta}_m^{(1)} \int dA (\hat{E}_{m\rho} \hat{H}_{m\phi}^R - \hat{E}_{m\phi} \hat{H}_{m\rho}^R - \hat{E}_{m\rho}^R \hat{H}_{m\phi} + \hat{E}_{m\phi}^R \hat{H}_{m\rho}) \quad (4.19) \\
&+ i \int dA\ \hat{\mathbb{F}}_m^R \cdot \Delta \hat{\mathbb{M}} \hat{\mathbb{F}}_m = 0.
\end{aligned}
$$

We now convert the reciprocal conjugate fields to forward propagating

fields, to get for Λ_{k_0}

$$
R \int d\phi (\hat{E}_{m\phi}\hat{H}_{mz}^{(1)k_0} + \hat{E}_{mz}\hat{H}_{m\phi}^{(1)k_0} - \hat{E}_{m\phi}^{(1)k_0}\hat{H}_{mz} - \hat{E}_{mz}^{(1)k_0}\hat{H}_{m\phi})
$$

$$
+ 2i\beta_m^{(1)k_0} \int dA (\hat{E}_{m\rho}\hat{H}_{m\phi} - \hat{E}_{m\phi}\hat{H}_{m\rho}) \tag{4.20}
$$

$$
- i \int dA \,\hat{\mathbb{E}}_m^R \cdot \varepsilon\Delta k_0 \hat{\mathbb{E}}_m + i \int dA \,\hat{\mathbb{H}}_m^R \cdot \mu\Delta k_0 \hat{\mathbb{H}}_m = 0.
$$

For Λ_ε, the first order equation yields

$$
R \int d\phi (\hat{E}_{m\phi}\hat{H}_{mz}^{(1)\varepsilon} + \hat{E}_{mz}\hat{H}_{m\phi}^{(1)\varepsilon} - \hat{E}_{m\phi}^{(1)\varepsilon}\hat{H}_{mz} - \hat{E}_{mz}^{(1)\varepsilon}\hat{H}_{m\phi})
$$

$$
+ 2i\beta_m^{(1)\varepsilon} \int dA (\hat{E}_{m\rho}\hat{H}_{m\phi} - \hat{E}_{m\phi}\hat{H}_{m\rho}) \tag{4.21}
$$

$$
- i \int dA \,\hat{\mathbb{E}}_m^R \cdot k_0\Delta\varepsilon \hat{\mathbb{E}}_m = 0,
$$

and for Λ_μ, we get

$$
R \int d\phi (\hat{E}_{m\phi}\hat{H}_{mz}^{(1)\mu} + \hat{E}_{mz}\hat{H}_{m\phi}^{(1)\mu} - \hat{E}_{m\phi}^{(1)\mu}\hat{H}_{mz} - \hat{E}_{mz}^{(1)\mu}\hat{H}_{m\phi})
$$

$$
+ 2i\beta_m^{(1)\mu} \int dA (\hat{E}_{m\rho}\hat{H}_{m\phi} - \hat{E}_{m\phi}\hat{H}_{m\rho}) \tag{4.22}
$$

$$
+ i \int dA \,\hat{\mathbb{H}}_m^R \cdot k_0\Delta\mu \hat{\mathbb{H}}_m = 0,
$$

which yields the combined equation as,

$$
R \int d\phi (\hat{E}_{m\phi}\hat{\mathbf{H}}_{mz}^{(1)} + \hat{E}_{mz}\hat{\mathbf{H}}_{m\phi}^{(1)} - \hat{\mathbf{E}}_{m\phi}^{(1)}\hat{H}_{mz} - \hat{\mathbf{E}}_{mz}^{(1)}\hat{H}_{m\phi})
$$

$$
+ 2i\boldsymbol{\beta}_m^{(1)} \int dA (\hat{E}_{m\rho}\hat{H}_{m\phi} - \hat{E}_{m\phi}\hat{H}_{m\rho}) \tag{4.23}
$$

$$
- i \int dA \,\hat{\mathbb{F}}_m^R \cdot \Delta\mathbb{M}\hat{\mathbb{F}}_m = 0.
$$

We now have to derive each of the first order field correction terms to obtain the first order correction term for the propagation constant.

4.2.1 ε field correction terms

Let us define $\tilde{\mathbb{F}} = \tilde{\mathbb{F}}(\mathbf{r}_\parallel, \beta, \Lambda)$ with the tilde denoting the analytical continuation of β in the exterior. The perturbed fields are written as a Taylor series

expansion of the unperturbed fields along with first and higher order field correction terms. From Eq. (4.12), we know that,

$$\tilde{\mathbb{F}} = \hat{\mathbb{F}}_m + \Lambda_{k_0}\hat{\mathbb{F}}_m^{(1)k_0} + \Lambda_\varepsilon\hat{\mathbb{F}}_m^{(1)\varepsilon} + \Lambda_\mu\hat{\mathbb{F}}_m^{(1)\mu} + ... \qquad (4.24)$$

By using the above expansion, we get

$$\hat{\mathbb{F}}_{mz}^{(1)\varepsilon} = \frac{d\tilde{\mathbb{F}}_z}{d\Lambda_\varepsilon}\bigg|_{\Lambda=0}. \qquad (4.25)$$

The derivative with respect to Λ_ε is evaluated as,

$$\frac{d\tilde{\mathbb{F}}_z}{d\Lambda_\varepsilon}\bigg|_{\Lambda=0} = \frac{\partial\tilde{\mathbb{F}}}{\partial\Lambda_\varepsilon}\bigg|_{\Lambda=0} + \frac{\partial\tilde{\mathbb{F}}}{\partial\beta}\frac{\partial\beta}{\partial\Lambda_\varepsilon}\bigg|_{\Lambda=0} \qquad (4.26)$$

This results in

$$\hat{E}_{mz}^{(1)\varepsilon} = \frac{d\tilde{E}_z}{d\Lambda_\varepsilon}\bigg|_{\Lambda=0}. \qquad (4.27)$$

From the relations,

$$\varkappa^2 + \beta^2 = (\varepsilon + \Lambda_\varepsilon\Delta\varepsilon)(\mu + \Lambda_\mu\Delta\mu)(k_0 + \Lambda_{k_0}\Delta k_0)^2 \qquad (4.28)$$

and the Taylor expansion of β in Eq. (4.11), we get

$$\frac{\partial\varkappa}{\partial\Lambda_\varepsilon}\bigg|_{\Lambda=0} = \frac{\Delta\varepsilon\mu k_0^2}{2\varkappa_m}, \qquad (4.29)$$

$$\frac{\partial\varkappa}{\partial\beta}\bigg|_{\Lambda=0} = \frac{-\beta_m}{\varkappa_m}. \qquad (4.30)$$

Using Eq. (4.26) along with the relations in Eqs. (2.30) and (2.31), we get the first order field correction term for the z component of the electric field as,

$$\begin{aligned}
E_{mz}^{(1)\varepsilon} &= \left(\frac{\partial\varkappa}{\partial\Lambda_\varepsilon} + \beta_m^{(1)\varepsilon}\frac{\partial\varkappa}{\partial\beta}\right)\frac{\partial E_{mz}}{\partial\varkappa}\bigg|_{\varkappa=\varkappa_m} \\
&= \left(\frac{\Delta\varepsilon\mu k_0^2}{2} - \beta_m\beta_m^{(1)\varepsilon}\right)\frac{1}{\varkappa_m}\frac{\partial E_{mz}}{\partial\varkappa}\bigg|_{\varkappa=\varkappa_m}.
\end{aligned} \qquad (4.31)$$

This can be written as,

$$E_{mz}^{(1)\varepsilon} = \frac{\Gamma_\varepsilon}{2\varkappa_m}\frac{\partial E_{mz}}{\partial\varkappa}\bigg|_{\varkappa=\varkappa_m} \qquad (4.32)$$

where we define

$$\Gamma_\varepsilon = \Delta\varepsilon\mu k_0^2 - 2\beta_m\beta_m^{(1)\varepsilon} \qquad (4.33)$$

for the sake of brevity of notations.

Similarly, the correction term for the z component of the magnetic field is given by

$$\hat{H}_{mz}^{(1)\varepsilon} = \left.\frac{d\tilde{H}_z}{d\Lambda_\varepsilon}\right|_{\Lambda=0}, \tag{4.34}$$

which results in

$$\hat{H}_{mz}^{(1)\varepsilon} = \left.\frac{\Gamma_\varepsilon}{2\varkappa_m}\frac{\partial\hat{H}_{mz}}{\partial\varkappa}\right|_{\varkappa=\varkappa_m}. \tag{4.35}$$

For the ϕ components, we know that

$$\hat{E}_{m\phi}^{(1)\varepsilon} = \left.\frac{d\tilde{E}_\phi}{d\Lambda_\varepsilon}\right|_{\Lambda=0}. \tag{4.36}$$

We describe the ϕ component of the electric field in terms of the z components of the electric and magnetic fields as [47]

$$\hat{E}_\phi = \frac{i\beta}{\varkappa^2\rho}\frac{\partial\hat{E}_z}{\partial\phi} - \frac{i(k_0 + \Lambda_{k_0}\Delta k_0)(\mu + \Lambda_\mu\Delta\mu)}{\varkappa^2}\frac{\partial\hat{H}_z}{\partial\rho}, \tag{4.37}$$

and use the dependence of β and $\varkappa$ on Λ_ε and Eq. (4.26) to get,

$$\begin{aligned}
\hat{E}_{m\phi}^{(1)\varepsilon} = {} & \left.\left(\frac{i\beta_m^{(1)\varepsilon}}{\varkappa_m^2\rho} - \frac{i\beta_m\Gamma_\varepsilon}{\varkappa_m^4\rho}\right)\frac{\partial\hat{E}_{mz}}{\partial\phi} + \frac{i\beta_m\Gamma_\varepsilon}{2\varkappa_m^3\rho}\frac{\partial}{\partial\phi}\left(\frac{\partial\hat{E}_{mz}}{\partial\varkappa}\right)\right|_{\varkappa=\varkappa_m} \\
& + \left.\left(\frac{ik_0\mu\Gamma_\varepsilon}{\varkappa_m^4}\right)\frac{\partial\hat{H}_{mz}}{\partial\rho} - \frac{ik_0\mu\Gamma_\varepsilon}{2\varkappa_m^3}\frac{\partial}{\partial\rho}\left(\frac{\partial\hat{H}_{mz}}{\partial\varkappa}\right)\right|_{\varkappa=\varkappa_m}.
\end{aligned} \tag{4.38}$$

Similarly, we know that

$$\hat{H}_{m\phi}^{(1)\varepsilon} = \left.\frac{d\tilde{H}_\phi}{d\Lambda_\varepsilon}\right|_{\Lambda=0}, \tag{4.39}$$

where [47]

$$\hat{H}_\phi = \frac{i\beta}{\varkappa^2\rho}\frac{\partial\hat{H}_z}{\partial\phi} + \frac{i(k_0 + \Lambda_{k_0}\Delta k_0)(\varepsilon + \Lambda_\varepsilon\Delta\varepsilon)}{\varkappa^2}\frac{\partial\hat{E}_z}{\partial\rho}, \tag{4.40}$$

we again use the dependence of β and $\varkappa$ on Λ_ε along with Eq. (4.26) to get,

$$\begin{aligned}
\hat{H}_{m\phi}^{(1)\varepsilon} = {} & \left.\left(\frac{i\beta_m^{(1)\varepsilon}}{\varkappa_m^2\rho} - \frac{i\beta_m\Gamma_\varepsilon}{\varkappa_m^4\rho}\right)\frac{\partial\hat{H}_{mz}}{\partial\phi} + \frac{i\beta_m\Gamma_\varepsilon}{2\varkappa_m^3\rho}\frac{\partial}{\partial\phi}\left(\frac{\partial\hat{H}_{mz}}{\partial\varkappa}\right)\right|_{\varkappa=\varkappa_m} \\
& + \left.\left(\frac{ik_0\Delta\varepsilon}{\varkappa_m^2} - \frac{ik_0\varepsilon\Gamma_\varepsilon}{\varkappa_m^4}\right)\frac{\partial\hat{E}_{mz}}{\partial\rho} + \frac{ik_0\varepsilon\Gamma_\varepsilon}{2\varkappa_m^3}\frac{\partial}{\partial\rho}\left(\frac{\partial\hat{E}_{mz}}{\partial\varkappa}\right)\right|_{\varkappa=\varkappa_m}.
\end{aligned} \tag{4.41}$$

Substituting the expressions for the correction terms in Eq. (4.21) and collecting all the $\beta_m^{(1)\varepsilon}$ terms we get

$$\beta_m^{(1)\varepsilon} = \frac{S_1^\varepsilon + L_1^\varepsilon}{S_0 + L_0}, \tag{4.42}$$

where

$$S_1^\varepsilon = ik_0 \int dA \, \hat{\mathbb{E}}_m^R \cdot \Delta\varepsilon \hat{\mathbb{E}}_m, \tag{4.43}$$

$$S_0 = 2i \int dA \, (\hat{E}_{m\rho}\hat{H}_{m\phi} - \hat{E}_{m\phi}\hat{H}_{m\rho}), \tag{4.44}$$

$$
\begin{aligned}
L_0 = 2i\left(\frac{\varepsilon\mu k_0^2 + \beta_m^2}{2\varkappa_m^4}\right) \int d\phi \left(\hat{E}_{mz}\frac{\partial \hat{H}_{mz}}{\partial\phi} - \hat{H}_{mz}\frac{\partial \hat{E}_{mz}}{\partial\phi}\right)_{\rho=R} \\
+ 2i\left(\frac{k_0\beta R^2}{2\varkappa_m^4}\right) \int d\phi\Big\{ \varepsilon\Big[\Big(\frac{\partial \hat{E}_{mz}}{\partial\rho}\Big)^2 - \rho\hat{E}_{mz}\frac{\partial}{\partial\rho}\Big(\frac{1}{\rho}\frac{\partial \hat{E}_{mz}}{\partial\rho}\Big)\Big] \\
+ \mu\Big[\Big(\frac{\partial \hat{H}_{mz}}{\partial\rho}\Big)^2 - \rho\hat{H}_{mz}\frac{\partial}{\partial\rho}\Big(\frac{1}{\rho}\frac{\partial \hat{H}_{mz}}{\partial\rho}\Big)\Big]\Big\}_{\rho=R},
\end{aligned}
\tag{4.45}
$$

and

$$L_1^\varepsilon = \frac{\Delta\varepsilon}{\varepsilon}\tilde{L}_1^\varepsilon, \tag{4.46}$$

where

$$
\begin{aligned}
\tilde{L}_1^\varepsilon = \frac{i\beta_m\varepsilon\mu k_0^2}{\varkappa_m^4} \int d\phi \left(\hat{E}_{mz}\frac{\partial \hat{H}_{mz}}{\partial\phi} - \hat{H}_{mz}\frac{\partial \hat{E}_{mz}}{\partial\phi}\right)_{\rho=R} \\
+ \frac{ik_0^3 R^2 \varepsilon\mu}{2\varkappa_m^4} \int d\phi \Big\{ \varepsilon\Big[\Big(\frac{\partial \hat{E}_{mz}}{\partial\rho}\Big)^2 - \rho\hat{E}_{mz}\frac{\partial}{\partial\rho}\Big(\frac{1}{\rho}\frac{\partial \hat{E}_{mz}}{\partial\rho}\Big)\Big] \\
+ \mu\Big[\Big(\frac{\partial \hat{H}_{mz}}{\partial\rho}\Big)^2 - \rho\hat{H}_{mz}\frac{\partial}{\partial\rho}\Big(\frac{1}{\rho}\frac{\partial \hat{H}_{mz}}{\partial\rho}\Big)\Big]\Big\}_{\rho=R} \\
- \frac{iRk_0\varepsilon}{\varkappa_m^2} \int d\phi \left(\hat{E}_{mz}\frac{\partial \hat{E}_{mz}}{\partial\rho}\right)_{\rho=R}.
\end{aligned}
\tag{4.47}
$$

We have converted the $\varkappa$ derivatives to ρ derivatives by using the relations described in Eqs. (2.32-2.33).

Note that similar to the derivation of correction terms for an ε perturbation, in further derivations the surface integral is always denoted by S and taken over a circle of radius R outside the region of spatial inhomogeneities. The line integral denoted by L encloses the surface integral and is calculated for the same radius R.

In Eq. (4.42), we have arrived at the expression for the first order correction term of the propagation constant for a purely ε perturbation. The fields in this expression need not be normalized separately since the normalization expression of $S_0 + L_0$ is automatically derived as a by product of the first order
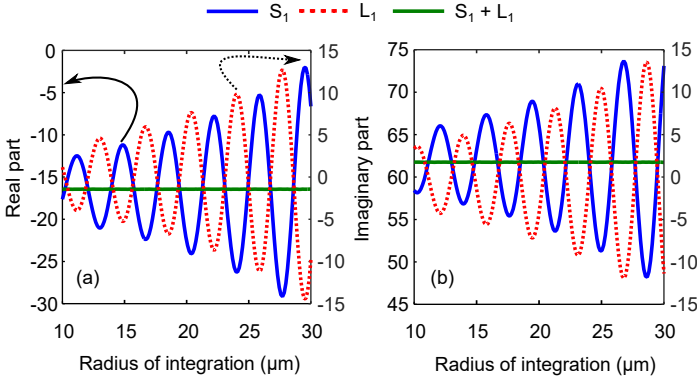
Figure 4.2: Real (a) and imaginary (b) part of the surface and line integral for an ε perturbation of unity, i.e., $\Delta\varepsilon = 1$, as a function of the radius of integration for a higher order mode for a silica-air photonic crystal fiber at a wavelength of 1 μm. The air inclusions have a radius of 0.25 μm with a pitch of 2.3 μm. It is seen that, since the modes supported by this fiber are leaky, the real and imaginary parts of the surface and line integrals are growing as the radius of normalization is increased. The surface integral is shown in the left *y* axis while the line integral is shown in the right *y* axis, as indicated by the arrows in panel (a). The sum of the surface and line integrals (green solid line) is constant independent of the radius of integration, despite the leaky nature of the mode.

derivation with an additional factor of $2i$ as can be seen from the normalization expression in Eq. (2.35).

Also note that the expression for the surface integral S_1^ε is the same as the so-called overlap integral derived for ε perturbations in the interior, but to the single mode approximation, where the perturbed field is taken equal to the unperturbed field. The additional expression is the line integral term which is specific to exterior perturbations. In Eq. (4.42), if the perturbation is purely in the interior then the line term would go to zero. Hence, this perturbation theory is also consistent with the interior perturbation theory to the single mode approximation.

We plot in Fig. 4.2, the real (a) and imaginary (b) parts of the surface and line integral of Eq. (4.42), denoted by the blue solid line and red dashed line respectively, as a function of radius of integration outside the region of spatial inhomogeneities for a higher order mode of a silica-air photonic crystal fiber for a unity perturbation in ε. The photonic crystal fiber comprises of four cladding rings with one missing inclusion as the defect core. The radius of the inclusion is 0.25 μm and the pitch is 2.3 μm. The wavelength is 1 μm. The green solid line denotes the sum of the surface and line integral terms. The

left y axis corresponds to the solid lines while the right y axis corresponds to the dashed line, as indicated by the arrow. We see that individually, both the real and imaginary parts of the surface and line terms oscillate and grow with respect to the radius of integration. This is due to the leaky nature of the mode, which has fields growing in the exterior. From Fig. 4.2, we see that the oscillations of the surface and line terms are perfectly out of phase with each other and the growth of the line term perfectly counteracts the growth of the surface term. This results in their sum giving a constant value irrespective of the radius of integration. Additionally, this helps in choosing a minimum computational domain in the presence of the perturbation which is very advantageous for fast calculations.

4.2.2 k_0 field correction terms

We now derive the field correction terms for the k_0 perturbation. We proceed as in the previous derivation where we use Eq. (4.24) to write,

$$\hat{\mathbb{F}}_{mz}^{(1)k_0} = \left.\frac{d\tilde{\mathbb{F}}_z}{d\Lambda_{k_0}}\right|_{\boldsymbol{\Lambda}=0}. \tag{4.48}$$

The derivative with respect to Λ_{k_0} is evaluated as,

$$\left.\frac{d\tilde{\mathbb{F}}_z}{d\Lambda_{k_0}}\right|_{\boldsymbol{\Lambda}=0} = \left.\frac{\partial\tilde{\mathbb{F}}}{\partial\Lambda_{k_0}}\right|_{\boldsymbol{\Lambda}=0} + \frac{\partial\tilde{\mathbb{F}}}{\partial\beta}\left.\frac{\partial\beta}{\partial\Lambda_{k_0}}\right|_{\boldsymbol{\Lambda}=0} \tag{4.49}$$

From the above equations, we get

$$\hat{E}_{mz}^{(1)k_0} = \left.\frac{d\tilde{E}_z}{d\Lambda_{k_0}}\right|_{\boldsymbol{\Lambda}=0}, \tag{4.50}$$

Using the relations in Eqs. (4.28) and (4.11), we have

$$\left.\frac{\partial\varkappa}{\partial\Lambda_{k_0}}\right|_{\boldsymbol{\Lambda}=0} = \frac{\varepsilon\mu k_0\Delta k_0}{\varkappa_m}, \tag{4.51}$$

Using Eq. (4.49) and Eq. (4.30) along with Eqs. (2.30) and (2.31), we get the first order field correction term for the z component of the electric field as,

$$\begin{aligned}
E_{mz}^{(1)k_0} &= \left(\frac{\partial\varkappa}{\partial\Lambda_{k_0}} + \beta_m^{(1)k_0}\frac{\partial\varkappa}{\partial\beta}\right)\left.\frac{\partial E_{mz}}{\partial\varkappa}\right|_{\varkappa=\varkappa_m} \\
&= \left(\frac{\varepsilon\mu k_0\Delta k_0}{\varkappa_m} - \frac{\beta_m\beta_m^{(1)k_0}}{\varkappa_m}\right)\left.\frac{\partial E_{mz}}{\partial\varkappa}\right|_{\varkappa=\varkappa_m}.
\end{aligned} \tag{4.52}$$

Defining

$$\Gamma_{k_0} = \varepsilon\mu k_0\Delta k_0 - \beta_m\beta_m^{(1)k_0}, \tag{4.53}$$

we can write the correction term for the z component of the electric field as,

$$\hat{E}_{mz}^{(1)k_0} = \frac{\Gamma_{k_0}}{\varkappa_m} \frac{\partial \hat{E}_{mz}}{\partial \varkappa}\bigg|_{\varkappa=\varkappa_m}. \tag{4.54}$$

Similarly,

$$\hat{H}_{mz}^{(1)k_0} = \frac{d\tilde{H}_z}{d\Lambda_{k_0}}\bigg|_{\Lambda=0}, \tag{4.55}$$

which gives

$$\hat{H}_{mz}^{(1)k_0} = \frac{\Gamma_{k_0}}{\varkappa_m} \frac{\partial \hat{H}_{mz}}{\partial \varkappa}\bigg|_{\varkappa=\varkappa_m}. \tag{4.56}$$

For

$$\hat{E}_{m\phi}^{(1)k_0} = \frac{d\tilde{E}_\phi}{d\Lambda_{k_0}}\bigg|_{\Lambda=0}, \tag{4.57}$$

with $\hat{E}_\phi$ as defined in Eq. (4.37), we use Eq. (4.49) along with the dependence of β and $\varkappa$ on Λ_{k_0} to get,

$$\hat{E}_{m\phi}^{(1)k_0} = \left(\frac{i\beta_m^{(1)k_0}}{\varkappa_m^2\rho} - \frac{2i\beta_m\Gamma_{k_0}}{\varkappa_m^4\rho}\right)\frac{\partial \hat{E}_{mz}}{\partial\phi} + \frac{i\beta_m\Gamma_{k_0}}{\varkappa_m^3\rho}\frac{\partial}{\partial\phi}\left(\frac{\partial \hat{E}_{mz}}{\partial\varkappa}\right)\bigg|_{\varkappa=\varkappa_m}$$
$$- \left(\frac{i\mu\Delta k_0}{\varkappa_m^2} - \frac{2i\mu k_0\Gamma_{k_0}}{\varkappa_m^4}\right)\frac{\partial \hat{H}_{mz}}{\partial\rho} - \frac{ik_0\mu\Gamma_{k_0}}{\varkappa_m^3}\frac{\partial}{\partial\rho}\left(\frac{\partial \hat{H}_{mz}}{\partial\varkappa}\right)\bigg|_{\varkappa=\varkappa_m}. \tag{4.58}$$

For

$$\hat{H}_{m\phi}^{(1)k_0} = \frac{d\tilde{H}_\phi}{d\Lambda_{k_0}}\bigg|_{\Lambda=0}, \tag{4.59}$$

we use the expression of $\hat{H}_{phi}$ as defined in Eq. (4.40) along with Eq. (4.49) to get the correction term as

$$\hat{H}_{m\phi}^{(1)k_0} = \left(\frac{i\beta_m^{(1)k_0}}{\varkappa_m^2\rho} - \frac{2i\beta_m\Gamma_{k_0}}{\varkappa_m^4\rho}\right)\frac{\partial \hat{H}_{mz}}{\partial\phi} + \frac{i\beta_m\Gamma_{k_0}}{\varkappa_m^3\rho}\frac{\partial}{\partial\phi}\left(\frac{\partial \hat{H}_{mz}}{\partial\varkappa}\right)\bigg|_{\varkappa=\varkappa_m}$$
$$+ \left(\frac{i\varepsilon\Delta k_0}{\varkappa_m^2} - \frac{2i\varepsilon k_0\Gamma_{k_0}}{\varkappa_m^4}\right)\frac{\partial \hat{E}_{mz}}{\partial\rho} + \frac{ik_0\varepsilon\Gamma_{k_0}}{\varkappa_m^3}\frac{\partial}{\partial\rho}\left(\frac{\partial \hat{E}_{mz}}{\partial\varkappa}\right)\bigg|_{\varkappa=\varkappa_m}. \tag{4.60}$$

Substituting the correction terms in Eq. (4.20) and combining all the $\beta_m^{(1)k_0}$ terms we get

$$\beta_m^{(1)k_0} = \frac{S_1^{k_0} + L_1^{k_0}}{S_0 + L_0}, \tag{4.61}$$

where S_0 and L_0 are the same as defined in Eq. (4.44) and Eq. (4.45) respectively, and the expressions for $S_1^{k_0}$ and $L_1^{k_0}$ are

$$S_1^{k_0} = i\Delta k_0 \int dA \; \hat{\mathbb{E}}_m^R \cdot \varepsilon\hat{\mathbb{E}}_m - \hat{\mathbb{H}}_m^R \cdot \mu\hat{\mathbb{H}}_m, \tag{4.62}$$

and

$$L_1^{k_0} = \frac{\Delta k_0}{k_0} \tilde{L}_1^{k_0} \tag{4.63}$$

where

$$
\begin{aligned}
\tilde{L}_1^{k_0} =& \frac{2i\beta_m \varepsilon \mu k_0^2}{\varkappa_m^4} \int d\phi \left(\hat{E}_{mz} \frac{\partial \hat{H}_{mz}}{\partial \phi} - \hat{H}_{mz} \frac{\partial \hat{E}_{mz}}{\partial \phi} \right)_{\rho=R} \\
&+ \frac{ik_0^3 R^2 \varepsilon \mu}{\varkappa_m^4} \int d\phi \left\{ \varepsilon \left[\left(\frac{\partial \hat{E}_{mz}}{\partial \rho} \right)^2 - \rho \hat{E}_{mz} \frac{\partial}{\partial \rho} \left(\frac{1}{\rho} \frac{\partial \hat{E}_{mz}}{\partial \rho} \right) \right] \right. \\
&\qquad\qquad\qquad \left. + \mu \left[\left(\frac{\partial \hat{H}_{mz}}{\partial \rho} \right)^2 - \rho \hat{H}_{mz} \frac{\partial}{\partial \rho} \left(\frac{1}{\rho} \frac{\partial \hat{H}_{mz}}{\partial \rho} \right) \right] \right\}_{\rho=R} \\
&- \frac{iRk_0}{\varkappa_m^2} \int d\phi \left(\varepsilon \hat{E}_{mz} \frac{\partial \hat{E}_{mz}}{\partial \rho} + \mu \hat{H}_{mz} \frac{\partial \hat{H}_{mz}}{\partial \rho} \right)_{\rho=R}.
\end{aligned}
\tag{4.64}
$$

By applying the relations in Eqs. (2.32-2.33) we have converted the derivatives with respect to $\varkappa$ to spatial derivatives.
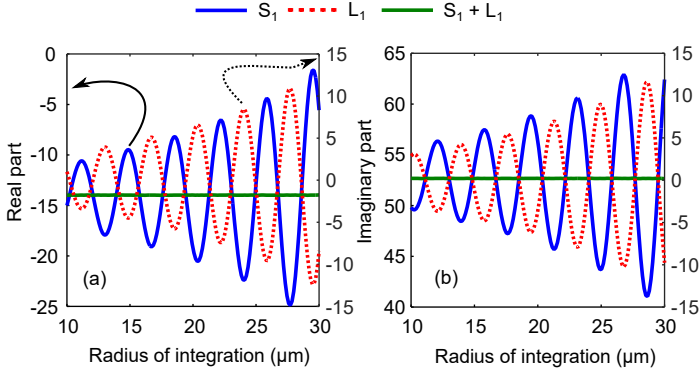

Figure 4.3: Real (a) and imaginary (b) part of the surface and line integral for a unity k_0 perturbation, i.e., $\Delta k_0 = 1$, as a function of the radius of integration for a higher order mode of a silica-air photonic crystal fiber. The fiber parameters are the same as in Fig. 4.2. We observe that due to the leaky nature of the mode we have growing fields and hence a growing surface integral with respect to the radius of integration. However, the line integral countervails this growth to give a constant value for the perturbed propagation constant. Note that the scales on the right and left y axes, which denote the line and surface integrals respectively, are different.

In Fig. 4.3, we plot the equivalent of Fig. 4.2 for a unity k_0 perturbation. The example structure of a silica-air photonic crystal fiber along with the fiber parameters remains the same. We again note that the leaky nature of the mode

results in growing surface and line integrals as a function of the radius of normalization but the sum of the surface and line integrals, taken over a circle enclosing all regions of spatial inhomogeneities results in a constant value for the correction term. Hence, this results in the first perturbation theory for wavelength.

Note that since a change in wavelength occurs over the entire structure, i.e., in the interior as well as the exterior, the line integral is very critical in the case of wavelength perturbation to get the first order correction term. This perturbation theory is valid for both bound and leaky modes. For the case of bound modes, the line integral may go to zero if the radius of integration is taken large enough as bound modes have exponentially decaying fields. However, calculating the line integral even for bound modes helps to reduce the computational domain, which significantly reduces simulation time.

4.2.3 μ field correction terms

We now derive the field correction terms for the μ component of the perturbation. From Eq. (4.24), we can write

$$\hat{\mathbb{F}}_{mz}^{(1)\mu} = \frac{d\tilde{\mathbb{F}}_z}{d\Lambda_\mu}\bigg|_{\Lambda=0}. \tag{4.65}$$

The derivative with respect to Λ_μ is evaluated as,

$$\frac{d\tilde{\mathbb{F}}_z}{d\Lambda_\mu}\bigg|_{\Lambda=0} = \frac{\partial\tilde{\mathbb{F}}}{\partial\Lambda_\mu}\bigg|_{\Lambda=0} + \frac{\partial\tilde{\mathbb{F}}}{\partial\beta}\frac{\partial\beta}{\partial\Lambda_\mu}\bigg|_{\Lambda=0}. \tag{4.66}$$

Hence, we get

$$\hat{E}_{mz}^{(1)\mu} = \frac{d\tilde{E}_z}{d\Lambda_\mu}\bigg|_{\Lambda=0}, \tag{4.67}$$

Using the relations in Eqs. (4.28) and (4.11), we have

$$\frac{\partial\varkappa}{\partial\Lambda_\mu}\bigg|_{\Lambda=0} = \frac{\varepsilon\Delta\mu k_0^2}{2\varkappa_m}. \tag{4.68}$$

Applying Eq. (4.66) and Eq. (4.30) along with Eqs. (2.30) and (2.31), we get the first order field correction term for the z component of the electric field as,

$$\begin{aligned}
E_{mz}^{(1)\mu} &= \left(\frac{\partial\varkappa}{\partial\Lambda_{k_0}} + \beta_m^{(1)\mu}\frac{\partial\varkappa}{\partial\beta}\right)\frac{\partial E_{mz}}{\partial\varkappa}\bigg|_{\varkappa=\varkappa_m} \\
&= \left(\frac{\varepsilon\Delta\mu k_0^2}{2} - \beta_m\beta_m^{(1)\mu}\right)\frac{1}{\varkappa_m}\frac{\partial E_{mz}}{\partial\varkappa}\bigg|_{\varkappa=\varkappa_m}.
\end{aligned} \tag{4.69}$$

Defining

$$\Gamma_\mu = \varepsilon\Delta\mu k_0^2 - 2\beta_m\beta_m^{(1)\mu} \tag{4.70}$$

we can write the first order correction terms as

$$\hat{E}_{mz}^{(1)\mu} = \frac{\Gamma_\mu}{2\varkappa_m}\frac{\partial\hat{E}_{mz}}{\partial\varkappa}\bigg|_{\varkappa=\varkappa_m}. \tag{4.71}$$

Similarly,

$$\hat{H}_{mz}^{(1)\mu} = \frac{d\tilde{H}_z}{d\Lambda_\mu}\bigg|_{\Lambda=0}. \tag{4.72}$$

Hence, we obtain

$$\hat{H}_{mz}^{(1)\mu} = \frac{\Gamma_\mu}{2\varkappa_m}\frac{\partial\hat{H}_{mz}}{\partial\varkappa}\bigg|_{\varkappa=\varkappa_m}. \tag{4.73}$$

We know that

$$\hat{E}_{m\phi}^{(1)\mu} = \frac{d\tilde{E}_\phi}{d\Lambda_\mu}\bigg|_{\Lambda=0}. \tag{4.74}$$

Using the relations from Eqs. (4.37) and (4.66), we get

$$\begin{aligned}
\hat{E}_{m\phi}^{(1)\mu} = & \left(\frac{i\beta_m^{(1)\mu}}{\varkappa_m^2\rho} - \frac{i\beta_m\Gamma_\mu}{\varkappa_m^4\rho}\right)\frac{\partial\hat{E}_{mz}}{\partial\phi} + \frac{i\beta_m\Gamma_\mu}{2\varkappa_m^3\rho}\frac{\partial}{\partial\phi}\left(\frac{\partial E_{mz}}{\partial\varkappa}\right)\bigg|_{\varkappa=\varkappa_m} \\
& - \left(\frac{ik_0\Delta\mu}{\varkappa_m^2} - \frac{i\mu k_0\Gamma_\mu}{\varkappa_m^4}\right)\frac{\partial\hat{H}_{mz}}{\partial\rho} - \frac{ik_0\mu\Gamma_\mu}{2\varkappa_m^3}\frac{\partial}{\partial\rho}\left(\frac{\partial\hat{H}_{mz}}{\partial\varkappa}\right)\bigg|_{\varkappa=\varkappa_m}.
\end{aligned} \tag{4.75}$$

Finally,

$$\hat{H}_{m\phi}^{(1)\mu} = \frac{d\tilde{H}_\phi}{d\Lambda_\mu}\bigg|_{\Lambda=0}. \tag{4.76}$$

Using the relations from Eqs. (4.40) and (4.66), we obtain

$$\begin{aligned}
\hat{H}_{m\phi}^{(1)\mu} = & \left(\frac{i\beta_m^{(1)\mu}}{\varkappa_m^2\rho} - \frac{i\beta_m\Gamma_\mu}{\varkappa_m^4\rho}\right)\frac{\partial\hat{H}_{mz}}{\partial\phi} + \frac{i\beta_m\Gamma_\mu}{2\varkappa_m^3\rho}\frac{\partial}{\partial\phi}\left(\frac{\partial\hat{H}_{mz}}{\partial\varkappa}\right)\bigg|_{\varkappa=\varkappa_m} \\
& - \frac{i\varepsilon k_0\Gamma_\mu}{\varkappa_m^4}\frac{\partial\hat{E}_{mz}}{\partial\rho} + \frac{ik_0\varepsilon\Gamma_\mu}{2\varkappa_m^3}\frac{\partial}{\partial\rho}\left(\frac{\partial\hat{E}_{mz}}{\partial\varkappa}\right)\bigg|_{\varkappa=\varkappa_m}.
\end{aligned} \tag{4.77}$$

Substituting the correction terms in Eq. (4.23) and combining all the $\beta_m^{(1)\mu}$ terms we get

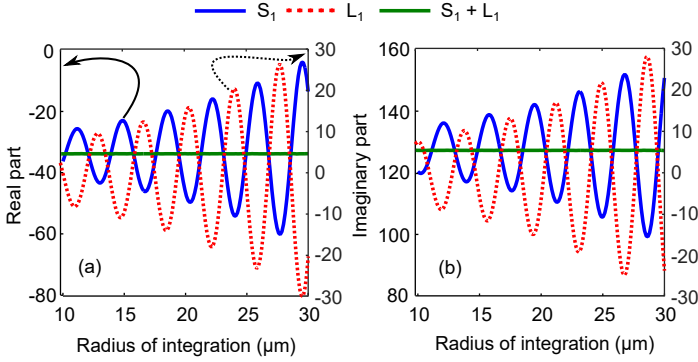$$\beta_m^{(1)\mu} = \frac{S_1^\mu + L_1^\mu}{S_0 + L_0}, \tag{4.78}$$

Figure 4.4: Real (a) and imaginary (b) part of the surface and line integral for a μ perturbation of unity, i.e., $\Delta\mu = 1$, as a function of the radius of integration for a higher order mode of a silica-air photonic crystal fiber. The fiber parameters are the same as in Fig. 4.2. We see that similar to the ε and k_0 perturbations, the sum of the surface and line term is constant with respect to radius of normalization for the μ perturbation as well. Note that the scales in the left and right y axis denoting surface and line terms respectively, are different.

where S_0 and L_0 are the same as defined in Eq. (4.44) and Eq. (4.45) respectively, and the expressions for S_1^μ and L_1^μ are

$$S_1^\mu = -ik_0 \int dA\ \hat{\mathbb{H}}_m^R \cdot \Delta\mu \hat{\mathbb{H}}_m, \tag{4.79}$$

$$L_1^\mu = \frac{\Delta\mu}{\mu} \tilde{L}_1^\mu, \tag{4.80}$$

where

$$
\begin{aligned}
\tilde{L}_1^\mu =& \frac{i\beta_m \varepsilon \mu k_0^2}{\varkappa_m^4} \int d\phi \left(\hat{E}_{mz} \frac{\partial \hat{H}_{mz}}{\partial\phi} - \hat{H}_{mz} \frac{\partial \hat{E}_{mz}}{\partial\phi} \right)_{\rho=R} \\
&+ \frac{ik_0^3 R^2 \varepsilon\mu}{2\varkappa_m^4} \int d\phi \left\{ \varepsilon\left[\left(\frac{\partial \hat{E}_{mz}}{\partial\rho}\right)^2 - \rho\hat{E}_{mz}\frac{\partial}{\partial\rho}\left(\frac{1}{\rho}\frac{\partial\hat{E}_{mz}}{\partial\rho}\right) \right] \right. \\
&\left. \qquad\qquad + \mu\left[\left(\frac{\partial \hat{H}_{mz}}{\partial\rho}\right)^2 - \rho\hat{H}_{mz}\frac{\partial}{\partial\rho}\left(\frac{1}{\rho}\frac{\partial\hat{H}_{mz}}{\partial\rho}\right) \right] \right\}_{\rho=R} \\
&- \frac{iRk_0\mu}{\varkappa_m^2} \int d\phi \left(\hat{H}_{mz}\frac{\partial\hat{H}_{mz}}{\partial\rho} \right)_{\rho=R},
\end{aligned}
\tag{4.81}
$$

after converting the $\varkappa$ derivatives to spatial ones using Eqs. (2.32-2.33).

We can now write the combined equation for the first order correction term of the propagtion constant by using the expressions of Eqs. (4.42), (4.61) and (4.78), to get

$$\beta_m^{(1)} = \frac{\int dA \ \hat{\mathbb{F}}_m^R \cdot \Delta\hat{\mathbb{M}}\hat{\mathbb{F}}_m + \frac{\Delta\varepsilon}{\varepsilon}\tilde{L}_1^\varepsilon + \frac{\Delta\mu}{\mu}\tilde{L}_1^\mu + \frac{\Delta k_0}{k_0}\tilde{L}_1^{k_0}}{S_0 + L_0} \qquad (4.82)$$

Interestingly, the symmetry of the equations works out such that,

$$\tilde{L}_1^{k_0} = \tilde{L}_1^\varepsilon + \tilde{L}_1^\mu \qquad (4.83)$$

In Fig. 4.4, we plot the real and imaginary part of the surface and line integrals of Eq. (4.78) as a function of the radius of integration for a unity μ perturbation throughout the example structure. We show that the expression for the propagation constant is independent of the radius of normalization for the same higher order core mode of a silica-air photonic crystal fiber as in Figs. 4.2 and 4.3. This relation for the correction term holds true for both bound and leaky modes. Note that we have derived the expression of the first order correction term of the propagation constant for the μ perturbation purely for the sake of completeness. However, it is hard to find practical examples where small changes in permeability occur in the external media at optical frequencies. In the following section, we now apply our first order perturbation theory to example fiber structures for ε and k_0 perturbations in the interior as well as exterior.

4.3 Examples

4.3.1 ε perturbation

We now show three different examples of fiber structures with ε perturbations in the exterior as well as interior. We consider only a scalar, homogeneous and isotropic perturbation of the permittivity.

Full perturbation in a step-index fiber

We first consider a simple theoretical example of a step-index fiber with a core index of $n = 1.10$ (theoretical assumption) and a homogeneous background index of $n_{bg} = 1.45$. The radius of the fiber core is 5 μm. The schematic of the unperturbed fiber is shown in Fig. 4.5 (a). We now introduce a perturbation of Δn both in the fiber core and exterior homogeneous background while all other parameters remain the same. The schematic of this perturbed fiber is shown in Fig. 4.5 (b). The panels (a) and (b) of the Fig. 4.5 compare

the real and imaginary parts of the effective index calculated from the first order perturbation theory with the exact analytical solutions, respectively, as a function of change in refractive index Δn. The wavelength is 1 µm.

We see that for the considered fundamental core mode, there is a very good agreement between the first order perturbation theory and exact analytical solution for both the real and imaginary parts for a range of positive as well as negative changes in the refractive index. However, for large changes the first order theory deviates from the exact solutions as the behavior of the effective index becomes more and more non linear.

This example perturbation can be used to treat materials that change their refractive index with temperature resulting in an overall change of index [62]. It should be noted however that the core and cladding will not have the same Δn as they are made up of different materials. Nonetheless, we consider a constant change keeping in mind that the theory can easily be extended to materials that have different temperature coefficients for refractive index in the core and cladding.
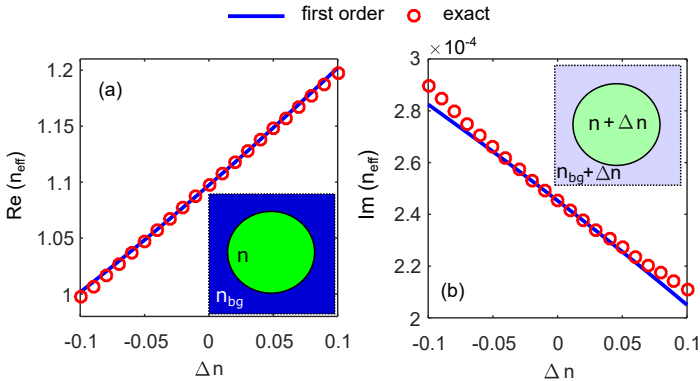

Figure 4.5: Comparison of the real (a) and imaginary (b) part of the effective index as a function of change in refractive index in the interior as well as exterior, between exact solution and first order perturbation theory for the fundamental core mode of a step-index fiber. The schematic of the unperturbed fiber, shown in the inset of (a) where $n = 1.10$ and $n_{bg} = 1.45$ while the perturbed fiber is shown in the inset of (b). The radius is 5 µm and the wavelength is 1 µm. We see that there is a good agreement between the exact solution and first order perturbation theory for small changes in Δn, which may be positive or negative.

Background perturbation in a teflon AF fiber

As a second example, we have a step-index fiber with core $n = 1.29$ which corresponds to the refractive index of Teflon AF [63]. The unperturbed background index is $n_{bg} = 1.60$ of high index liquids [64]. We introduce a perturbation into the system by only changing the background refractive index. The schematic for the unperturbed and perturbed fiber are shown in Fig. 4.6 (a). The radius of the fiber is 5 μm. These fibers with solid cores placed in liquids are used in evanescent field sensing, where the cladding modes interact with the exterior background [65].
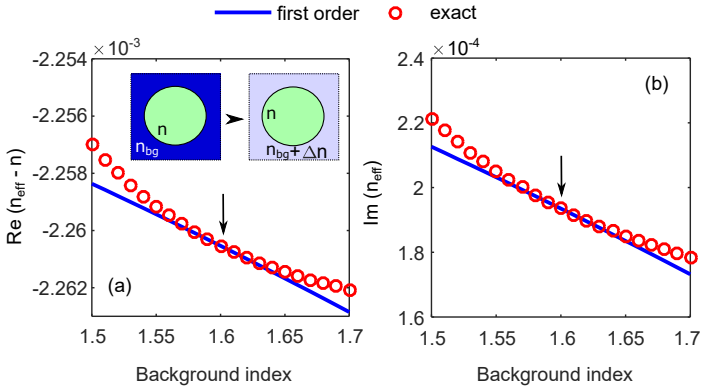
Figure 4.6: Comparison of the real (a) and imaginary (b) part of the effective index between exact solution and first order perturbation as a function of the background refractive index of the fundamental core mode for a step-index fiber. The radius of the fiber is 5 μm and the wavelength is 1 μm. The unperturbed values of refractive index are $n = 1.29$ (teflon AF) and $n_{bg} = 1.60$, indicated by the arrow. Note that the y axis in panel (a) shows the difference of the effective index and the core index to make visible the changes in effective index.

We now plot the comparison of the real and imaginary parts of the effective index between the exact solution and first order perturbation theory as a function of the background index. We see that the perturbation theory nicely agrees with the exact solutions for small changes in the background index but deviates for larger changes. The unperturbed background index is indicated by the arrow in Fig. 4.6 (a) and (b). The effective index is plotted for the fundamental core mode. Note that the y axis in Fig. 4.6 (a) is the difference between the effective index and the core index. It appears that the change in effective index is of the order of 10^{-3} for the real part while changing the background index. The wavelength is 1 μm.

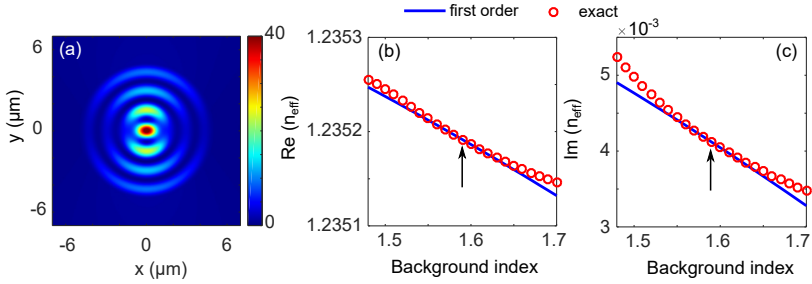We also plot the prediction of the effective index as a function of the chang-

Figure 4.7: (a) The absolute value of S_z (in a.u.) at a wavelength of 1 μm for a higher order core mode of a teflon fiber with core index 1.29 and unperturbed background index 1.59. The radius of the fiber is 5 μm. The comparison of the real (b) and imaginary (c) parts of the effective index as a function of changing background index. The unperturbed background index is indicated by the arrow in (b) and (c).

ing background index for a higher order core mode in Fig. 4.7. The absolute value of S_z for the higher order mode is plotted in Fig. 4.7 (a). The unperturbed background index is 1.59. All other parameters remain the same as in the previous example. It is seen in Fig. 4.7 (b) and (c) that there is a good agreement between the first order theory and exact solution for the higher order mode for both the real and imaginary parts of the effective index.

Background perturbation in a light cage structure

To increase the interaction of the background perturbation with the fundamental core mode, we now introduce a third example of a light cage [17, 66] structure to demonstrate the change in the propagation constant with changing background index. The schematic of this fiber structure is shown in Fig. 4.8 (b). We see that the light cage structure comprises of a single 12 strand ring of a dispersive polymer whose refractive index is given by [66]

$$n_{\text{polymer}} = \sqrt{1 + \frac{1.3424689\lambda^2}{\lambda^2 - 0.128436^2}} \tag{4.84}$$

where λ is taken in μm. The unperturbed background index is taken as $n_{bg} = 1.32$, which is the index of water [67]. The guiding mechanism of this light cage structure is an anti-resonant back reflection to the core. Such light cage structures have been experimentally fabricated [17, 66] and recently it has been shown that propagation of light also occurs in optofluidic mediums. As the hollow core itself is placed in liquid, the change in refractive index occurs in the core as well as the background as shown in the schematic in

Fig. 4.8 (b). Hence, the majority of the guided light interacts with the change in the environment, which can be very advantageous to monitor chemical and biological reactions. The strand radius of the light cage structure is taken as 1 μm and the pitch is 7 μm.
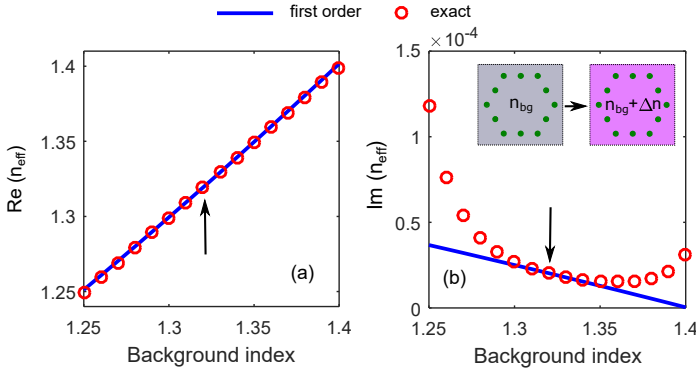

Figure 4.8: Comparison of the real (a) and imaginary (b) part of the effective index between exact numerical solution and first order perturbation as a function of background refractive index, of the fundamental core mode for a light cage structure surrounded by a liquid medium. The strand radius is 1 μm. The unperturbed background index is $n_{bg} = 1.32$, indicated by the arrow in the plots. The wavelength is 1.5 μm.

From Fig. 4.8 (a) and (b), we see that there is a good agreement between the first order perturbation theory and the exact numerical solutions, which have been obtained using the multipole expansion method [46] for the fundamental core mode. We also note from panel (a) that the agreement of the real part of the effective index and hence propagation constant is extremely good even for large changes in the background index. However, we see from panel (b) that the imaginary part deviates quickly due to its highly nonlinear behavior.

Hence, the first order perturbation theory has proved to be a very useful tool in predicting the perturbed propagation constant of structures with small perturbations in the exterior as well as interior of the structures, which is highly useful for defining the sensitivities and design rules for fiber sensing in a quick and efficient manner [30, 51].

4.3.2 k_0 **perturbation**

We now consider examples of k_0 perturbation, which we convert to λ, i.e., wavelength perturbation. Note that this is the only perturbation in the system and $\Delta\varepsilon$ and $\Delta\mu$ are considered to be zero. We also show that the perturbation theory is able to give exact values of group velocity in fiber structures.

Wavelength perturbation in a step-index fiber

We now discuss our first example, which is a capillary fiber with core refractive index $n = 1$ (air) and background refractive index $n_{bg} = 1.45$. The radius of the fiber is 5 μm. The schematic of the fiber structure is shown in Fig. 4.9 (a-b). The considered unperturbed wavelength is 1 μm, indicated by the arrows in panels (a) and (b). Note that the only change between the perturbed and unperturbed system is the wavelength, which is denoted by different color schemes in the schematic.

The comparison of the real and imaginary parts as a function of wavelength between the first order theory and exact solutions are shown in Fig. 4.9 (a) and (b), respectively, for the fundamental core mode. We see that there is a very good agreement between the two theories for a large range of wavelengths (0.8 μm - 1.2 μm) and for positive and negative changes in wavelength. Hence, the perturbation theory is very suitable for predicting the dispersion for small changes by solving the Maxwell's equations for only the unperturbed wavelength. The theory also gives an exact value of the slope of the dispersion curve, which corresponds to the prediction of group velocity.
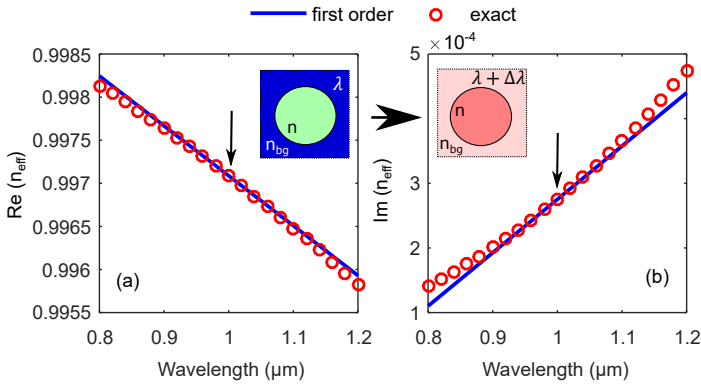

Figure 4.9: Comparison of the real (a) and imaginary (b) parts of the effective index between exact solution and first order perturbation as a function of wavelength for the fundamental core mode of a capillary fiber. The radius is 5 μm and the unperturbed wavelength is 1 μm (indicated by the arrow). The schematic of the fiber is shown in the insets. The refractive indices are $n = 1.00$ and $n_{bg} = 1.45$.

Wavelength perturbation in a silica air photonic crystal fiber

We now move on to a more complicated fiber structure of a silica air photonic crystal fiber and try to predict the real and imaginary part of the effective

index for changes in wavelength from the unperturbed wavelength of 1 μm for the fundamental core mode. The air inclusions have an index of 1, while the background index is 1.44. The pitch Λ is 2.3 μm. We see from Fig. 4.10 (a) and (b) that there is an excellent agreement between the exact numerical solution and first order perturbation theory for the real part for a range of radius of the air inclusions. Note that the only perturbation in the system is wavelength for each radius. Though there are deviations as we move to very large shifts in wavelength. We can see in Fig. 4.10 (c) and (d) we have nice agreement between the two theories even for the imaginary part but due to the higher nonlinearity of the imaginary part the deviations between the exact solution and first order perturbation theory arises much sooner.
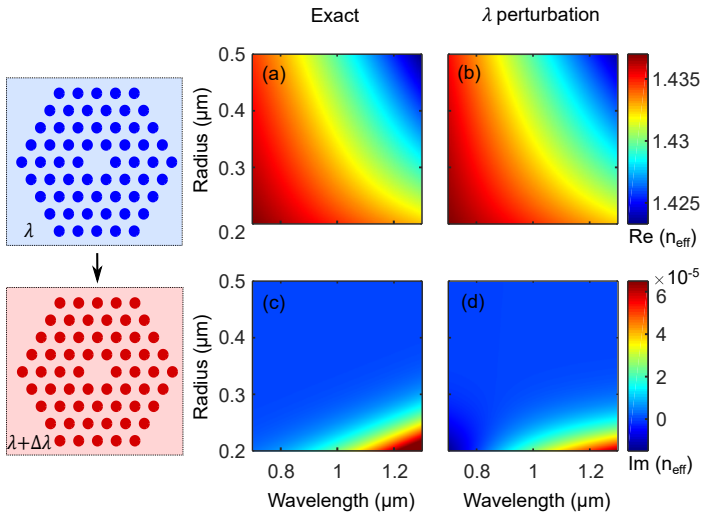

Figure 4.10: Comparison of the real (top row) and imaginary (bottom row) parts of the effective index of the fundamental core mode for a silica air photonic crystal fiber as a function of wavelength and strand radius, between exact numerical solution (left column) and first order perturbation theory (right column). The unperturbed wavelength is 1 μm. The background index is 1.44 with the index of air inclusions taken as 1 and the pitch is 2.3 μm.

We now compare the group velocities obtained from the first order theory and by taking a numerical derivative of the dispersion curve by repeatedly solving Maxwell's equations for close wavelengths. The expression of the

group velocity is given by [33]

$$V_g = \cfrac{c}{n_{\text{eff}} + \omega \cfrac{dn_{\text{eff}}}{d\omega}} \tag{4.85}$$

where ω is the angular frequency given by $\omega = ck_0$. Such a figure is plotted in Fig. 4.11 (a) and (b) for the fundamental core mode of a silica-air photonic crystal fiber as a function of wavelength and strand radius. The structure parameters are the same as in the previous example of Fig. 4.10. We see that the perturbation theory is able to predict the group velocity with very high accuracy and minimal computational effort. The relative error is of the order of $10^{-3}\%$.
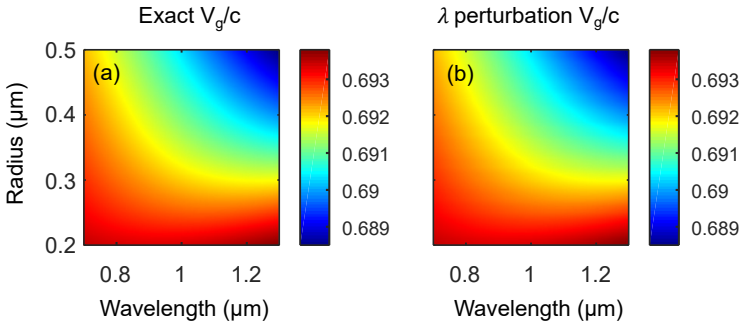

Figure 4.11: Comparison of the group velocity V_g/c between exact solution (a) and first order perturbation (b) as a function of wavelength and strand radius for the fundamental core mode of a silica air photonic crystal fiber. The structural parameters of the fiber are the same as in Fig. 4.10.

As a last example, we compare the effective index of a higher order cladding mode for wavelength perturbation. For this we use a silica air photonic crystal fiber with the refractive indices of the inclusions and background the same as in the previous example. We use an inclusion radius of $r = 0.5$ μm for the air inclusions with pitch 2.3 μm. The absolute value of S_z for the considered mode is plotted in Fig. 4.12 (a) at a wavelength of 1.19 μm, which is also the unperturbed wavelength. The comparison of the real and imaginary parts is plotted in Fig. 4.12 (b) and (c) for first order and exact numerical solutions, which agrees extremely well for the considered range of wavelengths.

With the above examples, we show that the λ perturbation theory is a very useful tool in predicting the dispersion of the propagation constant and the group velocity of the structures as a simple post processing step. We have shown its validity on fundamental and higher order modes of a silica air pho-
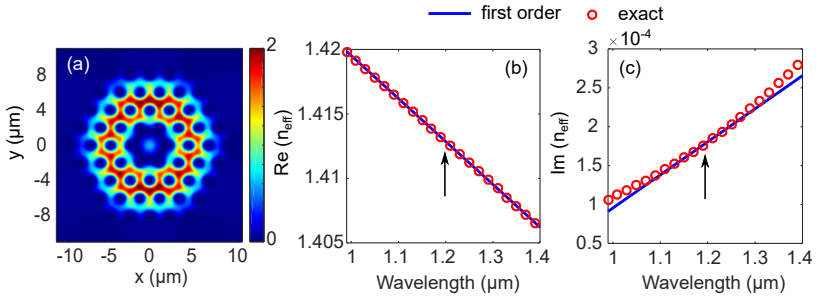
Figure 4.12: (a) Absolute value of S_z (in a.u.) at a wavelength of 1.19 μm for a higher order core mode of a silica air photonic crystal fiber with air inclusions having index 1 and 1.44. The radius of the inclusions are 0.5 μm. Comparison of the real (b) and imaginary (c) part of the effective index as a function of changing wavelength. The unperturbed wavelength is indicated by the arrow in (b) and (c).

tonic crystal fiber. However, if the perturbation is too high or there are multiple modes that are close to the considered unperturbed mode, then this leads to a highly nonlinear behavior. Hence, the first order perturbation theory will fail to accurately mimic the system and higher order perturbation theories or full numerical solutions may be required. Even with its deficiencies, perturbation theories have proved to be a useful tool for obtaining a fundamental understanding of the structure and generate simple design rules for optimization.

5 Design rules for confinement loss reduction

> "They're trying to kill me," Yossarian told him calmly. "No one's trying to kill you," Clevinger cried. "Then why are they shooting at me?" Yossarian asked. "They're shooting at everyone," Clevinger answered. "They're trying to kill everyone." "And what difference does that make?"
>
> Catch-22, Joseph Heller

Conventional step-index fibers, crossed the loss limit of 20 dB/km in 1970, taking their first step towards the utilization of optical fibers in communication systems [68, 69]. Further optimization of materials, design and wavelength of operation, in the coming decades has resulted in the ultimate loss limit of nearly 0.14 dB/km [70]. However, the fundamental limit in the performance of conventional optical fibers is now reached not only in terms of loss reduction but also in the optimization of other fiber properties such as dispersion, high power transmission, reducing nonlinearity, increasing bandwidth and so on [71].

Photonic crystal fibers provide a new way of improving the guiding properties of the conventional step-index fiber. They possess advantages like more flexibility in the dispersion and guiding properties due to the higher number of parameters, which can be manipulated [10] and most importantly the possibility of air guidance in the case of hollow-core photonic bandgap fibers. However, they have been unable to beat conventional step-index fibers in applications such as telecommunications. This is because the losses in fabricated photonic bandgap fibers are much higher than conventional step-index fibers. However, recent advances in loss reduction of both hollow-core [72, 73] and all solid photonic bandgap [74] fibers have lead to the lowest loss in such fibers to be around 1.7 dB/km [75].

To reduce the losses further we need to understand the loss mechanisms in PBG fibers:

- Finite cladding: Photonic bandgap fibers guide light using a bandgap effect [10], which arises due to the periodicity of the cladding. If the cladding is infinite then light is completely trapped in the defect core. Since fabricated photonic crystal fibers consist of only a few cladding rings light can escape through the fiber. Adding additional cladding rings helps reduce the losses of the fiber by almost one order of magnitude for each added cladding ring. The downside is that it also significantly increases the fabrication complexity of the fiber.

- Structural distortions: PBG fibers are much more complicated in their design when compared to their step-index counter parts. This in turn leads to many structural deviations from the perfect cladding, which affects their guiding properties and induce losses [41, 42]. This additionally can add surface modes and cladding supermodes which lowers the bandwidth [76].

- Frozen capillary waves: The fabrication of the fiber itself results in surface roughness because of the presence of frozen capillary waves [77]. These waves are thermodynamic in origin and hence, unavoidable in

the fiber and thus result in scattering losses. They tend to fundamentally limit the loss reduction of the fiber. However, optimizing the fiber design further can help overcome this loss barrier.

In this chapter, we focus on reducing the confinement loss of the fiber by optimizing the fiber design in high-index photonic bandgap fibers by making structural changes in the core surround.

5.1 Previous works of loss reduction in photonic bandgap fibers

There have been many attempts at loss reduction in photonic bandgap fibers by making structural changes in the core surround, as changes near the core cladding interface affect propagation of the fundamental core mode most significantly [76]. Some examples in literature of tailoring the guiding properties of fibers by structural design optimization are mentioned below:

- G. Ren et al., and W. Tong et al., in Ref. [78, 79] have introduced index depressed layers in each unit cell surrounding the high index inclusion of the all solid photonic bandgap fiber, which has shown to experimentally reduce confinement loss to as low as 2 dB/km and hence reduce transmission losses.

- J. H. Liu et al., in Ref. [80] show that by selectively filling the internal holes of a fiber with liquids and leaving the external cladding rings as air inclusions results in a slight reduce in the losses.

- Q. Fang et al., in Ref. [81] increase the diameter of two high index rods in the depth of the cladding and also in the core-cladding interface to show that this adds anticrossings and cladding supermodes. However, it also results in large waveguide group velocity dispersion at the center of the bandgap in the region of low loss.

- M. Pourmahayabadi et al., in Ref. [82] selectively modify the first ring along with selected inclusions of the second ring to smaller radius and higher index inclusions to form a snowflake like structure in the core surround while the other inclusions remain as air. This results in a fiber with a flattened dispersion and lower loss.

- P. Steinvurzel et al., in Ref. [83] reduces losses in photonic bandgap fibers by excluding certain strand inclusions in the core surround. However, this only works for the first bandgap.

- T. Yang et al., in Ref. [84] introduces a partially slotted core consisting of air slots to achieve low loss and a flattened dispersion in the THz regime.

There are of course many other works in the loss reduction of high-index and hollow-core PBG fibers by optimizing the structural design. Note that making changes to the core cladding interface is known to introduce additional modes such as surface modes in hollow core PBG fibers [85, 86] and cladding supermodes in high-index PBG fibers [81], which are generally known to increase the losses of the fibers and reduce the bandgap.

5.2 Fiber design and discussion

Here, we present our novel method of reducing confinement loss in photonic bandgap fibers by modifying the radius of specific strands, which we shall henceforth call "corner strands", as they form the corner vertices of the hexagon in the first cladding ring of the fiber. To demonstrate this mechanism of lowering losses, we consider an example photonic bandgap fiber with high index strands embedded in a low index background medium. The refractive index of the strands are n_{high} = 1.59, which correspond to CS$_2$ [87] and a background index of n_{low} = 1.44 corresponding to silica [88]. The strand radius is r = 0.764 μm and the center-to-center interstrand distance defined as pitch Λ is 3.82 μm, resulting in a radius-to-pitch ratio of r/Λ = 0.2. These parameters are chosen to obtain a loss minimum at a wavelength of 1.55 μm by enlarging the corner strands. The strands are placed in a triangular lattice forming four cladding rings while the core is comprised of 7 missing inclusions.

In Fig. 5.1, we observe two transitions of the unmodified fiber in the schematics. The top schematic shows the transition where all the strands of the unmodified fiber are increased upto R. In the bottom transition, only the radius of the corner strands are modified from $r \rightarrow R$ while the other strands remain unmodified. The bottom panel is our proposed structure of corner strand modification in photonic bandgap fibers. We now compare the losses of these transitions for different radii R.

For the structures with increasing strand radius [see Fig. 5.1 top schematic transition], the losses are plotted for the first and second bandgap in Fig. 5.1 (a). It is observed that the losses increase with increasing strand radii in both the first and second bandgaps. Note that the losses in panels (a) and (b) are

plotted as a function of the *V*-parameter defined as [33]

$$V = \frac{2\pi r \sqrt{n_{high}^2 - n_{low}^2}}{\lambda}. \tag{5.1}$$

Due to the dependence of the *V*-parameter on strand radius *r* and wavelength λ, we get a constant range of *V* values for changing strand radii in the first and second bandgaps. Futhermore, it is observed that the losses in the second bandgap are even lower than that of the first bandgap. This maybe due to the low index contrast between the CS_2 strands and the silica background of the test fiber [89].

The losses for changing corner strand radii are plotted in Fig. 5.1 (b), for the first and second bandgaps as a function of wavelength. The *V*-parameter axis of panel (a) is also valid for panel (b), however the reverse is not true. We see from panel (b) that selecting an optimal corner strand radius *R*, for each bandgap, can lead to a lowering of loss by almost two orders of magnitude. We further compare our results of modified corner strands to the structure of missing corner strands proposed by Steinwurzel et. al. in Ref. [83]. The loss of the missing corner strands structure is plotted as the blue dotted line in Fig. 5.1 (b). We observe that this structure is very effective in reducing losses in the first bandgap. However, it completely fails to do so in the second and higher order bandgaps. The results of the higher order bandgaps are not shown in the current work. Here, we only demonstrate the first and second bandgaps. Modifying the corner strand radius seems to be a simple way of reducing losses by orders of magnitude without highly changing the structure or increasing fabrication complexity.

However, the modification of the corner strand radius to *R* fundamentally changes the dispersion of the effective index by adding additional modes into the bandgap region of the fiber that effectively reduces the bandwidth. This can be seen as the highly lossy peaks in Fig. 5.1 (b). These modes which we call here as "cladding supermodes" are hybrid modes between the core and the first cladding ring of the fiber structure [81, 89].

To get an understanding of this low loss behavior, we now look into the effective index of the lowest loss structures in the first and second bandgaps as a function of wavelength. In Fig. 5.2, the dispersion of the real and imaginary parts of the effective index are plotted in (a) and (b), respectively, for the three structures of perfect, missing and enlarged ($R = 1.16$ μm) corner strands, in the first bandgap. The radius for the enlarged corner strand structure has been optimized to get the lowest loss by modifying the corner strands.

We can see that the unmodified and missing corner strand structures have a smooth dispersion for both the real and imaginary parts with high losses close to the band edges and a loss minimum at the center. Also note that
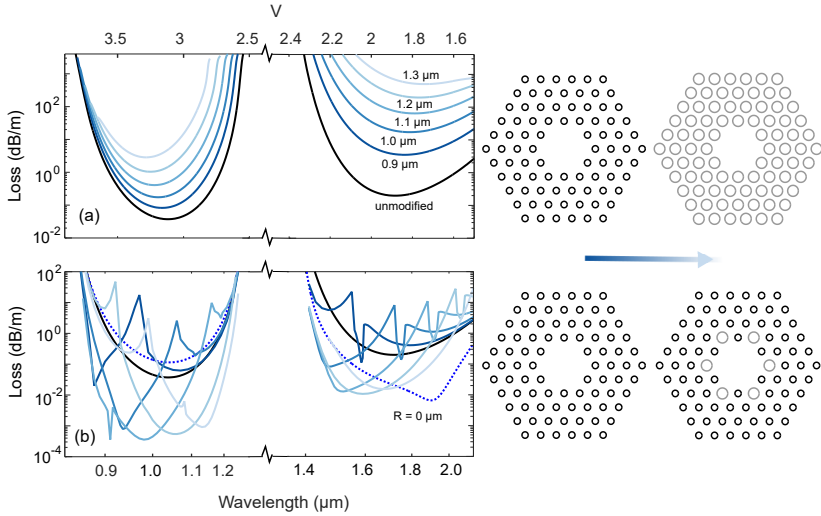
Figure 5.1: (a) Loss as a function of V parameter for varying strand radius r for the first (right) and second (left) bandgap. Schematics of the structures with increasing strand radius are shown on the top right, for a constant pitch of $\Lambda = 3.82$ μm. Panel (b) displays the loss for different corner strand radii R for the first and second bandgap. The strand radius of the unmodified structure is $r = 0.764$ μm. A schematic along with its modified version with enlarged corner strands (gray circles) in the core surround is shown on the bottom right. Comparison of panels (a) and (b), with the scale of loss being two orders of magnitude lower in (b), reveals that the optimal structure with the lowest loss is obtained in the first and second bandgap for missing (blue dotted line) and modified corner strands (blue solid lines), respectively. Note that the V parameter axis holds for top and bottom panels, while the wavelength axis is only valid for the bottom axis.

the dispersion of the real part [see Fig. 5.2 (a)] is very similar for the missing and unmodified structures. In the case of the modified (enlarged) corner strand structure, we observe three distinct dispersion curves and their anti-crossing with cladding supermodes. To get a further insight into the nature of these dispersion curves we take a look at the Poynting vector plots at different wavelengths in the dispersion curves.

We plot the absolute value of S_z, i.e., the z component of the time averaged Poynting vector, in Fig. 5.2 (c-k). This quantity can be physically interpreted as the energy travelling in the z direction, which we have chosen as the translationally invariant direction [33]. The fields have been normalized using the analytical normalization derived in Chapters 2 and 4, making a comparison of the fields and energy distribution feasible for different fiber structures. Due
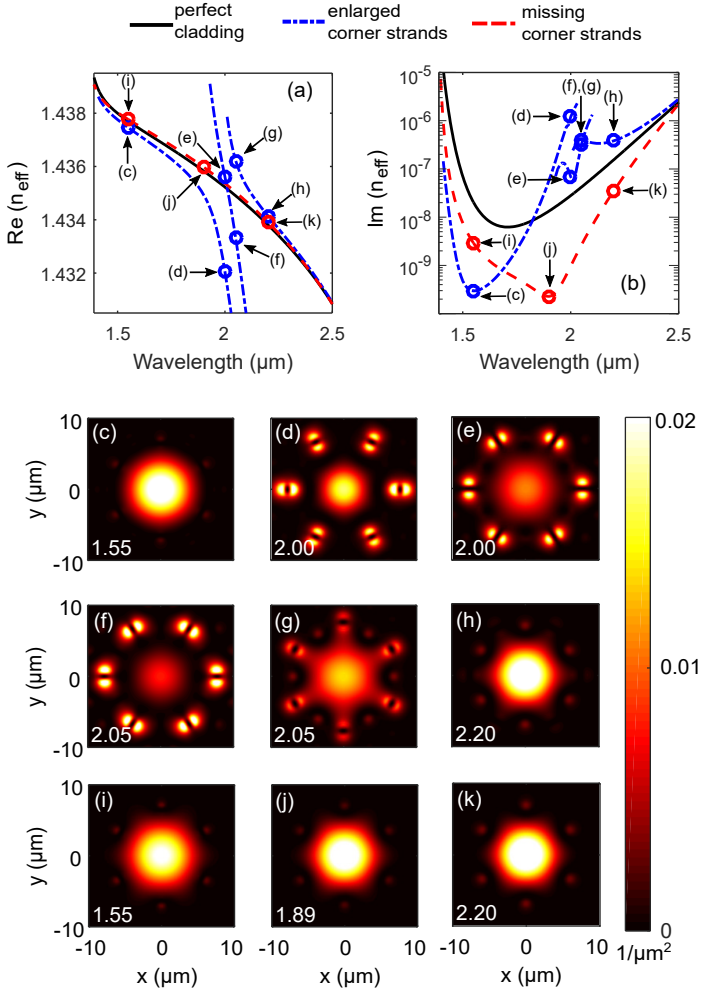
Figure 5.2: Real (a) and imaginary (b) part of the effective index of the fundamental core mode and its possible anticrossings with cladding supermodes with (blue dashed-dotted lines) and without (black solid lines) and missing (red dashed lines) enlarged corner strands in the core surround for the first bandgap. The corner radius is 1.16 μm, which corresponds to the lowest loss structure by modifying the corner strands. The normalized absolute value of the z component of the time averaged Poynting vector divided by $c/8\pi$ for x-polarized modes is plotted at different wavelengths of the dispersion curve in panels (c-k). The bottom row (i-k) is for the missing corner strand structure while panels (c-h) correspond to enlarged corner strand structure. The wavelengths in μm are indicated in the insets of the color plots.

to this normalization the unit of the fields is 1/μm. The position of these plots are marked in the dispersion curves of (a) and (b) and the wavelength is written in the inset of each field plot in μm. Taking a look at (c), we see that the mode is very fundamental like with most of its energy confined in the core. It has orders of magnitude lower loss, which can be deduced from the imaginary part of the effective index, when compared to the unmodified cladding structure. As we move along the dispersion curve and get closer to the anticrossing and hence the cladding supermode, we see that more and more fields are leaking to the modified corner strands and very little energy remains in the core [see Fig. 5.2 (d)]. We also see that the losses of the mode have drastically increased within the bandgap region.

We now jump to the second dispersion curve moving through the anticrossing to (e) and (f), where most of the fields are still confined in the enlarged corner strands but there is some energy remaining in the fiber core. It is interesting to note that the nodes near the modified corner strands have a different orientation as we move through the anticrossing to the cladding supermode. The losses of the cladding supermode are quite high when compared to the lowest loss of the unmodified and enlarged corner strands structures. We finally jump over the second anticrossing to the third dispersion curve with the modes plotted in (g) and (h). We can again see that the mode has become more fundamental like, and as we pass through the dispersion curve, more and more energy returns back to the core of the fiber [see Fig. 5.2 (h)]. Interestingly, the node in the enlarged corner strands has reverted back to its original orientation as we jumped the second anticrossing [see Fig. 5.2 (f) and (g)]. However, the losses in the third dispersion curve still remains higher than even the unmodified cladding structure and the low loss regime of the fiber does not reappear in the case of enlarged corner strands.

We also plot the absolute value of S_z for the case of missing corner strands at three different wavelengths in Fig. 5.2 (i-k). We can see that due to the lack of any additional modes introduced by a change in radius, the dispersion curve remains smooth and the energy is highly confined in the core for all the three wavelengths. We also see that for the first bandgap, we have an almost similar loss reduction by enlarging or removing the corner strands, with the structure of missing corner strands being slightly better as can be seen in Fig. 5.2 (b). The missing corner strand structure manages to reduces losses without decreasing the bandwidth of the fiber.

We have so far looked at the energy that is confined in the core and near the core surround. Now we take a closer look at how energy escapes the fiber structure into the homogeneous exterior and compare this for different fiber geometries in the first and second bandgaps. We start with the first bandgap and plot the S_z and S_ρ components of the modes at the wavelength

of lowest loss for their respective structures in Fig. 5.3 for the missing (a), unmodified (b) and enlarged (c) corner strands (same as Fig. 5.2). The plots marked (1), i.e., the top row corresponds to the S_z component while the bottom row marked (2) corresponds to the S_ρ component for each structure. We plot these components to physically analyze the flow of energy in the translationally invariant z direction and the leakage of energy in the ρ direction, as we move away from the fiber. The fields have been normalized by using the analytical normalization of Eq. (2.35), so that such a comparison becomes physically meaningful. We can see that the leakage of energy is maximum for the unmodified fiber structure (b) in both the z and ρ components, where we see large amounts of fields escaping to the homogeneous exterior. In both missing (a) and enlarged (c) corner strand structures, the leakage to the homogeneous exterior has drastically reduced, which is especially evident in the radial component of the Poynting vector, see Fig 5.3 (a2) and (c2). The arrow in the top row indicates x polarized modes. Hence, we can conclude that with the low loss structures the escape of energy to the exterior background is drastically reduced.
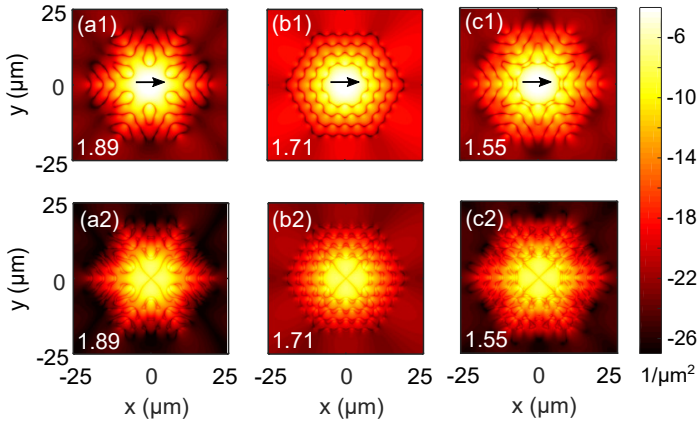

Figure 5.3: The normalized absolute value of the z and ρ components (marked as 1 and 2, respectively) of the time averaged Poynting vector divided by $c/8\pi$, in logarithmic scale, for x-polarized modes plotted at the wavelength of lowest loss for enlarged (c), unmodified (b) and missing (a) corner strands, in the first bandgap. The field distributions have been normalized analytically, so that the comparison of the magnitudes becomes physically meaningful. The wavelength are written in the insets of each panel in μm.

Now let us move to the second bandgap and study the fields and dispersion for the lowest loss structures. In the second bandgap, we take a look at the

dispersion of four different structures having missing, reduced, unmodified and enlarged corner strands as can be seen in Fig. 5.4 (a) and (b). We consider two radii of the modified corner strands structures, i.e., reduced strands of $R = 0.27$ μm and enlarged strands of $R = 1.11$ μm as the losses are around the same order of magnitude for both these structures. These particular radii are the optimized lowest loss corner strand radii in the regime of reducing and enlarging corner strands compared to the unmodified radius. It is evident from Fig. 5.4 (a) and (b) that in the region of the bandgap, the missing and unmodified corner strands have a smooth dispersion for both the real and imaginary parts. The glaring difference between the first and second bandgap is that in the case of the second bandgap, the missing corner strands structure fails to reduce the losses in comparison to the unmodified structure, while the structures with modified corner strands, both reduced and enlarged, succeed in reducing losses by orders of magnitude. However, the dispersion behavior of the enlarged and reduced corner strands appears to be quite different from each other. We see that the enlarged corner strands introduce additional cladding supermodes and anticrossings in the bandgap region. This is missing in the case of the reduced corner strands structure, where the dispersion appears to be quite smooth throughout the bandgap [see Fig. 5.4 (a) and (b)]. Also, the loss with the reduced corner strands is slightly lower when compared to the enlarged corner strands structure.

We now take a look at the leakage of energy to the exterior background in the second bandgap. This is done for the four structures mentioned above at the wavelength of lowest loss for their respective structures. Such a plot comprising the normalized S_z and S_ρ components can be found in Fig. 5.4 (c-f). Similar to Fig. 5.3 the top row marked 1 is the S_z component while the bottom row marked 2 is the S_ρ component of the x polarized fundamental core modes. We see that for the structures with missing and unmodified corner strands [see (c) and (d)], in which no reduction of loss is observed, there is a high leakage of energy to the homogeneous exterior with the missing corner strands having the highest leakage. We also observe a drastic reduce in this energy leakage for both the modified corner strands structures [enlarged (e) and reduced (f)].

This shows that the presence of the modified corner strands redistributes the energy in the fiber leading to much lower losses and much less energy leakage. To get an insight on how this redistribution occurs, we plot the real part of the ρ component of the Poynting vector in four directions i.e. from the center to each unique inclusion of the fiber in the first cladding ring.

Such a plot for the first bandgap is shown in Fig. 5.5. The panels (a) to (c), show the real part of S_ρ as a function of distance from the center in four different transverse directions indicated in the left hand side of each plot for
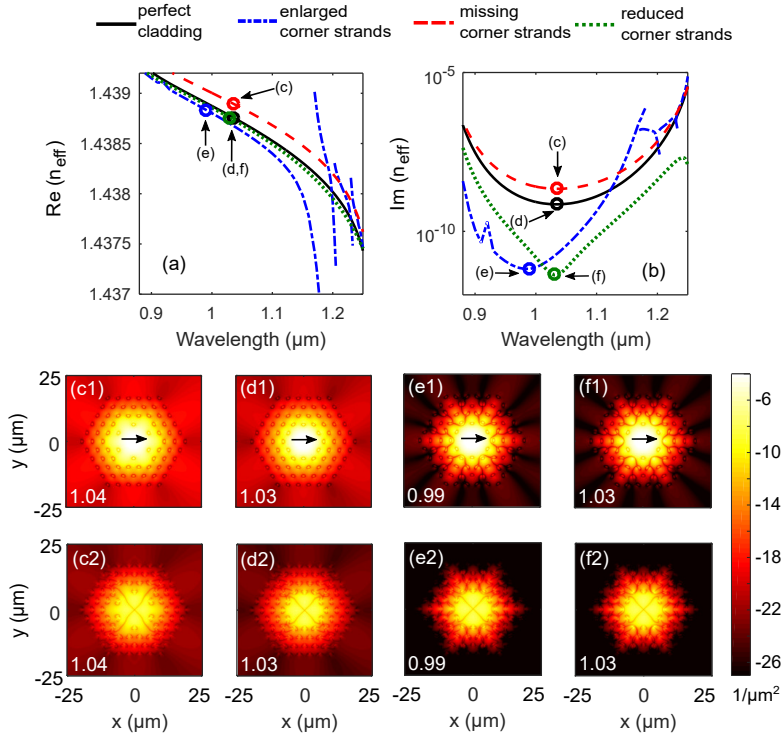
Figure 5.4: Real (a) and imaginary (b) part of the effective index of the fundamental core mode and its possible anticrossings with cladding supermodes for enlarged (blue dashed-dotted lines), unmodified (black solid lines), missing (red dashed lines) and reduced (magenta dotted lines) corner strands in the core surround for the second bandgap. The corner radius for enlarged strands is 1.11 μm, which corresponds to the lowest loss structure by enlarging the corner strands. The corner radius for reduced strands is 0.27 μm, which corresponds to the lowest loss structure by reducing the corner strands. The normalized absolute value of the z and ρ components in logarithmic scale (marked as 1 and 2, respectively) of the time averaged Poynting vector divided by $c/8\pi$ for x-polarized modes plotted at the wavelength of lowest loss for missing (c), unmodified (d), enlarged (e), and reduced (f) corner strands (in descending order of loss) in the second bandgap. The field distributions have been normalized analytically, so that the comparison of the magnitudes becomes physically meaningful. The wavelengths of lowest loss for each structure are indicated in the insets of the color plots in μm.

the cases of missing (a), unmodified (b) and enlarged (c) corner strands. We can see that in (a) and (c), the real part of S_ρ has large negative peaks at the wavelength of lowest loss. These negative peaks can be interpreted as energy flowing back into the core due to the presence of these modified and missing strands, instead of just moving away from the fiber core. The position of the first strands in each direction is indicated by the green vertical lines. It can also be seen in panel (b) that for the unmodified structure, these negative peaks are missing, hence there is no energy flow or backscattering of light back into the core giving rise to a lower loss.

In panels (d) to (f) of Fig. 5.5, we plot the real part of S_ρ as a function of wavelength at the particular positions of the center rods in the first cladding ring in the four unique directions of the fiber. Note that for the case of missing corner strands, there are no rods in the corner directions. The imaginary parts of the effective index is also plotted on the second y axis and the wavelength of lowest loss is indicated by the purple vertical line for each case. The interesting thing we observe in Fig. 5.5 (d) and (f) is that there is an exchange of the rods that backscatter light close to the wavelength of lowest loss, which is not observed in the unmodified structure (e), where no backscattering occurs. We can also see that around the wavelength of lowest loss the values of S_ρ are very small, leading to the conclusion that very little energy escapes in the transverse direction. This shows that for the case of the modified corner strands, an optimal point of the backscattering of rods is reached, which reduces the leakage to the exterior homogeneous medium drastically and is responsible for the added lowering of loss.

Let us see if a similar behavior is observed also in the second bandgap. For the second bandgap, we plot the same figures as in Fig. 5.5 but for four different structures as described in Fig. 5.4, which are missing (a,e), reduced (b,f), unmodified (c,g) and enlarged (d,h) corner strands. From the observations made in the first bandgap, we would expect to see no backscattering of light into the core for the unmodified structure and also the missing corner strands structures since the case of missing corner strands failed to reduce the losses in the higher order bandgaps. We can see that that is in fact true in panels (a) and (c). But for the case of the modified corner strands with reduced and enlarged strands, we observe strong backscattering of light back into the core. Interestingly, the backscattering of light to the core seems to occur predominantly in only one direction for the reduced corner strand structure at the wavelength of lowest loss. We also note that the y scale is almost two orders of magnitude lower for the modified corner strand structures than the missing and unmodified cases, which shows that there is a lot less energy escaping in the radial direction at the wavelength of lowest loss.

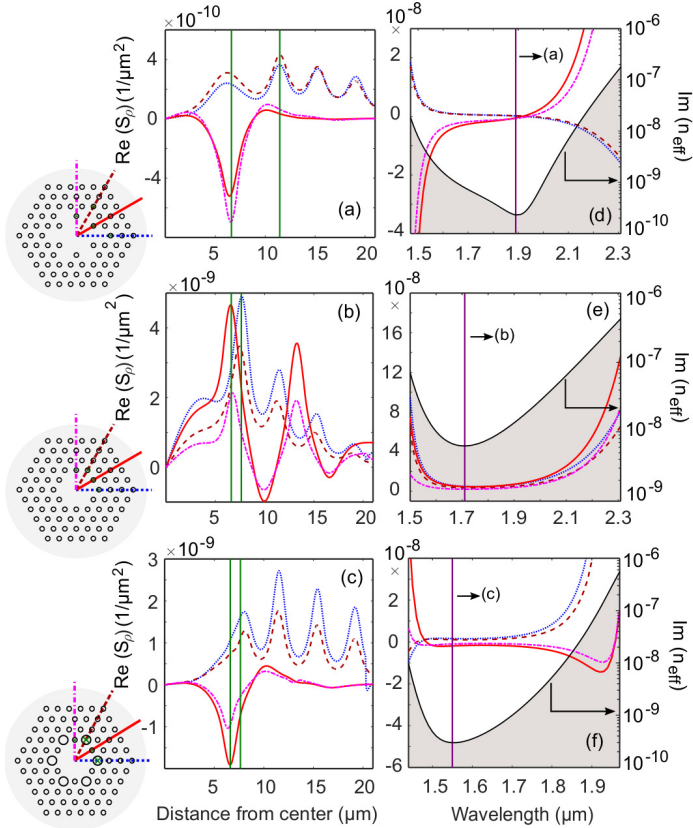We can also see in panels (f) and (h) of Fig. 5.6, that again an interchange

Figure 5.5: Real value of the time-averaged Poynting vector divided by $c/8\pi$, in the radial direction for the x-polarized fundamental mode in the first bandgap, with missing corner strands at $\lambda = 1.89\,\mu m$ (a), unmodified cladding at $\lambda = 1.71\,\mu m$ (b) and with enlarged corner strands ($R = 1.16\,\mu m$) at $\lambda = 1.55\,\mu m$ (c). All other parameters are the same as in Fig. 5.2. The selected wavelengths correspond to the minimum loss of the respective structures. The fields are plotted in four different transverse directions from the center as shown in the insets. The vertical lines in (a-c) mark the position of the center of the first inclusion in each direction. The right panels display the spectral distribution of the real part of the radial Poynting vector component divided by $c/8\pi$, at the center of the rods along these directions for missing (d) without (e) and with (f) enlarged corner strands. The gray curve indicates Im(n_{eff}) of the respective structures (right axis). For the sake of comparability, the field distributions have been normalized analytically. The vertical lines in (d-f) mark the wavelength of lowest loss. It can be seen in (a) and (c), that backscattering of light to the core occurs in the presence of the enlarged and missing-corner-strand structures, resulting in a decrease of the fiber loss.
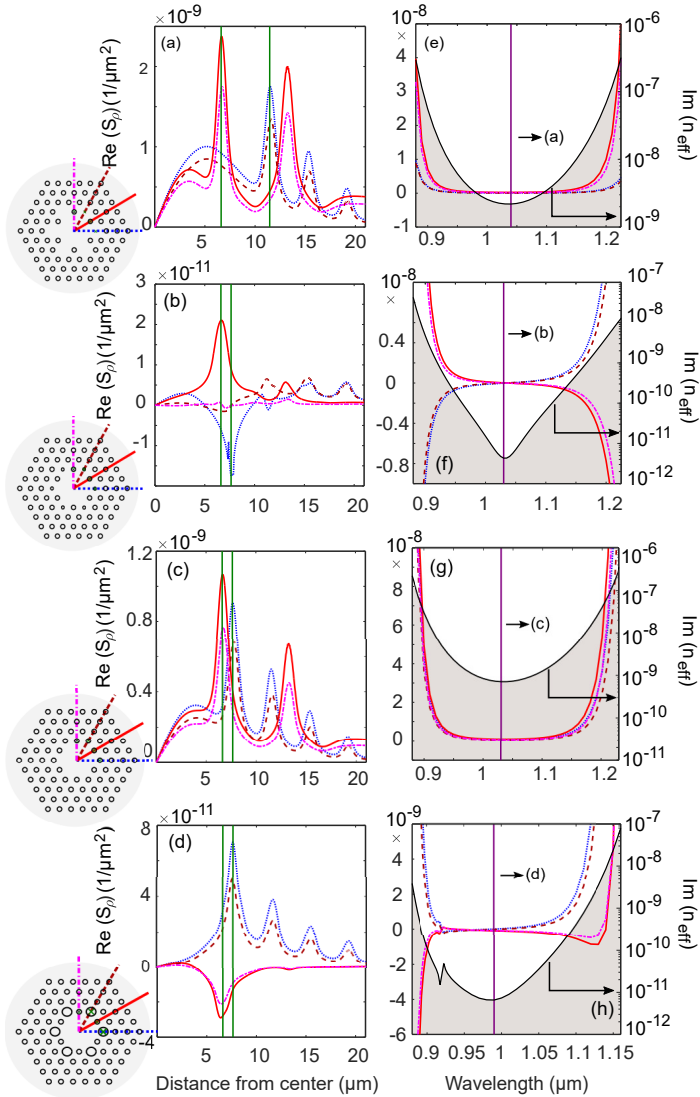
Figure 5.6: Results equivalent to Fig. 5.5, but for the second bandgap, with missing corner strands (a,e), reduced corner strands ($R = 0.27$ μm) (b,f), unmodified cladding (c,g), and enlarged corner strands ($R = 1.11$ μm) (d,h). It can be seen that backscattering of light to the core occurs for the second bandgap only in the presence of the modified corner strands. The vertical lines in (e-h) mark the wavelengths of lowest loss.

of the rods that backscatter light back to the core takes place close to the wavelength of lowest loss, which is especially prominent in (f). Hence, the low loss of the fibers with modified corner strands can be interpreted as the redistribution of energy in the fiber core due to the backscattering of light in the presence of the modified corner strands. When an optimum value of the backscattering is reached we get the lowest loss of the structure.

5.3 Design optimization: a parametric study

In the previous section, we have gained a basic understanding on the reason for this low loss behavior. Now, we do a parametric analysis by changing values like R, r/Λ and Λ to obtain the optimal structure from the fabrication standpoint. The only parameters that are kept constant are the material refractive indices.

We first start out with plotting the loss of the structures (in logarithmic scale) as a function of wavelength and corner strand radii. In Fig. 5.7, we have plotted this for two different ratios of r/Λ over the first and second bandgap. Note that the x axis is the V parameter with only the wavelength modified, while the y axis is the ratio of the corner strand radius to the strand radius. The white line marks the unmodified structure. Taking a first glance at Fig. 5.7 (a-d), we see that for each ratio of r/Λ and in each bandgap, there is a region of lower loss above and below the unmodified structure, which corresponds to structures with modified corner strands. We also deduce from panels (a) and (c), that the ideal choice of the corner strand radius for the first bandgap depends on the ratio of r/Λ since, for the case of $r/\Lambda = 0.3$ the missing corner strands do not provide the lowest loss. It appears that a reduced corner strand structure would be the better choice.

In the second bandgap, we observe that even though the reduced corner strand structures provide the lowest loss values in either r/Λ ratio, it comprises of a very narrow low loss region. This means that the fabricated fiber, which may be prone to structural distortions may miss this region completely. However, we see that enlarging the corner strands, always provides a broad region of lowered loss, irrespective of bandgap and the r/Λ ratio. We also notice lines of high losses which correspond to the cladding supermodes and it's anticrossing with the fundamental core mode.

Hence, we see that the modification of the corner strands is a more universal way of lowering loss in photonic bandgap fibers and the interplay of the large and small corner strands plays a significant role in lowering the losses by backscattering light to the core.

We now study the minimum loss as a function of strand radius and corner strand radius keeping the pitch Λ constant at 3.82 μm. Hence, this leads to
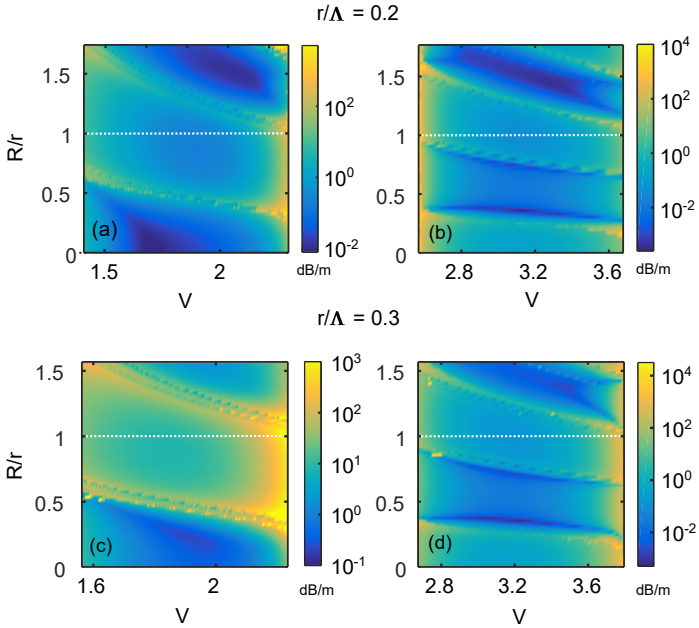
Figure 5.7: Loss as a function of V parameter and the ratio between corner strand radius R and strand radius r in the first (a,c) and second (b,d) bandgap for $r/\Lambda = 0.2$ (a, b) and $r/\Lambda = 0.3$ (c, d). Evidently, the ideal choice of corner strand radius significantly depends on the bandgap and the ratio of strand radius and Λ.
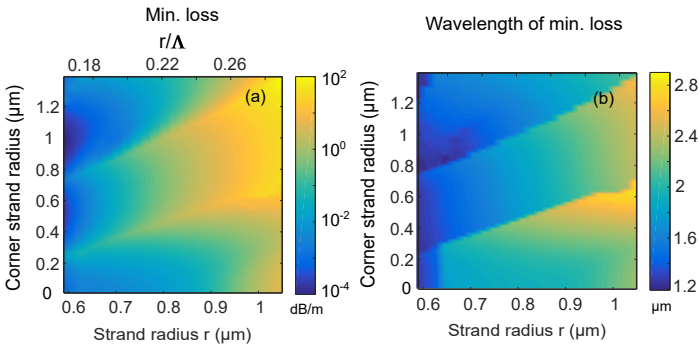

Figure 5.8: Minimum loss (a) and wavelength of its occurence (b), as a function of strand radius r and corner strand radius R, for the first bandgap in the case of a constant period of $\Lambda = 3.82$ μm.

a parametric study of the minimum loss over R and r/Λ. The minimum loss in logarithmic scale is plotted in Fig. 5.8 (a) and the wavelength of its occurrence in (b) for the first bandgap. We first observe in panel (a), that lowering the strand radius reduces the losses monotonously like in the case of Fig. 5.1. However, lowering the strand radius also means reduced guidance of the mode, as the limiting case of $r \rightarrow 0$ gives a loss less mode of homogeneous space that is not guided.

To quantify the amount of guidance in a physically meaningful manner, we use the absolute value of the normalized electric field at the center of the fiber core. A greater value of the fields at the origin (0,0) of the fiber would mean higher intensity of light trapped at the center and hence a higher degree of guidance. This is plotted in Fig. 5.9 as a function of strand radius and corner strand radius at the wavelength of the lowest loss, for each fiber structure. The white line in the figure indicates the structures that have the same strand and corner strand radius. Following the white line in Fig. 5.9, we see that as the strand radius r is increased we get higher and higher values of fields in the core. This means that the modes are more guided in a fiber with larger strands even though they have higher losses. However, we see that enlarging the corner strands gives higher values of the fields in the core, even for fibers with small strand radius, while also achieving a much lower loss as can be seen in Fig. 5.8 (a).
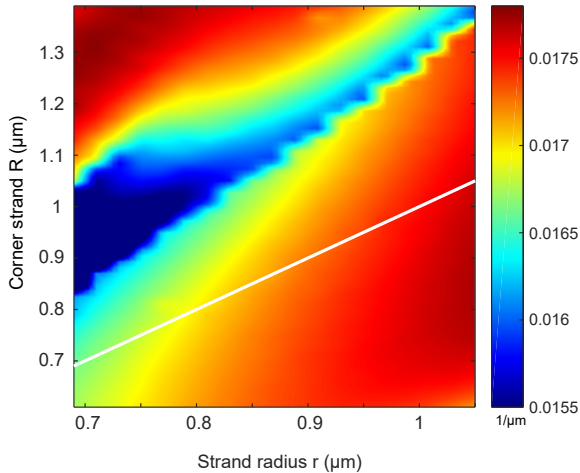

Figure 5.9: Absolute value of the normalized electric field in 1/μm, at the center of the fiber core as a function of strand radius r and corner strand radius R. The white line indicates the structures with $r = R$. We see that the electric field at the center increases with larger strand radii.
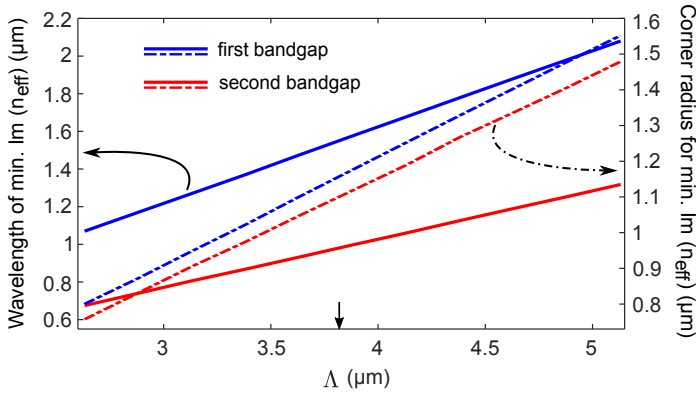
Figure 5.10: Wavelength of minimum Im (n_{eff}) (left axis, solid lines) and corner radius for minimum Im (n_{eff}) (right axis, dashed-dotted lines) as a function of pitch (Λ) for the first (blue lines) and second (red lines) bandgaps. The ratio of radius-to-pitch is kept constant at $r/\Lambda = 0.2$. The arrow on the x axis indicates the pitch used in all previous plots.

We can also see in Fig. 5.8 (a), that different regions provide the lowest loss for different ratios of r/Λ (top axis). For smaller r/Λ ratios, we see that enlarging the corner strands gives the lowest loss, while for higher r/Λ ratios, reduced corner strands results in the best fiber. We also notice that in Fig. 5.8 (b), the wavelength plot has huge discontinuities. This is because the region of lowest loss has shifted from wavelengths above the anticrossing to wavelengths below the anticrossing with the cladding supermodes.

We also plot in Fig. 5.10 the wavelength of minimum loss and the corner strand radius for minimum loss, only for the case of enlarging the corner strands, as a function of period, by keeping a constant r/Λ ratio of 0.2. Note that irrespective of the strand radius the minimum loss remains constant for a particular r/Λ value as the V parameter remains constant. For the case of $r/\Lambda = 0.2$, the imaginary part of the effective index is nearly 2.89×10^{-9}. From the figure we see that the behavior of wavelength and radius for minimum loss is linear with respect to period. This shows that the design is essentially very scalable and can be used to get a loss minimum at the wavelength of choice by modifying the period and the r/Λ ratios for the fundamental core mode.

Hence, we have shown a new way of decreasing losses by modifying the corner strands, which is fabricationally easy to achieve without adding additional complexity to the structure like adding more cladding rings.

5.4 Single ring structures

Here, we would like to show two additional examples to prove the true flexibility of the corner strand modification design. We first apply the corner strand modification to light cage structures. For a second example, we consider changing the index of the corner strands instead of the radius since the *V* parameter also depends on strand index. We do this for the same test fiber as before but consider only the first cladding ring. This is because the core cladding interface seems to be the most significant for this effect as the backscattering occurs from the modified corner strands and the additional cladding rings provide a further bandgap effect to lower losses.

5.4.1 Implementing corner strand modification for a light cage structure

We show that the approach of corner strand modification for achieving low loss structures is not only applicable for photonic bandgap fibers but also single ring 12 strand light cage structures [17]. We have plotted in Fig. 5.11, the imaginary part of effective index as a function of wavelength for two different types of structures similar to Fig. 5.1. In Fig. 5.11 (a) the radius of all the strands in the light cage structure is increased. The unmodified structure has a strand radius $r = 1.55$ μm and a period of $\Lambda = 6$ μm. We see that the losses do not reduce for the case of increasing strand radii. We now apply our corner strand modification design and plot the imaginary part of the effective index for different corner strand radii. We see that the losses decrease by orders of magnitude compared to the unmodified structure. The schematics of the two fiber structures are shown in Fig. 5.11 on the right. Note that the rods colored purple are the rods whose radii are changed in the figure. The background index is air with $n = 1$ and the strands are made of a dispersive polymer with refractive index as given in Ref. [66] and described in Eq. (4.84).

5.4.2 Change of refractive index in the core surround

We now try to see if the change in refractive index in the core surround can mimic the same effect of lowering the imaginary part of effective index and hence losses. We use the same test fiber with CS_2 high index strands and silica background. However, we only use a single ring structure. The schematic of this fiber is shown in Fig. 5.12, where the index of only the corner strands are varied. We now plot the imaginary part of effective index for different corner strand index and compare its losses with the case of the unmodified corner
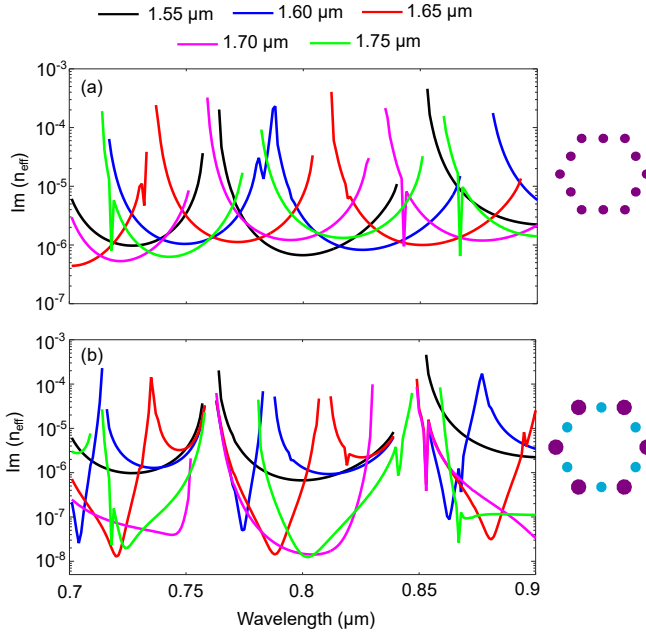
Figure 5.11: Imaginary part of the effective index for light cage structures without (a) and with (b) corner strand modification. The radius of all the strands in panel (a) are varied while only the corner strand radii of panel (b) are changed. The strands with changing radius are indicated in purple in the schematics. The unmodified structure has a radius of 1.55 μm (black curve) and pitch $\Lambda = 6$ μm. The background index of the light cage structure is air ($n_{bg} = 1$), while the strands are made of a dispersive polymer with refractive index as described in Ref. [66]. We see that even for the single ring light cage structure we observe a loss reduction of orders of magnitude with corner strand modification than the unmodified structure.

strand index in Fig. 5.12.

We see, at a first glance, that changing the refractive index does reduce the losses by orders of magnitude. However, taking a closer look we realize that the dependence of the lowering of loss with changing refractive index is quite low. The noticeable change that occurs, after a certain degree of lowering of loss, is the shift in wavelength of minimum loss with changing refractive index in the corner strands.

In conclusion, we have introduced a novel way to reduce losses of the fundamental core mode in fiber structures with high index strands by introducing corner strand modification in the core surround. We have shown that we can reduce the losses by orders of magnitude when compared to the unmodi-
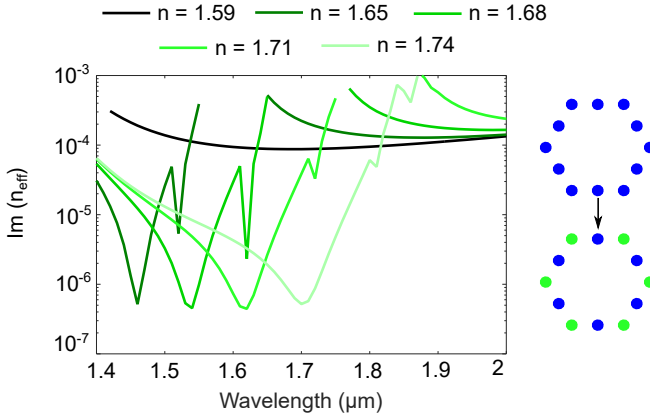
Figure 5.12: Imaginary part of the effective index as a function of wavelength for the fundamental core mode of a single ring structure with changing refractive index in the corner strands. The strand radius is $r = 0.764$ µm and period $\Lambda = 3.82$ µm. The unmodified structure (black solid line) has $n_{high} = 1.59$ with the background index as $n_{low} = 1.44$. It is seen that the losses decrease by orders of magnitude even while changing the index of corner strands.

fied cladding structure without increasing the fabricational complexity of the cladding. The optimized radius of corner strands for the lowest loss could be missing, reduced or enlarged corner strands depending on the bandgap and r/Λ ratios. We have shown that the case of missing corner strands suggested by Steinwurzel et al. in Ref. [83] does not apply to higher order bandgaps and works only for certain ratios of r/Λ in the first bandgap. Also note that since the reduction in losses highly depends on the *V*-parameter the effect caused by enlarging the strand radius can be mimicked by increasing the index of the corner strands to get similar results.

6 Additional applications of the normalization

This is all very confusing, especially when we consider that even though we may consistently consider ourselves to be the outside observer when we look at the rest of the world, the rest of the world is at the same time observing us, and that often we agree on what we see in each other. Does this then mean that my observations become real only when I observe an observer observing something as it happens? This is a horrible viewpoint.

Richard Feynman

Parts of this work is already published in *I. Allayarov, S. Upendar, M. A. Schmidt, and T. Weiss, "Analytic mode normalization for the Kerr nonlinearity parameter: Prediction of nonlinear gain for leaky modes," Physical Review Letters **121**, 213905 (2018).*

6.1 Introduction

Since the derivation of the analytical form of the normalization we have seen that it can be used in many applications. In this thesis, we have shown important applications of this normalization in the form of developing internal and external perturbation theories. We have shown that this normalization gives the correct weight for the pole expansion of the Green's dyadic using the Mittag-Lefler theorem and hence can be used to predict the resonant states of a perturbed system in terms of the resonant states of the unperturbed system. We have also shown how this normalization can be used to compare the fields of different fiber structures and hence give us a physically meaningful comparison of the flow of energy. This has been extremely useful in analyzing the effect of low loss fiber structures by varying the radius of the corner strands in the core surround.

The use of the normalization is however not limited to these applications. The problem of the normalization of leaky modes has existed in the fiber community for a very long time and hence analyzing and comparing leaky modes has always posed a difficulty for many field comparisons, calculations of nonlinear effects including the Kerr nonlinearity parameter, Purcell effect, four wave mixing and so on. The derivation of the correct normalization has now enabled us to tackle these problems with a new and better outlook.

Here, we show two additional instances in which this normalization has been applied to solve fundamental theoretical and experimental problems. The first is the redefining of the Kerr nonlinearity parameter for leaky modes. The second is providing the fraction of fields in the rods of an optofluidic light cage structure.

6.2 Analytical normalization for the Kerr nonlinearity parameter

The response of any medium towards high intensity light gives rise to nonlinearities. This nonlinearity is described by the induced polarization, where its dependence on the electric field is not linear. The polarization equation is given by [91],

$$\mathbf{P} = \chi^{(1)} \cdot \mathbb{E} + \chi^{(2)} : \mathbb{E}\mathbb{E} + \chi^{(3)} \vdots \mathbb{E}\mathbb{E}\mathbb{E} + \ldots \tag{6.1}$$

Here, $\chi^{(n)}$ is the nth order susceptibility tensor which depends on the dielectric medium. The linear response of the system is defined by first order of susceptibility i.e. the $\chi^{(1)}$ tensor. Often because of the molecular symmetry of the medium the second order susceptibility is zero. Hence, in practical optical fibers showing nonlinear effects the third order susceptibility plays a crucial role.

Calculation of nonlinear effects in fibers are chiefly done using two common methods. These are the iterative and perturbative approaches. While the iterative approaches rely on full numerical calculations of the system, the perturbative approaches treat the nonlinearity as a perturbation of the linear system since the polarization expression can be split as

$$\mathbf{P} = \mathbf{P}_L(\mathbf{r}, t) + \mathbf{P}_{NL}(\mathbf{r}, t). \tag{6.2}$$

Following the derivation of the nonlinear pulse propagation in fibers as in Ref. [91], we arrive at the so-called nonlinear Schroedinger equation, given as

$$\frac{\partial A}{\partial z} + \beta_1 \frac{\partial A}{\partial t} + \frac{i\beta_2}{2} \frac{\partial^2 A}{\partial t^2} + \frac{\alpha}{2} A = i\gamma |A|^2 A \tag{6.3}$$

Here, A is the amplitude of the envelope pulse which travels at a frequency of ω_0. The normalization is taken such that $|A|^2$ represents the optical power. The quantities β_1 and β_2 represent the inverse of the group velocity and the group velocity dispersion, respectively. The group velocity (v_g) is defined as the velocity with which the pulse envelope travels in the fiber. α is the complex part of the propagation constant β which denotes losses in the fiber. The nonlinearity parameter γ is defined as

$$\gamma = \frac{n_2 \omega_0}{c A_{\text{eff}}} \tag{6.4}$$

where n_2 is the cladding refractive index and c is the speed of light. The effective core area, A_{eff} is proportional to the integral of fields over all space. For bound modes, γ as defined in Eq. (6.4), gives a physically meaningful value due to the exponentially decaying fields. However, for leaky modes, which has fields that grow in the transverse direction, away from the fiber core, this parameter diverges and hence $\gamma \to 0$, which is nonphysical.

In order to correctly treat the problem of leaky modes, we require the correct normalization, which has been derived in the previous chapters. Using this analytical normalization and the resonant state expansion formalism,

we now derive the master equation for nonlinear pulse propagation, i.e., the nonlinear Schroedinger equation (NLSE) in a more general approach than in Ref. [91] in order to cover leaky mode propagation as well. This also leads to a redefined Kerr nonlinearity parameter, which due to the complex values of the fields and normalization constant, is also complex. This is consistent with results for leaky modes using purely iterative solvers where they show that the complex nonlinearity parameter γ results in additional nonlinear loss (corresponding to positive values of the imaginary part of γ). In Ref. [90], we show for the first time that the imaginary part of γ can also be negative, corresponding to nonlinear gain, depending on the material and fiber parameters. We briefly describe the derivation of the NLSE and γ using the resonant state expansion formalism.

6.2.1 Derivation of NLSE

We start with Maxwell's equations that are Fourier transformed in the direction of translational invariance, i.e., the z direction as defined in Eq. (2.4). The current vector is defined as

$$\hat{\mathbb{J}}(\mathbf{r}_\parallel) = \begin{pmatrix} \mathbf{J} \\ 0 \end{pmatrix} = \begin{pmatrix} -\frac{4\pi i \hat{\mathbf{j}}}{c} - 4\pi k_0 \hat{\mathbf{P}}_{NL} \\ 0 \end{pmatrix}, \tag{6.5}$$

which is the source of the fields. The Green's dyadic can be used to obtain the solutions of Eq. (2.4) for arbitrary sources and satisfies Eq. (2.5). The Green's dyadic of Eq. (2.4), in terms of the resonant states $\hat{\mathbb{F}}_m$ of the system, by using the Mittag-Leffler expansion and the reciprocity principle is given by Eq. (2.21), where we have neglected the contribution of the cut terms which arise from the analytical continuation to the complex β plane. N_m is the analytic mode normalization as derived in Chapter 2 and given by Eq. (2.35). The Green's dyadic is now used to describe the field vectors as

$$\hat{\mathbb{F}}(\mathbf{r}_\parallel, \beta; \omega) = \int \hat{\mathbb{G}}_\beta(\mathbf{r}_\parallel, \mathbf{r}'_\parallel; \omega) \hat{\mathbb{J}}(\mathbf{r}'_\parallel, \beta; \omega) d\mathbf{r}'_\parallel =$$
$$- \sum_m \frac{\hat{\mathbb{F}}_m(\mathbf{r}_\parallel; \omega)}{2 N_m (\beta - \beta_m)} \int \hat{\mathbb{F}}_m^R(\mathbf{r}'_\parallel; \omega) \cdot \hat{\mathbb{J}}(\mathbf{r}'_\parallel, \beta; \omega) d\mathbf{r}'_\parallel. \tag{6.6}$$

The field expressions are then decomposed as

$$\hat{\mathbb{F}}(\mathbf{r}_\parallel, \beta; \omega) = \sum_m a_m(\beta, \omega) \frac{1}{\sqrt{N_m}} \hat{\mathbb{F}}_m(\mathbf{r}_\parallel; \omega), \tag{6.7}$$

where a_m is the modal amplitude. Substituting this expression in the above equation and equating for each m we have

$$\left(\frac{\partial}{\partial z} - i\beta_m\right)a_m(z;\omega) = \frac{1}{2i\sqrt{N_m}}\int \mathbb{F}_m^R(\mathbf{r}_\parallel;\omega) \cdot \mathbb{J}(\mathbf{r}_\parallel,z;\omega)d\mathbf{r}_\parallel. \qquad (6.8)$$

Note that the we have taken an inverse Fourier transform and hence the hats have been removed. The nonlinearity can now be substituted as the source term as in Eq. (6.5) to get

$$\frac{\partial a_m(z;t)}{\partial z} = i\beta_m(t) * a_m(z;t) - \frac{2\pi}{c}\frac{\partial}{\partial t}\int \frac{\mathbf{E}_m^R(\mathbf{r}_\parallel;t)}{\sqrt{N_m}} * \mathbf{P}_{NL}(\mathbf{r};t)d\mathbf{r}_\parallel. \qquad (6.9)$$

Here, $*$ is a convolution in the time domain. Since it is not straight forward to define the Green's dyadic outside of the region of spatial inhomogeneities, hence the above master equation is only valid for nonlinearities within the fiber. However, no other approximations have been made to derive this equation. The most dominant contribution of the nonlinearity comes from the $\chi^{(3)}$ tensor in most fiber examples. By Fourier transforming Eq. (6.7) from the frequency to the time domain and writing the nonlinear polarization as

$$\mathbf{P}_{NL} \approx \frac{\chi_i^{(3)}}{4}\left[2(\mathcal{E}\cdot\mathcal{E}^*)\mathcal{E} + (\mathcal{E}\cdot\mathcal{E})\mathcal{E}^*\right]e^{-i\omega_0 t}, \qquad (6.10)$$

where $\mathcal{E}$ is the envelope field with a frequency around ω_0 we get the propagation equation as,

$$\frac{\partial a_m}{\partial z} \approx i\beta_m * a_m + \sum_{n,p,q}i\frac{2\pi}{c}\frac{\partial}{\partial t}(\alpha_{m,n,p,q}a_n a_p^* a_q), \qquad (6.11)$$

with

$$\alpha_{m,n,p,q} = \int \frac{\chi_i^{(3)}}{4}\left[2(\mathcal{E}_m^R\cdot\mathcal{E}_q)(\mathcal{E}_n\cdot\mathcal{E}_p^*) + (\mathcal{E}_m^R\cdot\mathcal{E}_p^*)(\mathcal{E}_n\cdot\mathcal{E}_q)\right]d\mathbf{r}_\parallel. \qquad (6.12)$$

The Eq. (6.11) results in the nonlinear Schroedinger equation in the single mode approximation, by separating the propagation constant to real and imaginary parts as in Ref. [90, 91] and expanding the real part in a Taylor series around ω_0. This results in a redefined Kerr nonlinearity parameter as

$$\gamma = 2\pi k_0\alpha_{m,m,m,m}. \qquad (6.13)$$

For bound modes, the above approach using resonant state expansion is equivalent to the vectorial approach [93], where the reciprocal conjugate is equivalent to the complex conjugation in that approach.
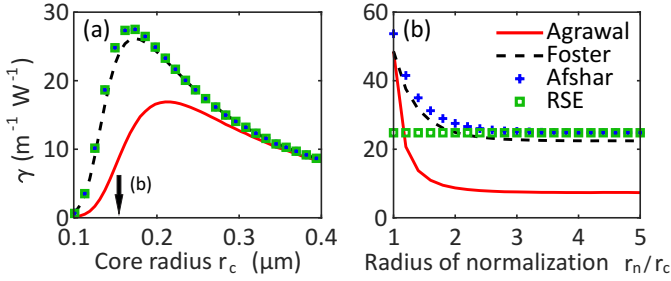
Figure 6.1: Comparison of different approaches [scalar approaches-Agarwal [91] and Foster [92] and the fully vectorial approach by Afshar [93] and the resonant state expansion [90]] for calculating the Kerr nonlinearity parameter γ of the fundamental bound mode of a Bi_2O_3 fiber located in air ($\lambda_0 = 800$ nm): (a) γ as a function of core radius for a radius of normalization $r_n = 5r_c$; (b) dependence of γ on r_n for $r_c = 0.15$ μm, indicated by the arrow in (a) [90].

6.2.2 γ for bound and leaky modes

We can now compare the results for the nonlinearity parameter using our method of the resonant state expansion with other perturbative approaches for bound modes. We select two scalar approaches described by Agarwal in Ref. [91] and Foster in Ref. [92] and the fully vectorial approach by Afshar as in Ref. [93]. We use a test fiber of Bi_2O_3 with $\chi^{(3)}_{Bi_2O_3} = 3.4 \times 10^{-13} \text{cm}^2 \text{statV}^{-2}$ surrounded by air as in Ref. [93]. This is plotted in Fig. 6.1, where we can see in panel (a) that the γ from the resonant state expansion matches perfectly with the fully vectorial approach. The scalar approaches deviate largely for the smaller core radii but seem to converge for the larger cores. In Fig. 6.1 (b), we plot γ as a function of the normalization radius. We can see that for the case of resonant state expansion, due to the normalization being independent of the radius of integration, we immediately achieve the correct value for γ using the smallest computational domain. However, the other methods require a large radius of normalization to converge to the correct value.

We now plot the γ for a fiber supporting leaky modes. We choose as a test fiber a Bi_2O_3 capillary fiber as in Ref. [94, 95] filled with CS_2 [96], which we assume is the only nonlinear material in the fiber with $\chi^{(3)}_{CS_2} = 1.8 \times 10^{-12} \text{cm}^2 \text{statV}^{-2}$. Since the modes are leaky we get a complex value for γ using the resonant state expansion as can be seen in panels (a) and (c) as a function of the core radius. We also see in (b) and (d) that γ remains constant with respect to the radius of normalization for the case of resonant state expansion but tends to zero for other methods. Surprisingly, we notice
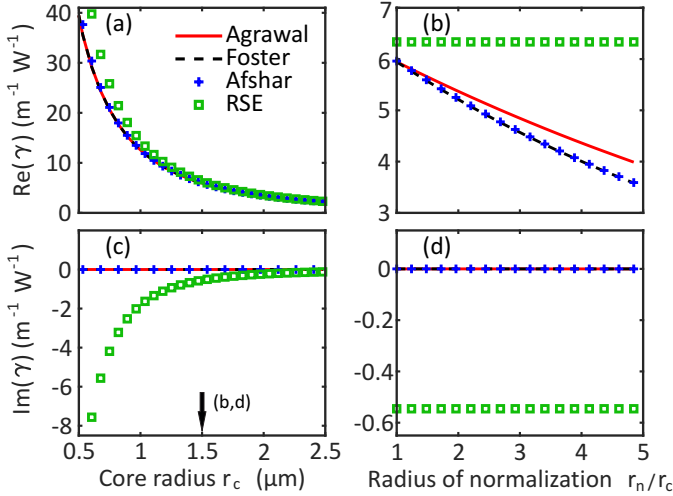
Figure 6.2: Comparison of different approaches (same as in Fig. 6.1) for calculating γ of the fundamental leaky mode of a Bi_2O_3 capillary filled with CS_2 ($\lambda_0 = 800$ nm). Top and bottom panels depict the dependence of the real and imaginary parts of γ as a function of core radius r_c [panels (a) and (c)] with radius of normalization $r_n = r_c$, and radius of normalization [panels (b) and (d)] at a fixed core radius of $r_c = 1.5\mu m$ [arrow in (c)], respectively [90].

that the imaginary part of γ is negative for our test fiber which corresponds to additional nonlinear gain [90].

6.3 Energy in the strands of a light cage structure

Light cage structures are principally a single or double ring of strands placed in a medium [66]. This medium could be air or low index liquids such as water which has important applications in biofluidics. The main guiding principle of the light cage structure in the hollow core is an anti resonant reflecting optical waveguide (ARROW) technique. The dispersion of the real and imaginary parts of the effective index for a optofluidic light cage structure is shown in Fig. 6.3 (a) and (b), respectively, for the fundamental core mode. It is seen in panels (a) and (b) that the core mode has many anticrossings, which arise at the position of resonances of the individual rods that constitute the fiber [17]. The advantage of these light cage structures is that they provide high field

values in regions where high light matter interaction is advantageous [17].

As discussed in Chapter 4, for sensing changes that occur in the homogeneous exterior medium itself like gas sensing, or chemical reaction sensing, mainly two techniques were historically used. The first is the evanescent field sensing [65] which uses the evanescent fields of a bound cladding mode to interact with the exterior. However, since the fields are evanescent the light matter interaction is very low and this results in using very large fiber lengths. Another more efficient method would be to use hollow core fibers, where the medium (gas or liquid) could be filled into the fiber core where there is the possibility of high light matter interaction. However, the accessibility to the fiber core is only from the fiber edges. Hence, reaching an equilibrium of concentration in the exterior medium and the core may take a very long time due to the slow rate of diffusion. In contrast to these fiber structures, the light cage structure provides access to the core transversally and traps light in the core region, solving both problems simultaneously.

The absorbance (A) of a considered optofluidic light cage structure is defined by the modified Beer-Lambert's law [97] as

$$A = -\log_{10}\frac{P}{P_0} = -\log_{10}\eta + \epsilon(1-f)cL + \alpha L. \tag{6.14}$$

where P is the output power, P_0 is the input power, η is the in-coupling efficiency, ϵ is molar attenuation coefficient, while c is the molar concentration of the analyte. f is the fraction of fields within the strands, L denotes the fiber length and α is the modal attenuation.

All quantities of Eq. (6.14) are accessible experimentally through spectroscopic measurements except the fraction of the mode fields within the strands f. This can be theoretically calculated quite easily for bound modes by taking the ratio of integral of S_z within the strands to the integral of S_z over all space. Since the modes are bound with decaying fields as we move away from the fiber core, f has a constant non-zero value. However for leaky modes the integral over all space explodes due to the exponentially growing fields in the transverse direction. Hence, to calculate f the correct analytical normalization is required which has been derived in Chapters 2 and 4. By using this analytically normalized fields the fraction of fields in the strands can be determined by simply integrating over the area of the strands. Such a figure for a test optofluidic light cage structure is plotted in Fig. 6.3 (c). The chosen optofluidic light cage has a background of water with the refractive index of water n_{water} defined as [98]

$$n_{\text{water}} = 1.3199 + \frac{6878}{\lambda^2} - \frac{1.132 \times 10^9}{\lambda^4} + \frac{1.11 \times 10^{14}}{\lambda^6}. \tag{6.15}$$

The refractive index of the strands of the polymer are taken as in Ref. [66]. We can see from Fig. 6.3 (b) and (c) that the fraction of the fields inside the strands nicely follows the trend of losses in the fundamental core mode of the fiber. This is quite easily interpreted by considering that a lower loss would mean more fields in the fiber core due to higher confinement and higher loss means that more energy is away from the core giving rise to higher f values. We also notice sudden peaks at certain wavelengths in f, which arise from the presence of cladding supermodes, which are hybrid modes between the core and the cladding ring.
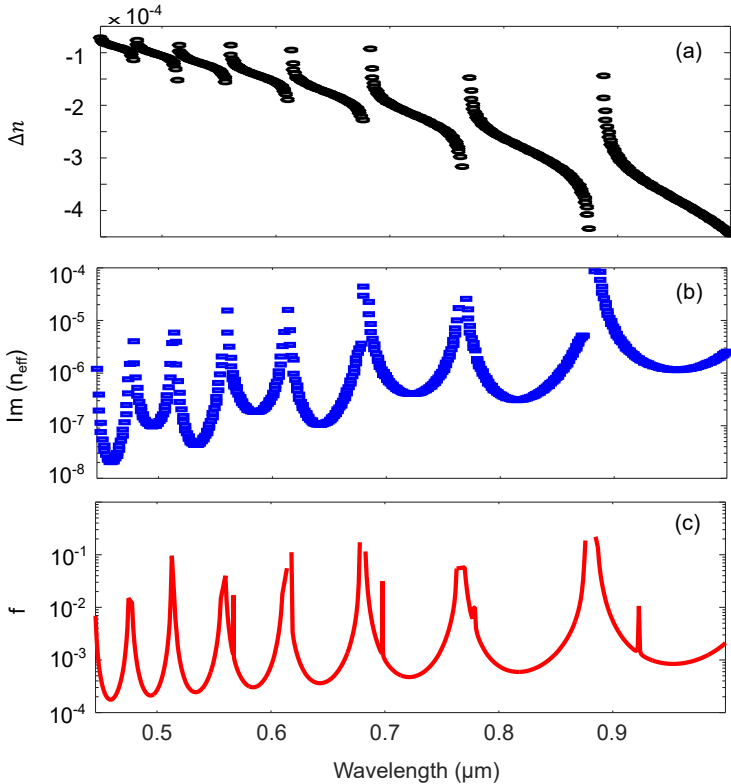

Figure 6.3: The dispersion of the real (a) and imaginary (b) part the effective index for a 12 strand optofluidic light cage structure with background index of n_{water} and polymer strands. Note that the y axis on panel (a) is $\Delta n = \text{Re}(n_{\text{eff}} - n_{\text{water}})$. The energy in the strands f as a function of wavelength is plotted in (c). The diameter of the strands is 3.67 μm and the pitch $\Lambda = 7$ μm.

In conclusion, we have shown two additional applications of the analytical

normalization of bound and leaky modes in fiber structures. There of course can be many more applications, which are beyond the scope of this thesis.

7 Conclusion and outlook

"You know," said Arthur, "it's at times like this, when I'm trapped in a Vogon airlock with a man from Betelgeuse, and about to die of asphyxiation in deep space that I really wish I'd listened to what my mother told me when I was young." "Why, what did she tell you?" "I don't know, I didn't listen."

Hitchhiker's guide to the galaxy, Douglas Adams

In this thesis, we have derived the correct analytical mode normalization for bound and leaky propagating modes in fiber structures. We have applied this normalization to simple step and capillary fibers whose solutions can be obtained analytically and also to complex fiber structures such as light cage and photonic crystal fibers. We have shown that the analytical normalization remains independent of the radius of normalization for both bound and leaky modes even though leaky modes have fields that grow as we move away from the fiber core. We have also shown that the computational domain for evaluating the normalization for bound modes is drastically reduced by using this new normalization. Hence, we have solved a long standing problem of the normalization of leaky modes in the fiber community as a correct normalization is essential for many applications.

We have developed a perturbation theory, i.e., the resonant state expansion by deriving the Green's dyadic using the Mittag-Leffler theorem. The resonant state expansion is limited to interior perturbations as the Green's dyadic must have a finite value everywhere apart from the position of the poles. This does not hold true for leaky modes, which have growing fields in the exterior. This perturbation theory leads to an eigen equation with the eigenvalue as the perturbed propagation constant, which is computationally very easy to solve. We have applied this perturbation theory on two test systems. First, a homogeneous change in the core refractive index of a capillary fiber. We have demonstrated the accurate prediction of the fundamental and higher order modes through this perturbation theory. Second, we have treated diameter disorder for multiple realizations of disorder and various disorder strengths for the fundamental core mode of a silica-air photonic crystal fiber. We have shown that the perturbation theory is an extremely useful tool while studying disorder as a true study of disorder requires averaging over multiple realizations, which the perturbation theory is well equipped to do instead of repeatedly solving Maxwell's equations for disordered systems.

The internal perturbation theory could further be used to study other types of disorder such as material disorder to find the most optimal fiber design. It also gives a direct physical insight into the modes that couple best in the presence of a perturbation in the form of the overlap integral. Furthermore, the current perturbation theory assumes that the perturbation extends to the axial or z direction which is not the case in many fabricated disordered systems. Frozen capillary waves, which are surface waves formed during the fabrication process due to thermodynamic effects may occur as perturbations in the z direction [77]. Perturbation theories can be used to study such processes. It can also be developed to study twist as a perturbation [99], which also occurs in the axial z direction. However, using the appropriate coordinate transformations the twist can be converted as a two dimensional change

in the permittivity and permeability tensors. Also, the effect of the cut contributions in the Green's dyadic have been ignored. This could be included into the theory for increasing the accuracy of the perturbation theory.

We have also extended the perturbation theory to exterior perturbations in fibers. The exterior perturbations can be changes in the permittivity or permeability tensors in the interior along with the exterior and also changes of wavelength, which occurs throughout the fiber. We have shown that even though the perturbation theory deals with exterior changes where fields of leaky modes grow as we move away from the fiber, the perturbation theory is independent of the radius of integration as along as the area of integration encloses all regions of spatial inhomogeneities. We have shown the validity of the first order external perturbation theory on many test systems like step index, capillary, light cage and photonic crystal fiber structures for the fundamental and higher order modes, which has predicted the propagation constant for small perturbations to a high accuracy. Computationally this is very advantageous as dealing with small changes numerically requires high computational abilities. We have also accurately predicted quantities like the group velocity using the external wavelength perturbation theory, as a simple post processing step, while calculating it usually requires solving Maxwell's equations repeatedly for different wavelengths and taking a numerical derivative. Additionally, we have seen that the exact form of the analytical normalization automatically comes out of the external perturbation theory.

This perturbation theory can be extended to higher orders by equating higher orders of the perturbation factor Λ. Similar to the Rayleigh-Schrodinger perturbation theory of quantum mechanics, the complexity of these higher order terms increases. However, it is advantageous to extend the perturbation theory to the second order in order to predict the group velocity dispersion [33], which is another key parameter in fiber design and applications. It might also be interesting to see a full blown resonant state expansion [100] for exterior perturbations, which can capably predict the dispersion of the propagation constant by solving the Maxwell's equations only once.

In this thesis, we have developed a new design rule that lowers the losses of fundamental core modes in high index photonic bandgap fibers by orders of magnitude. This is done by modifying the corner stands in the core surround of the fiber. We have shown, using a test CS_2-silica fiber, that this modification could be an increase or decrease in the corner strand radii and for some particular ratios of radius-to-pitch even completely removing the corner strands. It is seen that this method of loss reduction can also be extended to different materials of the corner strands and to structures such as single ring light cages. The lowering of loss has been analyzed using the fields and Poynting vectors in the transverse directions. Such a field comparison for

different structures of leaky modes is possible because of the normalization. Hence, we have achieved a robust way of reducing losses which applies to all high index photonic bandgap structures irrespective of the radius-to-pitch ratio or the bandgap in use.

Even though a first study of the material change of corner strands has been done, further parametric analysis is needed to completely understand the effect. The losses of the fundamental core mode does decrease by orders of magnitude with changing the corner strand material. However the lowering of loss appears to be independent of corner strand index. Also, more theoretical analysis on the nature of this backscattering is required to further understand the fundamental cause of the lowering of loss to obtain the optimal fiber design. This anti-resonant technique can also be extended to non-bandgap guiding fibers like microstructured silica-air fibers to see the effect of modified corner strands.

We have also demonstrated the use of the analytical normalization in redefining the Kerr nonlinearity parameter for leaky modes by using the resonant state expansion formalism. We have shown that this leads to a complex nonlinearity parameter which may have a positive or negative imaginary part corresponding to nonlinear loss or gain, respectively. It has been shown that it can be further applied to various other nonlinear applications like four wave mixing [101] and so on. We have also used the analytical normalization for calculating the absorbance of a fiber, which requires experimentally inaccessible quantities like the energy in the strands of a light cage.

Hence, we have successfully applied the analytical normalization to study leaky modes in different fiber optic systems for various applications.

Bibliography

[1] A. Ghatak and K. Thyagarajan, *An introduction to fiber optics* (Cambridge University press, 1998).

[2] B. Lee, "Review of the present status of optical fiber sensors," Optical Fiber Technology **9**, 57–79 (2003).

[3] D. A. Krohn, T. MacDougall, and A. Mendez, *Fiber optic sensors: fundamentals and applications* (Spie Press Bellingham, USA, 2014).

[4] J. Heijmans, L. Cheng, and F. Wieringa, "Optical fiber sensors for medical applications-practical engineering considerations," in "4th European Conference of the International Federation for Medical and Biological Engineering," (Springer, 2009).

[5] E. Cibula, D. Donlagic, and C. Stropnik, *Miniature fiber optic pressure sensor for medical applications*, vol. 1 (IEEE, 2002).

[6] A. Perchant, G. Le Goualher, and F. Berier, "Method for processing an image acquired through a guide consisting of a plurality of optical fibers," US Patent 7,903,848 (2011).

[7] G. P. Agrawal, "Nonlinear fiber optics: its history and recent progress," JOSA B **28**, A1–A10 (2011).

[8] R. Stolen and H. Tom, "Self-organized phase-matched harmonic generation in optical fibers," Optics Letters **12**, 585–587 (1987).

[9] K. Inoue, "Four-wave mixing in an optical fiber in the zero-dispersion wavelength region," Journal of Lightwave Technology **10**, 1553–1561 (1992).

[10] P. Russell, "Photonic crystal fibers," Science **299**, 358–362 (2003).

[11] N. Ashcroft and N. Mermin, *Solid State Physics* (Cengage Learning, 2011).

[12] S. G. Johnson, M. Ibanescu, M. Skorobogatiy, O. Weisberg, T. D. Engeness, M. Soljacic, S. A. Jacobs, J. D. Joannopoulos, and Y. Fink, "Breaking the glass ceiling: hollow omniguide fibers," in "Proceedings of 2002 4th International Conference on Transparent Optical Networks," , vol. 2 (IEEE, 2002).

[13] T. M. Ritari, J. Tuominen, J. C. Petersen, and H. Ludvigsen, "Photonic bandgap fibers: optical properties and device applications," in "Optical Transmission Systems and Equipment for WDM Networking III," , vol. 5596 (International Society for Optics and Photonics, 2004).

[14] M. Petrovich, F. Poletti, A. Van Brakel, and D. Richardson, "Robustly single mode hollow core photonic bandgap fiber," Optics Express **16**, 4337–4346 (2008).

[15] T. A. Birks, J. C. Knight, and P. S. J. Russell, "Endlessly single-mode photonic crystal fiber," Optics Letters **22**, 961–963 (1997).

[16] N. M. Litchinitser, S. C. Dunn, P. E. Steinvurzel, B. J. Eggleton, T. P. White, R. C. Mcphedran, and C. M. de Sterke, "Application of an ARROW model for designing tunable photonic devices," Optics Express **12**, 1540–1550 (2004).

[17] C. Jain, A. Braun, J. Gargiulo, B. Jang, G. Li, H. Lehmann, S. A. Maier, and M. A. Schmidt, "Hollow core light cage: Trapping light behind bars," ACS Photonics **6**, 649–658 (2018).

[18] L. Armitage, M. Doost, W. Langbein, and E. A. Muljarov, "Resonant-state expansion applied to planar waveguides," Physical Review A **89**, 053832 (2014).

[19] J. Sakurai and A. W. Longman, *Quantum mechanics* (Addison-Wesley, 1976).

[20] J. O. Hirschfelder, W. B. Brown, and S. T. Epstein, "Recent developments in perturbation theory," in "Advances in Quantum Chemistry," vol. 1 (Elsevier, 1964), pp. 255–374.

[21] E. Muljarov and W. Langbein, "Resonant-state expansion of dispersive open optical systems: Creating gold from sand," Physical Review B **93**, 075417 (2016).

[22] R. Shankar, *Principles of quantum mechanics* (Springer Science & Business Media, 2012).

[23] L. D. Landau and E. M. Lifshitz, *Quantum mechanics: non-relativistic theory*, vol. 3 (Elsevier, 2013).

[24] L. Brillouin, "Les problèmes de perturbations et les champs self-consistents," (1932).

[25] E. A. Muljarov, W. Langbein, and R. Zimmermann, "Brillouin-Wigner perturbation theory in open electromagnetic systems," Europhysics Letters **92**, 50010 (2011).

[26] R. More, "Theory of decaying states," Physical Review A **4**, 1782 (1971).

[27] M. Doost, W. Langbein, and E. A. Muljarov, "Resonant-state expansion applied to three-dimensional open optical systems," Physical Review A **90**, 013834 (2014).

[28] M. B. Doost, W. Langbein, and E. A. Muljarov, "Resonant state expansion applied to two-dimensional open optical systems," Physical Review A **87**, 043827 (2013).

[29] M. Doost, "Resonant-state-expansion born approximation for waveguides with dispersion," Physical Review A **93**, 023835 (2016).

[30] T. Weiss, M. Mesch, M. Schäferling, H. Giessen, W. Langbein, and E. A. Muljarov, "From dark to bright: first-order perturbation theory with analytical mode normalization for plasmonic nanoantenna arrays applied to refractive index sensing," Physical Review Letters **116**, 237401 (2016).

[31] T. Weiss, M. Schäferling, H. Giessen, N. Gippius, S. Tikhodeev, W. Langbein, and E. Muljarov, "Analytical normalization of resonant states in photonic crystal slabs and periodic arrays of nanoantennas at oblique incidence," Physical Review B **96**, 045129 (2017).

[32] E. Muljarov and T. Weiss, "Resonant-state expansion for open optical systems: generalization to magnetic, chiral, and bi-anisotropic materials," Optics Letters **43**, 1978–1981 (2018).

[33] A. W. Snyder and J. Love, *Optical waveguide theory* (Springer Science & Business Media, 2012).

[34] C. Sauvan, J.-P. Hugonin, I. Maksymov, and P. Lalanne, "Theory of the spontaneous optical emission of nanosize photonic and plasmon resonators," Physical Review Letters **110**, 237401 (2013).

[35] R. Sammut and A. W. Snyder, "Leaky modes on a dielectric waveguide: orthogonality and excitation," Applied Optics **15**, 1040–1044 (1976).

[36] C.-T. Tai, *Dyadic Green functions in electromagnetic theory* (Institute of Electrical & Electronics Engineers (IEEE), 1994).

[37] G. B. Arfken and H.-J. Weber, *Mathematical methods for physicists* (Academic Press Harcourt Brace Jovanovich, San Diego, 1967).

[38] M. Doost, W. Langbein, and E. A. Muljarov, "Resonant-state expansion applied to planar open optical systems," Physical Review A **85**, 023835 (2012).

[39] M. Frosz, J. Nold, T. Weiss, A. Stefani, F. Babic, S. Rammler, and P. S. J. Russell, "Five-ring hollow-core photonic crystal fiber with 1.8 db/km loss," Optics Letters **38**, 2215–2217 (2013).

[40] Y. Wang, X. Zhang, X. Ren, L. Zheng, X. Liu, and Y. Huang, "Design and analysis of a dispersion flattened and highly nonlinear photonic crystal fiber with ultralow confinement loss," Applied Optics **49**, 292–297 (2010).

[41] M.-J. Li, J. A. West, and K. W. Koch, "Modeling effects of structural distortions on air-core photonic bandgap fibers," Journal of Lightwave Technology **25**, 2463–2468 (2007).

[42] E. N. Fokoua, S. R. Sandoghchi, Y. Chen, G. T. Jasion, N. V. Wheeler, N. K. Baddela, J. R. Hayes, M. N. Petrovich, D. J. Richardson, and F. Poletti, "Accurate modelling of fabricated hollow-core photonic bandgap fibers," Optics Express **23**, 23117–23132 (2015).

[43] M.-J. Li, J. A. West, and K. W. Koch, "Effects of structural distortions on photonic band-gap fibers," in "OFC/NFOEC 2007-2007 Conference on Optical Fiber Communication and the National Fiber Optic Engineers Conference," (IEEE, 2007).

[44] E. N. Fokoua, D. J. Richardson, and F. Poletti, "Impact of structural distortions on the performance of hollow-core photonic bandgap fibers," Optics Express **22**, 2735–2744 (2014).

[45] T. White, B. Kuhlmey, R. McPhedran, D. Maystre, G. Renversez, C. M. De Sterke, and L. Botten, "Multipole method for microstructured optical fibers. I. formulation," JOSA B **19**, 2322–2330 (2002).

[46] B. T. Kuhlmey, T. P. White, G. Renversez, D. Maystre, L. C. Botten, C. M. De Sterke, and R. C. McPhedran, "Multipole method for microstructured optical fibers. II. implementation and results," JOSA B **19**, 2331–2340 (2002).

[47] J. D. Jackson, *Classical electrodynamics* (John Wiley and Sons, 2007).

[48] J. M. Fini, "Improved symmetry analysis of many-moded microstructure optical fibers," JOSA B **21**, 1431–1436 (2004).

[49] M. Steel, T. White, C. M. De Sterke, R. McPhedran, and L. Botten, "Symmetry and degeneracy in microstructured optical fibers," Optics Letters **26**, 488–490 (2001).

[50] S. Upendar, I. Allayarov, M. Schmidt, and T. Weiss, "Analytical mode normalization and resonant state expansion for bound and leaky modes in optical fibers-an efficient tool to model transverse disorder," Optics Express **26**, 22536–22546 (2018).

[51] S. Both and T. Weiss, "First-order perturbation theory for changes in the surrounding of open optical resonators," Optics Letters **44**, 5917–5920 (2019).

[52] A. M. Pinto and M. Lopez-Amo, "Photonic crystal fibers for sensing applications," Journal of Sensors **2012** (2012).

[53] R. Jha, J. Villatoro, and G. Badenes, "Ultrastable in reflection photonic crystal fiber modal interferometer for accurate refractive index sensing," Applied Physics Letters **93**, 191106 (2008).

[54] B. Keller, M. DeGrandpre, and C. Palmer, "Waveguiding properties of fiber-optic capillaries for chemical sensing applications," Sensors and Actuators B: Chemical **125**, 360–371 (2007).

[55] D. Monzón-Hernández and J. Villatoro, "High-resolution refractive index sensing by means of a multiple-peak surface plasmon resonance optical fiber sensor," Sensors and Actuators B: Chemical **115**, 227–231 (2006).

[56] W. Eickhoff, "Temperature sensing by mode–mode interference in birefringent optical fibers," Optics Letters **6**, 204–206 (1981).

[57] A. Unger and M. Kreiter, "Analyzing the performance of plasmonic resonators for dielectric sensing," The Journal of Physical Chemistry C **113**, 12243–12251 (2009).

[58] W. Zhang and O. J. Martin, "A universal law for plasmon resonance shift in biosensing," ACS Photonics **2**, 144–150 (2015).

[59] J. Yang, H. Giessen, and P. Lalanne, "Simple analytical expression for the peak-frequency shifts of plasmonic resonances for sensing," Nano Letters **15**, 3439–3444 (2015).

[60] M. Mesch, T. Weiss, M. Schäferling, M. Hentschel, R. S. Hegde, and H. Giessen, "Highly sensitive refractive index sensors with plasmonic nanoantennas-utilization of optimal spectral detuning of Fano resonances," ACS Sensors **3**, 960–966 (2018).

[61] S. Arnold, M. Khoshsima, I. Teraoka, S. Holler, and F. Vollmer, "Shift of whispering-gallery modes in microspheres by protein adsorption," Optics Letters **28**, 272–274 (2003).

[62] J. Matsuoka, N. Kitamura, S. Fujinaga, T. Kitaoka, and H. Yamashita, "Temperature dependence of refractive index of SiO2 glass," Journal of non-crystalline solids **135**, 86–89 (1991).

[63] J. H. Lowry, J. S. Mendlowitz, and N. M. Subramanian, "Optical characteristics of Teflon AF® fluoroplastic materials," Optical Engineering **31**, 1982–1986 (1992).

[64] X. Yu, P. Shum, G. Ren, and N. Ngo, "Photonic crystal fibers with high index infiltrations for refractive index sensing," Optics Communications **281**, 4555–4559 (2008).

[65] R. Orghici, U. Willer, M. Gierszewska, S. Waldvogel, and W. Schade, "Fiber optic evanescent field sensor for detection of explosives and CO2 dissolved in water," Applied Physics B **90**, 355–360 (2008).

[66] B. Jang, J. Gargiulo, R. F. Ando, A. Lauri, S. A. Maier, and M. A. Schmidt, "Light guidance in photonic band gap guiding dual-ring light cages implemented by direct laser writing," Optics Letters **44**, 4016–4019 (2019).

[67] I. Thormählen, J. Straub, and U. Grigull, "Refractive index of water and its dependence on wavelength, temperature, and density," Journal of physical and chemical reference data **14**, 933–945 (1985).

[68] F. Kapron, D. B. Keck, and R. D. Maurer, "Radiation losses in glass optical waveguides," Applied Physics Letters **17**, 423–425 (1970).

[69] D. Keck, R. Maurer, and P. Schultz, "On the ultimate lower limit of attenuation in glass optical waveguides," Applied Physics Letters **22**, 307–309 (1973).

[70] Y. Tamura, H. Sakuma, K. Morita, M. Suzuki, Y. Yamamoto, K. Shimada, Y. Honma, K. Sohma, T. Fujii, and T. Hasegawa, "Lowest-ever 0.1419-db/km loss optical fiber," in "Optical Fiber Communication Conference," (Optical Society of America, 2017).

[71] J. C. Knight, "Photonic crystal fibres," Nature **424**, 847–851 (2003).

[72] C. M. Smith, N. Venkataraman, M. T. Gallagher, D. Müller, J. A. West, N. F. Borrelli, D. C. Allan, and K. W. Koch, "Low-loss hollow-core silica/air photonic bandgap fibre," Nature **424**, 657–659 (2003).

[73] P. Roberts, D. Williams, B. Mangan, H. Sabert, F. Couny, W. Wadsworth, T. Birks, J. Knight, and P. S. J. Russell, "Realizing low loss air core photonic crystal fibers by exploiting an antiresonant core surround," Optics Express **13**, 8277–8285 (2005).

[74] G. Bouwmans, L. Bigot, Y. Quiquempois, F. Lopez, L. Provino, and M. Douay, "Fabrication and characterization of an all-solid 2D photonic bandgap fiber with a low-loss region (¡ 20 db/km) around 1550 nm," Optics Express **13**, 8452–8459 (2005).

[75] B. Mangan, L. Farr, A. Langford, P. J. Roberts, D. P. Williams, F. Couny, M. Lawman, M. Mason, S. Coupland, R. Flea *et al.*, "Low loss (1.7 db/km) hollow core photonic bandgap fiber," in "Optical Fiber Communication Conference," (Optical Society of America, 2004).

[76] F. Poletti, N. G. Broderick, D. J. Richardson, and T. M. Monro, "The effect of core asymmetries on the polarization properties of hollow core photonic bandgap fibers," Optics Express **13**, 9115–9124 (2005).

[77] P. Roberts, F. Couny, H. Sabert, B. Mangan, D. Williams, L. Farr, M. Mason, A. Tomlinson, T. Birks, J. Knight *et al.*, "Ultimate low loss of hollow-core photonic crystal fibres," Optics Express **13**, 236–244 (2005).

[78] G. Ren, P. Shum, L. Zhang, X. Yu, W. Tong, and J. Luo, "Low-loss all-solid photonic bandgap fiber," Optics Letters **32**, 1023–1025 (2007).

[79] W. Tong, H. Wei, J. Li, H. Wang, Q. Han, J. Luo, G. Ren, X. Yu, and P. Shum, "Investigation of all-solid photonic bandgap fiber with low losses in low-order bandgaps," Optical and Quantum Electronics **39**, 1071–1080 (2007).

[80] J.-H. Liu and C.-P. Yu, "Loss-reduced internally liquid-filled photonic crystal fibers," in "Photonic and Phononic Crystal Materials and Devices X," , vol. 7609 (International Society for Optics and Photonics, 2010).

[81] Q. Fang, Z. Wang, L. Jin, J. Liu, Y. Yue, Y. Liu, G. Kai, S. Yuan, and X. Dong, "Dispersion design of all-solid photonic bandgap fiber," JOSA B **24**, 2899–2905 (2007).

[82] M. Pourmahayabadi and S. M. Nejad, "Optimal confinement loss reduction in photonic crystal fiber with flattened dispersion," in "2008 International Symposium on High Capacity Optical Networks and Enabling Technologies," (IEEE, 2008).

[83] P. Steinvurzel, C. M. De Sterke, M. Steel, B. Kuhlmey, and B. Eggleton, "Single scatterer Fano resonances in solid core photonic band gap fibers," Optics Express **14**, 8797–8811 (2006).

[84] T. Yang, C. Ding, R. W. Ziolkowski, and Y. J. Guo, "A scalable THz photonic crystal fiber with partially-slotted core that exhibits improved birefringence and reduced loss," Journal of Lightwave Technology **36**, 3408–3417 (2018).

[85] R. Amezcua-Correa, F. Gérôme, S. G. Leon-Saval, N. Broderick, T. A. Birks, and J. C. Knight, "Control of surface modes in low loss hollow-core photonic bandgap fibers," Optics Express **16**, 1142–1149 (2008).

[86] H. K. Kim, J. Shin, S. Fan, M. J. Digonnet, and G. S. Kino, "Designing air-core photonic-bandgap fibers free of surface modes," IEEE Journal of Quantum Electronics **40**, 551–556 (2004).

[87] M. Chemnitz, M. Gebhardt, C. Gaida, F. Stutzki, J. Kobelke, J. Limpert, A. Tünnermann, and M. A. Schmidt, "Hybrid soliton dynamics in liquid-core fibres," Nature Communications **8**, 1–11 (2017).

[88] J. Fleming, "Material and mode dispersion in GeO2· B2O3· SiC2 glasses," Journal of the American Ceramic Society **59**, 503–507 (1976).

[89] A. Argyros, T. Birks, S. Leon-Saval, C. Cordeiro, and P. S. J. Russell, "Guidance properties of low-contrast photonic bandgap fibres," Optics Express **13**, 2503–2511 (2005).

[90] I. Allayarov, S. Upendar, M. Schmidt, and T. Weiss, "Analytic mode normalization for the Kerr nonlinearity parameter: Prediction of nonlinear gain for leaky modes," Physical Review Letters **121**, 213905 (2018).

[91] G. Agrawal, *Nonlinear Fiber Optics*, Optics and Photonics (Elsevier Science, 2013).

[92] M. A. Foster, K. D. Moll, and A. L. Gaeta, "Optimal waveguide dimensions for nonlinear interactions," Optics Express **12**, 2880–2887 (2004).

[93] S. Afshar and T. M. Monro, "A full vectorial model for pulse propagation in emerging waveguides with subwavelength structures part I: Kerr nonlinearity," Optics Express **17**, 2298–2318 (2009).

[94] K. Kikuchi and K. Taira, "Highly nonlinear bismuth oxide-based glass fibres for all-optical signal processing," Electronics Letters **38**, 166–167 (2002).

[95] H. Ebendorff-Heidepriem, P. Petropoulos, S. Asimakis, V. Finazzi, R. C. Moore, K. Frampton, F. Koizumi, D. J. Richardson, and T. Monro, "Bismuth glass holey fibers with high nonlinearity," Optics Express **12**, 5082–5087 (2004).

[96] M. Chemnitz, R. Scheibinger, C. Gaida, M. Gebhardt, F. Stutzki, S. Pumpe, J. Kobelke, A. Tünnermann, J. Limpert, and M. A. Schmidt, "Thermodynamic control of soliton dynamics in liquid-core fibers," Optica **5**, 695–703 (2018).

[97] M. Nissen, B. Doherty, J. Hamperl, J. Kobelke, K. Weber, T. Henkel, and M. A. Schmidt, "UV absorption spectroscopy in water-filled antiresonant hollow core fibers for pharmaceutical detection," Sensors **18**, 478 (2018).

[98] A. N. Bashkatov and E. A. Genina, "Water refractive index in dependence on temperature and wavelength: a simple approximation," in "Saratov Fall Meeting 2002: Optical Technologies in Biophysics and Medicine IV," , vol. 5068 (International Society for Optics and Photonics, 2003).

[99] G. Wong, M. S. Kang, H. Lee, F. Biancalana, C. Conti, T. Weiss, and P. S. J. Russell, "Excitation of orbital angular momentum resonances in helically twisted photonic crystal fiber," Science **337**, 446–449 (2012).

[100] T. Weiss and E. A. Muljarov, "How to calculate the pole expansion of the optical scattering matrix from the resonant states," Physical Review B **98**, 085433 (2018).

[101] I. Allayarov, M. Schmidt, and T. Weiss, "Theory of four-wave mixing for bound and leaky modes," Physical Review A **101**, 043806 (2020).

Curriculum Vitae Swaathi Upendar

PhD - Nov. 2015

4th Physics Institute, University of Stuttgart

Topic: "Perturbation and manipulation of leaky modes in photonic crystal fibers".

Projects: Worked on "Theory of disordered claddings in photonic crystal fibers", funded by the DFG SPP 1839- Tailored disorder under Jun-Prof. Dr. Thomas Weiss, 4th Physics Institute, University of Stuttgart.

Additional Courses: 1. Attended the DFG SPP 1839 Spring school on "Tailored disorder" in May 2017.

Master of Science - 2013 - 2015

National Institute of Technology Karnataka, Surathkal

Subjects: Physics

CGPA: 9.64/10

Projects: 1. Worked on "Graphene based modulator for Terahertz radiation" under Prof. G. Umesh, which includes the calculation of optical and electronic properties of Graphene in the THz region and studying a THz Graphene Intensity Modulator.

2. Submitted a project on a silver based Metal-Insulator-Metal (MIM) waveguide using COMSOL under the guidance of Prof. G. Umesh as part of MSc Course work during III semester (Dec 2014).

Board: National Institute of Technology Karnataka

Achievements: Ranked First in MSc Physics.

Additional Courses: 1. Attended the "IMSc School on Theoretical Physics" organized by the Institute of Mathematical Sciences, Chennai (IMSc) in June-2014.

2. Completed the Stanford OpenEdx Online course on "Quantum Mechanics for Scientists and Engineers" with a grade of 85 percent.

Bachelors of Science - 2010 - 2013

Bhavan's Vivekananda College, Secunderabad

Subjects: Mathematics, Physics and Computer Science (MPCs).

Percentage: 90.72

Project: Submitted a mini-project in C++ titled "Almanak" involving file concepts for a digital diary.

Board: Osmania University

Achievements: 1. Stood 2nd in Bhavan's Vivekananda College and was ranked 13th in Osmania University for BSc MPCs.

2. University topper in Physics-II, Physics-IV, Mathematics-III and Mathematics-IV papers in BSc.

3. Received the PVR Memorial Award and a cash price of Rs. 5000 for getting 100 percent score in Physics-II.

12th standard - 2010

St. Joseph's Convent Sr. Sec. School, Bhopal

Percentage: 89.8

Board: Central Board of Secondary Education (CBSE)

10th standard - 2008

St. Joseph's Convent Sr. Sec. School, Bhopal

Percentage: 89.4

Board: Central Board of Secondary Education (CBSE)

9th July 1992

Birthplace: Secunderabad, India

Acknowledgment